

## AN ABSTRACT OF THESIS OF

Sam Goodrich for the degree of Master of Science in Nuclear Engineering presented on June 21, 2013.

Title: Design, Fabrication, and Characterization of the Laser-Imaged Natural Circulation (LINC) Facility

Abstract approved: \_\_\_\_\_

Wade R. Marcum

Currently there is a great amount of interest in the phenomena of natural circulation as a cooling mechanism for normal operation as well as emergency conditions in nuclear reactors and spent fuel pools. In order to better understand this phenomena for the specific geometry of vertical, heated rods in water, an experimental facility was designed and constructed at Oregon State University. This facility, named the Laser-Imaged Natural Circulation (LINC) facility, consists of a water tank capped with a custom cooling plate through which two heated rods pass into the tank. The LINC facility enables flow patterns in the channel between the heated rods to be imaged and quantified using particle image velocimetry (PIV).

This paper presents the reasoning and theory behind the design of the LINC facility, as well as a characterization of the thermodynamics, boundary layer thickness and velocity profile progression of the system. The thermodynamic analysis consists of bulk equilibrium temperatures and heat removal rates for 3 cases where the two heater rods have equal power levels (dubbed “symmetrical heating”). The boundary layer thickness analysis consists of a test matrix of 5 test cases including symmetrical and asymmetrical heating in which the thickness of the boundary layer is measured using the velocity field between the heater

rods. The velocity profile analysis centered on an effective vertical length of 100 mm along the entrance region between the two rods at one symmetrical rod power. In addition to these experiments, additional synthesis of data regarding the dependence of the Nusselt number on the Rayleigh number along with temperature profile of the boundary layer were collected and presented.

© Copyright by Sam Goodrich

June 21, 2013

All Rights Reserved

Design, Fabrication, and Characterization of the Laser-Imaged Natural Circulation

(LINC) Facility

by

Sam Goodrich

A THESIS

Submitted to

Oregon State University

in partial fulfillment of

the requirements for the

degree of

Master of Science

Presented June 21, 2013

Commencement June 2014

Master of Science thesis of Sam Goodrich presented on June, 21 2013.

APPROVED:

---

Major Professor, representing Nuclear Engineering

---

Head of the Department of Nuclear Engineering and Radiation Health Physics

---

Dean of the Graduate School

I understand that my thesis will become part of the permanent collection of Oregon State University libraries. My signature below authorizes release of my thesis to any reader upon request.

---

Sam Goodrich, Author

## ACKNOWLEDGEMENTS

I would like to thank my friends, family and colleagues. Their friendship and collaboration have made graduate school an enjoyable experience.

I would especially like to thank my wonderful wife Jess. She is the most supportive, kind and understanding person I have ever known. I would like to thank her and my boys, James and David, for being understanding when I needed to work extra hours.

I would like to thank my advisor, Dr. Marcum for all of the help and support he has provided in this work and for always making time to help out. Working with Dr. Marcum has helped me learn to be a better student, professional, and scientist.

Finally, I would like to thank my parents for never considering it a possibility that I might not be able to achieve my ambitions.

## TABLE OF CONTENTS

<u>Section</u>	<u>Page</u>
1 Introduction.....	1
1.1 Objectives.....	2
1.2 Document Overview .....	3
2 Survey of Literature .....	5
2.1 Natural Circulation Phenomena .....	5
2.2 Flow Visualization Using Particle Image Velocimetry.....	10
3 Theory .....	13
3.1 Material Properties .....	13
3.1.1 Properties of water.....	13
3.1.2 Properties of Copper.....	14
3.1.3 Other Materials.....	15
3.1.3.1 Incoloy 800 .....	15
3.1.3.2 Magnesium Oxide (MgO).....	15
3.2 Derived Parameters .....	16
3.2.1 Volumetric Thermal expansion coefficient ( $\beta$ ) .....	16
3.2.2 Kinematic Viscosity .....	16
3.3 Dimensional Analysis .....	17
3.3.1 Biot Number .....	21
3.3.2 Prandtl Number .....	21
3.3.3 Grashof Number .....	22
3.3.4 Rayleigh Number .....	22
3.4 Natural Circulation Loop .....	23
3.4.1 Heat transfer in Cooling Plate .....	25
3.4.2 Heat transfer from heater rods.....	28
3.5 Natural Circulation & Boundary Layer Development .....	32
3.6 Particle Image Velocimetry.....	33

## TABLE OF CONTENTS (Continued)

<u>Section</u>	<u>Page</u>
4 Experimental Facility.....	38
4.1 Design Bases .....	40
4.1.1 Tank design .....	40
4.1.2 Cooling Plate Design.....	42
4.2 Experimental Equipment and Specifications .....	46
4.2.1 Heaters & Cooling.....	46
4.2.2 Instrumentation.....	48
4.2.3 PIV System.....	48
4.3 Procedure and Set-up for Characterization Experiments .....	49
4.3.1 Thermal Equilibrium Analysis .....	49
4.3.2 Boundary Layer Thickness Analysis.....	51
4.3.3 Velocity Profile Analysis .....	54
5 Results and Discussion .....	56
5.1 Energy Balance Characterization .....	56
5.2 Boundary Layer Characterization .....	62
5.3 Velocity Profile Characterization.....	70
5.4 The Nusselt Number and the Transverse Curvature Effect.....	77
5.5 Temperature Profiles .....	79
6 Conclusion .....	83
6.1 Observations.....	83
6.2 Relevance of Work.....	84
6.3 Experimental Limitations .....	85
6.4 Future Work .....	86
7 Works Cited .....	88
8 Nomenclature.....	97
9 Appendix A: Uncertainty Analysis.....	101
10 Appendix B: Experimental Facility Drawings.....	106



## LIST OF FIGURES

<u>Figure</u>	<u>Page</u>
Figure 3.1 Boundary layer sketch showing coordinate conventions .....	17
Figure 3.2 Illustration of LINC facility circulation loops .....	24
Figure 3.3 Illustration of heat transfer mechanisms in primary and secondary loops .....	24
Figure 3.4 Illustration of cross-section of heater rod .....	31
Figure 3.5 Summary of PIV analysis process using images from the LINC facility .....	34
Figure 3.6 Cross correlation map acquired from LINC facility data .....	36
Figure 4.1 Overview of LINC facility .....	39
Figure 4.2 Rendering of LINC facility close up .....	40
Figure 4.3 Tank sketch with dimensions .....	41
Figure 4.4 Detail of cross section of cooling plate with labels .....	43
Figure 4.5 Rendering of side A of cooling plate .....	44
Figure 4.6 Rendering of side B of cooling plate .....	44
Figure 4.7 Cooling configuration of cooling plate .....	45
Figure 4.8 Cross section view of heater rod design. Image courtesy of Bucan .....	47
Figure 5.1 Temperature equilibrium plot for 200W rod power .....	57
Figure 5.2 Power equilibrium plot for 200W rod power .....	57
Figure 5.3 Temperature equilibrium plot for 300W rod power .....	58
Figure 5.4 Power equilibrium plot for 300W rod power .....	58
Figure 5.5 Temperature equilibrium plot for 400W rod power .....	59
Figure 5.6 Power equilibrium plot for 400W rod power .....	59
Figure 5.7 Equilibrium temperature comparison summary .....	60
Figure 5.8 Equilibrium power comparison summary .....	60
Figure 5.9 Surface/contour plot of $V$ with accurate aspect ratio test case 4 .....	63
Figure 5.10 Surface/contour plot of $V$ for full profile test case 4 .....	64
Figure 5.11 Boundary layer comparison Case 1 .....	66
Figure 5.12 Boundary layer comparison Case 2 .....	66
Figure 5.13 Boundary layer comparison Case 3 .....	67

## LIST OF FIGURES (Continued)

<u>Figure</u>	<u>Page</u>
Figure 5.14 Boundary layer comparison Case 4 .....	67
Figure 5.15 Boundary layer comparison Case 5 .....	68
Figure 5.16 Colorized surface plot of V for test case 5 .....	68
Figure 5.17 Surface plot of velocity profile for 200W power .....	71
Figure 5.18 Velocity profile development in absolute units a 200W .....	72
Figure 5.19 Normalized velocity profile development at 200W .....	73
Figure 5.20 Velocity profile from Eckert .....	73
Figure 5.21 Velocity Profile at $Ra=1.5E6$ (13.22mm from leading edge) .....	75
Figure 5.22 Velocity Profile at $Ra=5.4E7$ (43.1mm from leading edge) .....	76
Figure 5.23 Velocity Profile at $Ra=5E8$ (90.75mm from leading edge) .....	76
Figure 5.24 Nu vs. Ra for current work compared with prior work .....	78
Figure 5.25 Temperature profile for 200W symmetrical heating case .....	80
Figure 5.26 Temperature Profile for 300W symmetrical heating case .....	80
Figure 5.27 Temperature profile for 400W symmetrical heating case .....	81
Figure 10.1 Rendering of LINC facility .....	106
Figure 10.2 Rear view rendering of LINC facility .....	107
Figure 10.3 Cooling Plate Side A Top View Detail .....	108
Figure 10.4 Cooling Plate Side A Bottom View Detail.....	108
Figure 10.5 Cooling Plate Side B Top View Detail.....	108
Figure 10.6 Heater Rod Clamp Side 1 Detail .....	108
Figure 10.7 Heater Rod Clamp Side 2 Detail .....	108
Figure 10.8 Parts List.....	108

## LIST OF TABLES

<u>Table</u>	<u>Page</u>
Table 4.1 Boundary Layer Experimental Test Matrix .....	54
Table 9.1 Tabulated Error for Cooling Calculation Components .....	102
Table 9.2 Equilibrium Plate Power Removal Uncertainty.....	102
Table 9.3 Tabulated component error for surface temperature calculation .....	103
Table 9.4 Tabulated component error for Ra calculation .....	103
Table 9.5 Uncertainty in Ra for 4 thermal equilibrium cases .....	104
Table 9.6 Tabulated error for Nu calculation.....	104
Table 9.7 Uncertainty in Nu for 4 thermal equilibrium cases.....	104
Table 9.8 Standard deviation of V used in velocity profile analysis (mm/s).....	105

# **Design, Fabrication, and Characterization of the Laser-Imaged Natural Circulation (LINC) Facility**

## **1 INTRODUCTION**

There is currently significant interest in the energy vertical centered on small, modular reactors (SMRs) [1]. The International Atomic Energy Association (IAEA) classifies any commercial nuclear power reactor with a design power output of 300 MW electric or less as a small modular reactor [2]. This reactor concept enables manufacturing of reactor components such as the pressure vessel at a central location with flexibility to distribute a unit to remote locations. Furthermore, several companies have adopted the concept of ganging multiple units together to accommodate economy of scale. One unique design feature of many SMRs is a passively cooled core which makes several design-basis accidents associated with Generation II, Generation III and Generation III+ reactors obsolete [3], [4]. The passive cooling in the core is achieved by natural convection, also known as natural circulation. Fuel rods locally heat water (used as a coolant and moderator in light water SMRs), which reduces its density and generates buoyancy-driven flow upward to a heat exchanger. This heat is removed and the coolant then becomes more dense, flowing downward in the closed loop to be heated again. In this way SMRs maintain passive cooling in their core as long as the buoyancy forces created by the fuel and heat exchanger exceed resistive forces in the loop. While much is known about the principles governing natural convection, many questions remain [4]. In order to begin to answer some of these questions, the Laser-Imaged Natural Circulation (LINC) facility was designed and constructed at Oregon State University (OSU). The facility consists of a primary and secondary loop where natural convection occurs in the primary loop via heater rods and a cooling plate. In this study, the design-basis calculations are presented to support the decisions behind the design of the facility. In addition, experiments were conducted using the facility to evaluate the accuracy of the design-basis calculations. These experiments

involved a study of (1) the thermodynamic behavior of the system, (2) the determination of the boundary layer thickness at a series of heating conditions, and (3) an analysis of the velocity profile development at a single heating condition. In addition, a preliminary evaluation of the Nusselt (Nu) number of the heater rods as a function of the Rayleigh (Ra) number was performed as well as a temperature profile measurement adjacent to the rods. The results of this characterization study are presented and discussed herein.

## **1.1 Objectives**

The objectives of this work can be divided into two categories: long-term and short-term. The long-term objective is to add to the body of knowledge regarding natural circulation adjacent to vertical, heated cylinders by gathering experimental data about said phenomena within a body of water. The short-term objective, in support of the long-term objective, is to design, construct, and characterize the LINC facility. In order to fulfil the short-term objective, specific tasks were performed:

- An experimental apparatus was designed to create small-scale natural circulation conditions in water adjacent to a heated vertical surface, the velocity of which could be measured and quantified using particle image velocimetry (PIV). This facility is called the LINC facility.
- The LINC facility was fabricated and constructed at OSU and all instrumentation and auxiliary equipment was installed.
- A characterization study was performed using the LINC facility to collect data to compare against design basis calculations. This characterization was done in three primary parts:
  - The facility was used to measure the thermal equilibrium values of bulk temperature, heat removed by the cooling plate and a rough temperature profile. This data was compared to the design basis model.

- The boundary layer thickness was measured for a series of five symmetrical and asymmetrical heating conditions between the heater rods and compared to estimates provided in literature.
- The velocity profile development was measured for a symmetrical heating case of 200W from the leading edge to 100 mm upstream. This velocity profile progression was compared with previous work.

## 1.2 Document Overview

This thesis consists of the following outlined content.

**Chapter 1: Introduction** – An introduction to the need for basic natural circulation research, including a list of objectives and tasks to address this need.

**Chapter 2: Survey of Literature** – Background information summarizing prior work in the fields of natural circulation and particle image velocimetry.

**Chapter 3: Theory** – A detailed treatment of the theory, equations and correlations used to design the LINC facility and characterize it. Included is a summary of physical properties used, the correlations used to model the energy balance of the system, an introduction to natural circulation and boundary layer development, and a primer on particle image velocimetry.

**Chapter 4: Experimental Facility** – A detailed description of the experimental facility and reasoning behind the design. Also, an explanation of the procedures used for both the experimental and modeling work to address the characterization objectives.

**Chapter 5: Results and Discussion** – A presentation of the results of the experiments outlined in the objectives, a comparison to the design basis calculations, and a discussion of the performance of the facility.

**Chapter 6: Conclusion** – Conclusions drawn from the results of the work performed and a brief discussion of limitations and future work.

At the end of the document the reader will find references, a table of nomenclature and appendices. Appendix A contains an uncertainty analysis of the experimental data and Appendix B contains detailed drawings of the experimental facility.

## 2 SURVEY OF LITERATURE

Significant scientific work has been focused on the area of natural circulation for both closed and open systems. Additionally, recently developed experimental techniques such as PIV have been applied toward the characterization of complex fluid flow fields, like those in natural circulation driven conditions. This chapter addresses a compressed summary of relevant work in the area of natural circulation phenomena in an attempt to discover what has been done before and also what needs to be done to progress the science. In addition, a summary of the development and use of PIV as a fluid flow field imaging technique is presented in order to provide context regarding strengths and limitations when applying the technique to natural circulation.

### 2.1 Natural Circulation Phenomena

Examples of natural circulation abound in nature and as such, have likely been studied for centuries. One early pioneer in furthering understanding of natural circulation was Lorenz [5]. In Lorenz's analytical study, he assumed that the only relevant velocity in the fluid flow boundary was that parallel to a heated vertical plate and that temperature in the fluid was a function of distance from the plate only. While the efforts of Lorenz (1881) were a significant beginning to analytical understanding of natural convection, some of the first published experimental results on the topic were those by Lorenz (1934) [6] and Colburn and Hougen [7] where Lorenz measured the heat loss from a 12 cm tall plate that was immersed in oil while Colburn and Hougen measured the heat loss from a vertical cylinder. Elenbaas [8] addressed a need for an analysis of a more complex system than a single vertical plate or cylinder in 1942. He examined natural circulation of air between pairs of isothermal plates ranging in size from 5.95 x 5.95 cm, 12 x 12 cm and 24 x 24 cm. The thickness of the plates were 6mm, 6mm and 10mm, respectively. The ambient temperature was varied from 10°C to 330°C and the angle of the two plates in relation to gravity was varied from 0° to 90°. The heat transfer coefficient was quantified for several cases in order



to begin to characterize and predict natural convection cooling. In 1950, Eckert and Jackson [9] used the integrated momentum equation for forced-convection flow from Kármán [10] to find the flow and heat transfer in the turbulent free-convection boundary layer on a vertical flat plate. Eckert and Jackson obtained a formula for the heat transfer coefficient that agreed with experimental values for Grashof numbers in the range of  $10^{10}$  to  $10^{12}$ . They also obtained a formula for the maximum velocity in the boundary layer and the thickness of said boundary layer. Further work with natural convection in vertical channels was done in 1952 by Ostrach [11]. His work analyzed the heat transfer characteristics, temperature profile, and frictional effects of the flow between two long parallel plates in fully-developed laminar natural convection flow with and without heat sources. In 1953 Ostrach [12] published another paper on the laminar free-convection heat transfer from a flat plate, this time not in a channel. In 1956, Sparrow and Gregg solved the laminar boundary layer equation for the Nusselt number (Nu) specific to vertical circular cylinders [13] and from a heated plate with uniform surface heat flux [14], both under natural convection conditions. In 1958 Millsaps and Pollhausen [15] further investigated the external heat transfer from a heated vertical cylinder in laminar natural circulation conditions and compared their work with Kármán momentum method approximations which were solved using the assumption of a parabolic thermal profile. The exact solutions obtained by Millsaps and Pollhausen were in good agreement with the Kármán parabolic approximations. In 1962, Bodoia and Osterle [16] investigated free convection in a viscous fluid between heated vertical plates by solving the continuity, momentum, and energy equations on a digital computer. They found good agreement with the work by Elenbaas by using a Prandtl (Pr) number of 0.7. The work also examined heat transfer characteristics and the development height for laminar structured flows.

Notable further work on laminar natural circulation was performed by Nagendra (1970) [17], Fujii (1970) [18], Aung (1972) [19], Cebeci (1974) [20] and Narain (1976) [21]. Nagendra et al. found refined heat transfer correlations for vertical cylinders of constant heat flux which matched their own experimental data [22] with a tolerance of

approximately 6%. Fujii and Uehara compared the laminar natural convection along the outer surface of a vertical cylinder with that of a heated vertical plate. They found a simple expression for the Nusselt number of a vertical cylinder as a function of the rod radius and length as well as the Nusselt number of a vertical plate under the same conditions. This allowed for the vast number of correlations that had been developed for a flat plate to be used in applications involving vertical cylinders in the laminar regime. Aung et al. performed an experimental and numerical investigation into the laminar heat transfer in natural convection in vertical plate channels with asymmetric heating. They tested air in two thermal conditions: uniform heat flux and uniform wall temperature. It was found that, in the uniform heat flux case, the maximum temperature on the walls differed by less than 6% for all wall heat flux ratios in the fully developed region. They also found a correlation for the average Nusselt number for the uniform wall temperature case between Rayleigh numbers of 2-400 which proved to be fairly accurate. Cebeci studied the transverse curvature effect on laminar heat transfer from the outer surface of vertical circular cylinders. He did this by applying a two-point finite-difference method for various values of  $Pr$  and the transverse curvature parameter,  $\xi$ . He found that the Nusselt number of the cylinder increases significantly with higher values of  $\xi$  and the effect is especially apparent for materials with low ( $<0.01$ ) Prandtl numbers. He found an expression for the deviation of the local Nusselt number on a cylinder from that of a flat plate as a function of  $\xi$  and  $Pr$ . Narain examined combined forced and free laminar convection along slender, vertical rods. He quantified the effect of transverse curvature on the Nusselt number and found that such curvature has a proportional effect on heat transfer from the cylinder.

Just as understanding of the laminar behavior of natural convection progressed, so did the knowledge of turbulent natural convection. Cheesewright (1968) [23], Kato (1968) [24], Fujii (1970) [25], Sparrow (1974) [26], Mason (1974) [27], Churchill (1975) [28], Cheesewright (1978) [29], and George (1979) [30] all examined turbulent natural convection. Cheesewright aimed to provide reliable velocity and temperature profiles for turbulent natural convection, as the only data previously available was that of Griffiths and

Davis [31]. He presented experimental measurements for temperature and velocity profiles, and local heat transfer coefficients for natural convection on a vertical plane. The turbulent regime results were in good agreement with Eckert and Ostrach as well as with the limited experimental values previously available. In addition to adding valuable data about turbulent natural convection, Cheesewright also contributed important information and experimental data on the transition region in terms of profiles and mean properties. Kato et al. used a new method of finding the heat transfer coefficient from a vertical plate by not assuming a velocity profile from experimental data. Their approach acquired and characterized the wall shear stress, heat flux, and eddy diffusivity distribution from forced convection heat transfer and adapted them to natural convection to obtain velocity and temperature profiles as well as heat transfer coefficients with good agreement with previous experimental results by other authors. In addition, Kato et al. proposed a new criterion for the energy of mean flow and the dissipation of energy near the wall that can be used in both free and forced convection applications.

Fujii et al. undertook an ambitious effort to contribute reliable experimental data for heat transfer behavior in turbulent regime from a heated vertical cylinder submerged in water, spindle oil, and Mobiltherm oil. They presented results over the ranges of  $Pr$  of 2-300, Rayleigh numbers of  $5E7$ - $5E12$ , and modified  $Ra$  of  $1E9$ - $2E16$ . They divided a 1 m tall cylinder into 20 independent axial heated sections allowing for the the assumption of uniform heat flux and virtually isothermal conditions for each separate section since the section segments were so small relative to the flow. They were able to clarify and examine the mechanism and flow patterns associated with the transition region (transition between laminar and turbulent natural convection) and found that the transition region of water was indistinguishable from the turbulent region with respect to heat transfer. They drew many conclusions and provided large amounts invaluable experimental data for natural convection from a heated vertical cylinder with liquids of various Prandtl numbers. One important observation unique to water in their study was that the surface temperature of

the heated cylinder fluctuated in relatively large periods and amplitudes, which was attributed to the indeterminate transition region flow pattern for water.

Sparrow and Minkowycz utilized a local non-similarity solution method to analyze the deviation of heat transfer behavior of cylinders from that of a flat plate under similar conditions. They analyzed a range of parameters in which the local heat flux varied from small deviations to a factor of four difference from an analogous flat plate geometry. They obtained good results which compared well with previously published values, lending credence to the method for other applications. Mason and Seban performed numerical calculations for the free convection heat transfer from vertical plates using a program developed by Ptankar and Spalding [32] with favorable results when compared to available data for air, water, and select oils for isothermal and isoflux conditions. Churchill and Chu developed a simple expression for the average Nusselt number on a vertical plate for all  $Ra$  and  $Pr$  using experimental values as bounds at zero and infinity. They also developed simpler expressions for small ranges of conditions. These expressions were compared to experimental data and it was determined that accurate power law correlations for extended ranges of  $Ra$  and  $Pr$  were generally unsuccessful due to the nature of the shape of the curve. Cheesewright and Doan contributed to the experimental data available for turbulent natural circulation behavior by performing experiments on a 2.75 m tall heated plate using thermocouples and anemometers to gather information for correlation coefficients for temperature and velocity in the turbulent region. They noted that the turbulent region was relatively independent from the main flow as well as the fact that the turbulent region is highly periodic. George and Capp analyzed the turbulent natural convection boundary layer by way of scaling arguments and proposed that the boundary layer has two distinct parts: an outer region where conduction is negligible and an inner region where convection is negligible. They used this information to develop universal velocity and temperature profiles in the two layers.

In addition to those presented here, others have analytically and numerically studied the characteristics of natural circulation on a heated vertical plate or cylinder [33] [34] [35] [36] [37] [38]. Some have studied the boundary layer specifically in such a configuration [39] [40] [41] [42].

In 1986, Myamoto et al. [43] provided much needed experimental data regarding free convection between vertical, heated plates. They measured heat transfer, temperature and velocity profiles between two plates that were 5 m tall and spaced 40, 50, 100, and 200 mm apart. Many built off of the work by Myamoto [44] [45] [46] [47] where Naylor, Fedorov, and Darie studied the case of vertical plate channels numerically and analytically and Habib conducted more experiments providing valuable data on velocity and temperature profiles in water.

Much of the work of the previous authors is compiled in textbooks and handbooks [48] [49], and perhaps one of the most extensive of these is that of Gebhart et al. [50]. In their book, they treat the topics of similarity solutions of various geometries, instability, turbulent and laminar regimes, combined mass and thermal transport, mixed convection and more. It is an excellent summary and resource on the subject of natural convection and is recommended for more information on the topic.

## **2.2 Flow Visualization Using Particle Image Velocimetry**

Using particles to visualize flow has been practiced for centuries. Early observation of fluid flow behavior could be seen with smoke, fog, particles in water, or other mediums. Until relatively recently, the observations have been purely qualitative. Leonardo da Vinci is a notable early scientist who observed flow in a pool and was able to capture sketches of vortices and eddies resulting from an inlet stream to a pool [51]. Ludwig Prandtl conducted experiments in a water channel using mica particles to visualize flow [52]. His observations, though important for understanding developing flow, were strictly qualitative. In the last few decades, advances in imaging and computational capabilities

have transformed fluid flow visualization to the point where quantitative information can be collected from flow fields.

Particle image velocimetry (PIV) is now an accepted name for the flow measurement technique that allows for quantitative measurement of flow fields. Early on, the method was known by other names, including pulsed light velocimetry and particle image displacement velocimetry [51]. The term particle image velocimetry first appeared in academic literature in 1984 [53] [54]. PIV was seen as a promising way to study turbulent flow, which drove development toward that goal [53]. The nature of turbulent flow is characterized by flow in all directions, high velocities and large magnitudes of acceleration. For PIV to be successful, particles need to be small enough and similar enough to the fluid that they follow these complex flows. The small size of the particles is in opposition to the goal of scattering as much light off the particle as possible due to the short exposure time of a camera needed to capture images of high frame rates. This need for high intensity light naturally led to the use of lasers for illuminating particles [55]. In some cases, it was easier to pulse the laser to control exposure time instead of the camera shutter. Standard PIV configurations for two dimensional (2D) flow generally consist of a pulsed laser with a lens to focus the laser light into a light sheet, and a digital high speed camera for capturing images of the particles, however digital imaging is a relatively recent technology and early PIV systems relied on the technology available of the time.

One early and successful method of PIV was to double-pulse a laser to produce a double exposure on high resolution film. In 1983, a method of auto-correlation was proposed which involved dividing the image into a grid of overlapping interrogation areas and each grid coordinate's particle displacement is determined using Fourier transforms [56]. Early PIV was limited by computational capabilities of the time, and as such, some effort was made to find alternate, less computationally expensive means of tracking particles. One such method was pursued by Morck [57] and Vogt [58] wherein they arranged their particle density such that there was a low probability of finding more than one particle per

interrogation area. The method then depended on the assumption that any particle that appeared in a neighboring interrogation area was the same particle. This method solved the problem of limited computational resources but was unable to produce resolutions fine enough for turbulent flow pattern investigation.

With the limitations of analog imaging apparent, efforts were made to explore different imaging techniques such as using digital cameras. Willert [59] and Westerweel [60] showed that digital cameras could be used effectively to capture useful results with PIV. Early digital cameras had very low resolution compared to film but had good pixel regularity. Digital cameras advanced quickly and soon their resolution was on par with film, making them the preferred imaging method for PIV. Another valuable advance to the method came when Lourenco [61] convinced Kodak to make cameras for the PIV market which could hold two images taken in rapid succession [55]. This made the fluid flow direction inherent in the image order, allowed for cross-correlation, and eliminated problems where small displacement in a double-exposed image would simply overlap [53].

Today, PIV systems are available as a package which include a Nd:Yag laser, high speed camera, and software for analyzing camera data. Digital cameras and computational capabilities have advanced such that less than 10 seconds of turbulent flow can be imaged with PIV and generate gigabytes of information about the flow field. Indeed, PIV is often the preferred method for modern flow characterization as it is non-intrusive, has a high resolution and can capture behavior at speeds of 10,000 Hz or more. Much recent work has been done using the method to study natural convection [62] [63] [64] [65].

More information on the development and capabilities of PIV can be found in several books and publications on the subject [55] [66] [51]. The works by Adrian are of particular detail and merit and are a good place to begin to learn more about PIV.

### 3 THEORY

When performing design-basis calculations for the design of the LINC facility, certain material properties were required to facilitate the prediction of heating, cooling, and flow phenomena. These are presented in section 3.1 Heat transfer principles and equations using these material properties are presented in sections 3.2 3.3 and 3.4 . A brief introduction to boundary layer development is included in section 3.5 and a similar introduction on PIV is presented in section 3.6

#### 3.1 Material Properties

##### 3.1.1 Properties of water

Since natural circulation is driven by density differences arising from temperature gradients, accurate and precise knowledge of the temperature dependence of the properties of the fluid becomes very important. The temperature-dependent properties of water that are used in calculations hereafter are gathered from many sources and summarized here.

The viscosity of water (in units of Pa\*s) as a function of temperature is correlated in equation (3.1), where  $T$  is in Kelvin,  $A = -52.843$ ,  $B = 3.7036E3$ ,  $C = 5.866$ ,  $D = -5.789E-29$ , and  $E = 10$ . The correlation has an uncertainty of <3% and a temperature range of 273.16K to 646.15K. [67]

$$\mu(T) = \exp\left(A + \frac{B}{T} + C \ln T + DT^E\right) \quad (3.1)$$

The density of water, in units of kmol/m<sup>3</sup>, is presented in equation (3.2) as a function of temperature where  $A = 17.87$ ,  $B = 35.618$ ,  $C = 19.655$ ,  $D = -9.1306$ ,  $E = -31.367$ ,  $F = -813.56$ , and  $G = -1.7421E7$ . The correlation has an uncertainty of <0.2% and temperature ( $T$ ) is in Kelvin. The temperature range of the correlation is 273.16K to 647.096K. [68]  $T_c$  is the critical temperature of water which is 647.096K. [69]



$$\rho(T) = A + B \left(1 - \frac{T}{T_c}\right)^{\frac{1}{3}} + C \left(1 - \frac{T}{T_c}\right)^{\frac{2}{3}} + D \left(1 - \frac{T}{T_c}\right)^{\frac{5}{3}} \dots$$

$$+ E \left(1 - \frac{T}{T_c}\right)^{\frac{16}{3}} + F \left(1 - \frac{T}{T_c}\right)^{\frac{43}{3}} + G \left(1 - \frac{T}{T_c}\right)^{\frac{110}{3}} \quad (3.2)$$

The thermal conductivity of water, in units of W/m · K is presented in equation (3.3) where  $T$  is in Kelvin,  $A = -0.00432$ ,  $B = 5.7255\text{E-}3$ ,  $C = -8.078\text{E-}6$ , and  $D = 1.861\text{E-}9$ . The correlation has an uncertainty of less than 1% and is valid over the temperature range of 273.15K – 633.15K. [67]

$$k(T) = A + BT + CT^2 + DT^3 \quad (3.3)$$

The heat capacity of water, in units of J/kmol · K is presented in equation (3.4) as a function of temperature (in K) where  $A = 2.7637\text{E}5$ ,  $B = -2.0901\text{E}3$ ,  $C = 8.125$ ,  $D = -1.4116\text{E-}2$ , and  $E = 9.3701\text{E-}6$ . The correlation has an uncertainty of less than 1% and is valid over the temperature range of 273.15K to 533.15K. [68]

$$k(T) = A + BT + CT^2 + DT^3 + ET^4 \quad (3.4)$$

### 3.1.2 Properties of Copper

The thermal conductivity of pure copper as a function of temperature can be predicted by equation (3.5), where  $T$  is in Kelvin and  $k$  is in units of W/m · K. Data from Incropera [48] was fitted to a polynomial across a select range of 200K to 800K where  $A = 446.57$ ,  $B = -0.21306$ ,  $C = 2.5005\text{E-}4$ , and  $D = -1.3706\text{E-}7$ . In this range equation (3.5) correlates to the data with an  $R^2$  value of .9997.

$$k(T) = A + BT + CT^2 + DT^3 \quad (3.5)$$

The thermal conductivity of pure copper as a function of temperature can be predicted by equation (3.6) where  $T$  is in Kelvin and  $C_p$  is in units of  $\text{J/kg} \cdot \text{K}$ . The data from Incropera [48] was fitted to a polynomial across a range of 200K to 800K where  $A= 1.538\text{E}2$ ,  $B= 1.8017$ ,  $C= -5.1792\text{E}-3$ ,  $D= 6.7708\text{E}-6$ , and  $E=-3.2083\text{E}-9$ . In this range, equation (3.6) correlates to the data with an  $R^2$  value of 1.0000.

$$C_p(T) = A + BT + CT^2 + DT^3 + ET^4 \quad (3.6)$$

### 3.1.3 Other Materials

#### 3.1.3.1 Incoloy 800

The thermal conductivity of Incoloy 800 is used in the calculation of rod surface temperature based on the temperature reading from a thermocouple in the rod centerline. The temperature dependence of the thermal conductivity of Incoloy 800 is approximately linear and can be found using equation (3.7) where  $T$  is in Kelvin,  $k$  is in units of  $\text{W/m} \cdot \text{K}$   $A= 6.6942$ , and  $B= .0167$ . Equation (3.7) was correlated from data provided by Special Metals Corporation and is valid across the temperature range of 294K to 1140 K and has an  $R^2$  value of 0.9991 in that range. [70]

$$k(T) = A + BT \quad (3.7)$$

#### 3.1.3.2 Magnesium Oxide

Magnesium Oxide (MgO) is the ceramic filler material in the heater rods used in this experiment. In order to calculate the surface temperature of the Incoloy sheath, the conduction properties of the ceramic packing are required. Data from Slack's [71] study on ceramics was correlated over a small range of interest (165.5K to 554.9 K) to yield the temperature dependence of the thermal conductivity of MgO. This is presented in equation (3.8) as a 5<sup>th</sup> order polynomial where  $T$  is in K,  $k$  has units of  $\text{W/m} \cdot \text{K}$ ,  $A= 3.6221\text{E}2$ ,  $B=$

-2.7050,  $C=9.0470\text{E-}3$ ,  $D=-1.4095\text{E-}5$ , and  $E=8.3113\text{E-}9$ . The correlation has an  $R^2$  value of 0.9998 with the data.

$$k(T) = A + BT + CT^2 + DT^3 + ET^4 \quad (3.8)$$

## 3.2 Derived Parameters

### 3.2.1 Volumetric Thermal expansion coefficient ( $\beta$ )

The driving force behind natural circulation is density differences in a fluid. This being the case, it is needed to be able to quantify how dependent the density is on temperature. The volumetric thermal expansion coefficient,  $\beta$ , is shown in equation (3.9) [48].

$$\beta = -\frac{1}{\rho} \left( \frac{\partial \rho}{\partial T} \right)_p \quad (3.9)$$

Using a correlation such as equation (3.2), one can take the derivative of the density with respect to temperature and insert that into equation (3.9) to obtain  $\beta$  as a function of temperature. It should be noted that equation (3.9) is taken to be at constant pressure.

### 3.2.2 Kinematic Viscosity

The viscosity presented in equation (3.1) is called the dynamic viscosity, or a measure of a fluid's resistance to deformation by shear and tensile stress. Kinematic viscosity is simply the dynamic viscosity divided by the density of the material and is a function of temperature by way of both density and viscosity. The equation for kinematic viscosity is shown in equation (3.10).

$$\nu(T) = \frac{\mu(T)}{\rho(T)} \quad (3.10)$$

### 3.3 Dimensional Analysis

In order to attempt to describe natural convection flow, a brief similarity discussion is appropriate. To begin, it is necessary to define conventions for direction and velocity terms. Figure 3.1 shows a sketch of the boundary layer adjacent to a heated vertical plate. Velocity in the x direction along the plate is denoted by  $v$ , where in the y direction the velocity is denoted by  $u$ . Gravity is taken to be negative in this system.

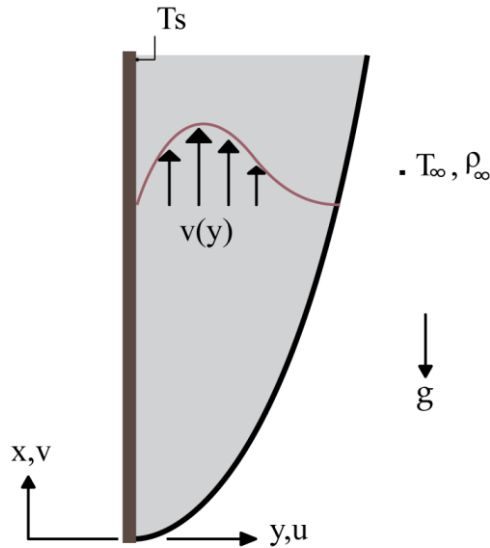


Figure 3.1 Boundary layer sketch showing coordinate conventions

The Navier-Stokes momentum equation for incompressible flow in the x direction is shown in equation (3.11). A note should be made here that even though the system is considered incompressible, the assumption only holds except where the density term is multiplied by gravity, since this is the driving force for natural circulation. This is called the Boussinesq approximation.

$$\rho \left( \frac{\partial v}{\partial t} + v \frac{\partial v}{\partial x} + u \frac{\partial v}{\partial y} + w \frac{\partial v}{\partial z} \right) = - \frac{\partial p}{\partial x} + \mu \left( \frac{\partial^2 v}{\partial x^2} + \frac{\partial^2 v}{\partial y^2} + \frac{\partial^2 v}{\partial z^2} \right) - \rho g \quad (3.11)$$

If the assumptions of steady-state, two dimensional flow are made, then the momentum equation reduces to the expression in equation (3.12).

$$\rho \left( v \frac{\partial v}{\partial x} + u \frac{\partial v}{\partial y} \right) = -\frac{\partial p}{\partial x} + \mu \left( \frac{\partial^2 v}{\partial x^2} + \frac{\partial^2 v}{\partial y^2} \right) - \rho g \quad (3.12)$$

The assumptions are then made that the velocity  $v$  change with respect to  $x$  is much smaller than with respect to  $y$ , and that the partial derivative of density with respect to  $x$  is just the bulk pressure gradient. The latter, when evaluated at  $u=0$ , gives the expression in equation (3.13)

$$\frac{dp_{\infty}}{dx} = -\rho_{\infty} g \quad (3.13)$$

which, when substituting into equation (3.12) and dividing the entire expression by density yields equation (3.14).

$$v \frac{\partial v}{\partial x} + u \frac{\partial v}{\partial y} = g \left( \frac{\Delta \rho}{\rho} \right) + \nu \frac{\partial^2 v}{\partial y^2} \quad (3.14)$$

The volumetric thermal expansion coefficient can be substituted into equation (3.14) by approximating:

$$\beta \approx -\frac{1}{\rho} \frac{\Delta \rho}{\Delta T} = -\frac{1}{\rho} \frac{\rho_{\infty} - \rho}{T_{\infty} - T} \quad (3.15)$$

which yields equation (3.16)

$$v \frac{\partial v}{\partial x} + u \frac{\partial v}{\partial y} = g \beta (T - T_{\infty}) + \nu \frac{\partial^2 v}{\partial y^2} \quad (3.16)$$

Finally, the expression in (3.16) may be non-dimensionalized by the following:

$$x^* = \frac{x}{L}, \quad y^* = \frac{y}{L}, \quad v^* = \frac{v}{v_0}, \quad u^* = \frac{u}{v_0}, \quad T^* = \frac{T - T_\infty}{T_s - T_\infty}$$

where  $L$  is a characteristic length,  $v_0$  is a characteristic velocity, and  $T_s$  and  $T_\infty$  are surface temperature and bulk fluid temperature, respectively. This is applied and shown in equation (3.17)

$$v^* \frac{\partial v^*}{\partial x^*} + u^* \frac{\partial v^*}{\partial y^*} = \frac{T^* g \beta (T - T_\infty) L}{v_0^2} + \frac{1}{Re_L} \frac{\partial^2 v^*}{\partial y^{*2}} \quad (3.17)$$

The velocity term  $v_0^2$  can be chosen arbitrarily so it is chosen to cancel out the coefficient terms to  $T^*$ . This choice is shown in equation (3.18).

$$v_0^2 = g \beta (T_s - T_\infty) L \quad (3.18)$$

The result, when solved for the Reynolds number, is shown in equation (3.19).

$$Re_L = \left[ \frac{g \beta (T_s - T_\infty) L^3}{\nu^2} \right]^{\frac{1}{2}} \quad (3.19)$$

The square of this Reynolds number is called the Grashof number.

In addition to the momentum similarity analysis, one should be done for the energy as well. The thermal energy equation is shown in equation (3.20) where  $T$  is temperature,  $c_p$  is heat capacity,  $k$  is thermal conductivity,  $\dot{q}$  is the volumetric heat generation term and  $\mu \Phi$  is the viscous dissipation term defined in (3.32).

$$\rho c_p \left( v \frac{\partial T}{\partial x} + u \frac{\partial T}{\partial y} \right) = k \left( \frac{\partial^2 T}{\partial x^2} + \frac{\partial^2 T}{\partial y^2} \right) + \mu \Phi + \dot{q} \quad (3.20)$$

$$\mu\Phi = \mu \left\{ \left( \frac{\partial v}{\partial y} + \frac{\partial u}{\partial x} \right)^2 + 2 \left[ \left( \frac{\partial v}{\partial x} \right)^2 + \left( \frac{\partial u}{\partial y} \right)^2 \right] \right\} \quad (3.21)$$

The first simplification that can be made to the energy equation is in reference to the energy transfer and diffusivity in the x direction where it is assumed to be much less than that in the y direction and so all shear stress, flux and diffusion terms in the x direction are taken to be zero. Also, the fluid in this case is not considered to be undergoing any sort of reaction or heat generation effects so  $\dot{q}$  can be removed. Finally, the pressure gradient in the boundary layer is considered to be negligibly different than that of the bulk pressure gradient (shown in equation (3.13)). These simplifications and assumptions lead to equation (3.22).

$$v \frac{\partial T}{\partial x} + u \frac{\partial T}{\partial y} = \alpha \frac{\partial^2 T}{\partial x^2} + \frac{v}{c_p} \left( \frac{\partial u}{\partial y} \right)^2 \quad (3.22)$$

Using the same technique as in the momentum equation, the energy equation is non-dimensionalized and the result is shown in equation (3.23).

$$v^* \frac{\partial T^*}{\partial x^*} + u^* \frac{\partial T^*}{\partial y^*} = \frac{1}{Re_L Pr} \frac{\partial^2 T^*}{\partial y^{*2}} \quad (3.23)$$

Equation (3.17) can be rearranged to obtain temperature as a function of  $x^*$ ,  $y^*$ , Re and Pr (Pr is defined in section 3.3.2). Using the definition of the convection coefficient these expressions can be combined to form a dimensionless temperature gradient shown in equation (3.35). This is known as the Nusselt number and it is a dimensionless way to express the ratio of convective to conductive heat transfer.

$$Nu = \frac{\partial T^*}{\partial y^*} = \frac{hL}{k_f} \quad (3.24)$$

With the brief primer on the origin of the Nusselt number and Grashof number, these quantities are defined and explained hereafter along with other dimensionless parameters

useful for characterizing buoyancy-induced flow. Many of the properties these dimensionless parameters depend upon are temperature-dependent properties of the materials and so while the dimensionless number might not explicitly indicate a dependence on temperature, it is dependent in an indirect manner through the material properties.

### 3.3.1 Biot Number

The Biot number gives a simple ratio of heat transfer resistance through and from a body. A low Biot number indicates conduction is dominant and material temperature should be relatively uniform. A large Biot number would indicate that heat is being transferred via convection faster than conduction can transfer heat to the cooled area. The definition of the Biot number is presented here as equation (3.25), where  $h$  is the heat transfer coefficient,  $L_C$  is the characteristic length (often the ratio of the volume to surface area of the body), and  $k_b$  is the thermal conductivity of the body.

$$Bi = \frac{hL_C}{k_b} \quad (3.25)$$

### 3.3.2 Prandtl Number

One way to normalize and compare the diffusivity of different fluids is by use of the Prandtl number. The Prandtl number is a dimensionless ratio of momentum diffusivity (kinematic viscosity) to thermal diffusivity. As with most other material characteristics mentioned herein, the Prandtl number is also a function of temperature. It is shown symbolically in equation (3.26). The Prandtl number is used in calculating the Grashof and Rayleigh numbers as well as in several heat transfer correlations.

$$Pr(T) = \frac{C_p(T)\mu(T)}{k(T)} \quad (3.26)$$



### 3.3.3 Grashof Number

The Grashof number is a dimensionless number which approximates the ratio of buoyancy to viscous force acting on a fluid. The Grashof number is a function of gravity,  $\beta$ ,  $\nu$ , length ( $L$ ), surface temperature ( $T_s$ ), and bulk fluid temperature ( $T_\infty$ ). The length used in the Grashof number is the characteristic length for the geometry it is applied to; such as diameter for pipes and length for vertical plates. The mathematical definition of the Grashof number is presented here as equation (3.27). Ostrach [12] found a similarity solution for natural circulation adjacent to a vertical, heated plate in which the velocity in the boundary layer is proportional to the fourth root of the Grashof number. The similarity parameter is presented in equation (3.40).

$$Gr_L(T) = \frac{g\beta(T)(T_s - T_\infty)L^3}{\nu(T)^2} \quad (3.27)$$

$$\eta = \frac{y}{x} \left( \frac{Gr_x}{4} \right)^{1/4} \quad (3.28)$$

### 3.3.4 Rayleigh Number

The Rayleigh number is a dimensionless number commonly used in buoyancy-driven flow. An analogy could be drawn from the Reynolds number for forced convection to the Rayleigh number in natural convection. A low Rayleigh number is indicative of conduction as the primary heat transfer mechanism while a high Rayleigh number indicates convection as the primary heat transfer mechanism. The Rayleigh number is simply the Grashof number multiplied by the Prandtl number. The value of the Rayleigh number at which a transition occurs from laminar to turbulent is approximately  $10^9$  [48]. The equation for the Rayleigh number is included here as equation (3.29).

$$Ra(T) = Gr(T)Pr(T) \quad (3.29)$$

### 3.4 Natural Circulation Loop

The LINC facility consists of a primary loop and a secondary loop. The primary loop is an acrylic tank with heater rods inserted into it. At the top of the tank is a custom cooling plate. The heaters and cooling plate drive natural circulation in the primary loop. The secondary loop consists of an industrial chiller and the cooling plate previously mentioned. The chiller pumps cool water through channels machined into the cooling plate to remove heat added to the system by the heater rods. This configuration is illustrated in Figure 3.2. Figure 3.3 illustrates the different heat transfer mechanisms modeled in the design basis calculations. These mechanisms include convection from the heater rods, to the cooling plate and inside the cooling plate channels, as well as conduction through the plate itself. In section 3.4.1 the heat transfer mechanisms and theory for the cooling plate are presented and the same are presented for the heater rods in section 0.

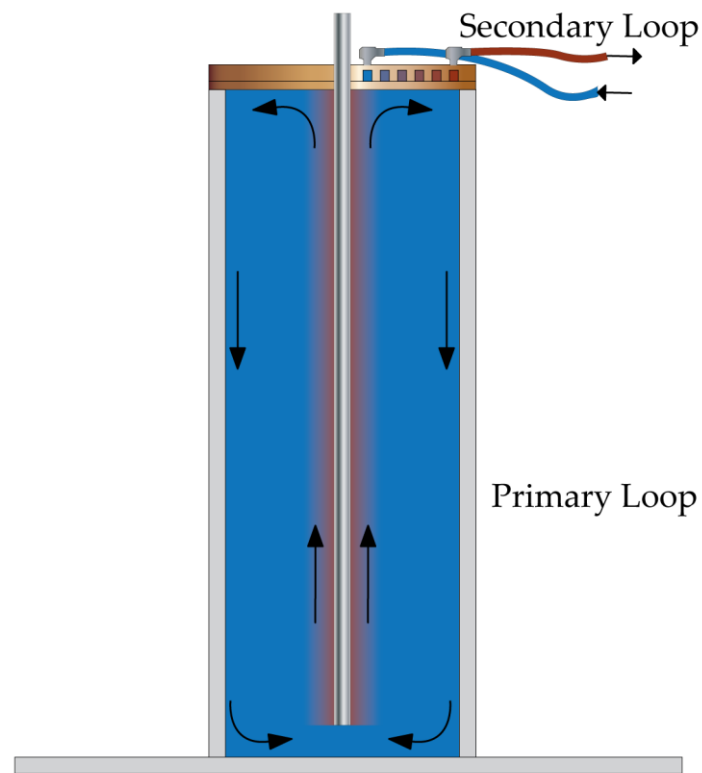


Figure 3.2 Illustration of LINC facility circulation loops

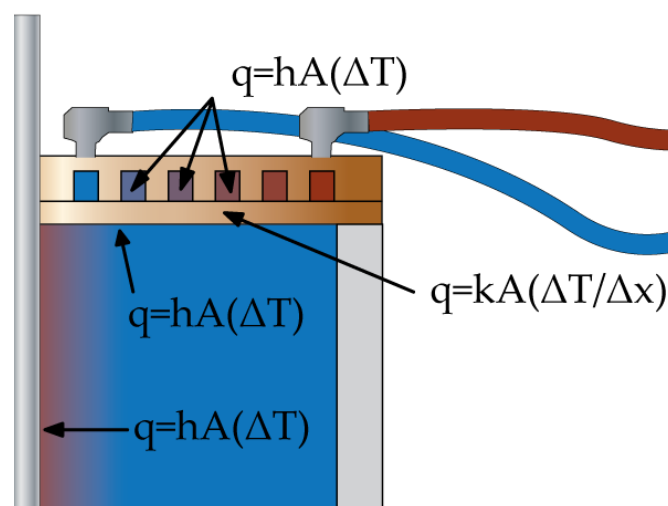


Figure 3.3 Illustration of heat transfer mechanisms in primary and secondary loops

### 3.4.1 Heat Transfer in Cooling Plate

Calculations for the cooling plate include the convective heat transfer inside the cooling channels, the conduction through the plate and the convective heat transfer from the surface in contact with the tank. The plate consists of a top portion (side A) containing cooling channels and a bottom portion to cap off the cooling channels (side B). Further details on the design of the LINC facility are presented in section 4.1.2.

In order to determine the heat transfer from the cooling water to the plate, some analysis of the geometry of the cooling channels must be made. The channels themselves are rectangular in cross sectional shape measuring 6.35 mm deep by 5.08 mm wide. The total length of each of the two channels is 89.54 cm. This means there is a total wetted area in the channel of 204.68 cm<sup>2</sup>. The heat transfer coefficient inside the channels was found by using a correlation by Gnielinski [72] shown in equation (3.30) where  $f$  is the friction factor,  $Re_D$  is the Reynolds number based on diameter, and  $Pr$  is the Prandtl number.

$$Nu_D = \frac{(f/8)(Re_D - 1000)Pr}{1 + 12.7(f/8)^{1/2}(Pr^{2/3} - 1)} \quad (3.30)$$

Once the Nusselt number is found, the convection coefficient can be found using the definition of the Nusselt number, shown here, rearranged as equation (3.31).

$$h = \frac{k_f Nu_L}{L} \quad (3.31)$$

Since the channels are rectangular rather than circular, an effective diameter can be used in the calculation of the Reynolds number. This effective diameter, often called the hydraulic diameter is a function of cross sectional area and perimeter of the channel as

shown in equation (3.32). The hydraulic diameter should be used for all calculations of Reynolds number in the non-circular channels.

$$D_h \equiv \frac{4A_c}{P} \quad (3.32)$$

Once the convection coefficient is found, the next heat transfer problem is that of conduction through the plate. Only one of the four walls in the channels is in direct contact with side B of the cooling plate (see section 4.1.2 for more information on the design of the cooling plate). For conduction through the other 3 walls of the channel located in side A, it has been suggested by some [48] that a correction should be applied to correctly model the resistance of the conduction at the interface between the two plates. This conduction resistance is called contact resistance. It is expressed in units of  $\text{m}^2 \text{K/W}$  and is a function of temperature and power. An expression to quantify contact resistance is presented here as equation (3.33) where  $T_A$  is the temperature at the bottom surface of the plate side A and  $T_B$  is the temperature at the top surface of plate side B. Thermal contact resistance for several metallic interfaces under vacuum conditions was presented by Fried [73] in Tye's book on thermal conductivity. For copper, the resistance had a range of  $10^{-4} \text{m}^2 \text{K/W}$  to  $10^{-3} \text{m}^2 \text{K/W}$  at a contact pressure of  $100 \text{kN/m}^2$ . Equation (3.33) can be rearranged to solve for the temperature difference across the interfacial boundary.

$$R''_{t,c} = \frac{T_A - T_B}{q''_x} \quad (3.33)$$

As is the case with all interfaces of materials, there will be some resistance to heat transfer. However, in the case of the cooling plate in the LINC facility, the materials of the top plate and the bottom plate were chosen to be identical and efforts were made to polish each surface and tighten all fasteners such that the interface resistance is negligible. As such, for the study presented here it is not deemed necessary to account for the interface resistance and equation (3.33) is not used in the model for this facility.

The conduction from the plate to the air or in any direction other than straight down to the bulk fluid of the tank was considered to be negligible. This assumption was made based on an analysis of the Biot numbers at the interface with air and the surface at the interface with the water in the pool. The Biot number for the air surface was  $2.77\text{E-}4$  using equation (3.25) with air considered to be an ideal gas, all properties of air considered to be at 295K and the conductivity of copper taken at 283K. The heat transfer coefficient for the upper surface of a cold plate was found from a correlation for natural circulation by McAdams [74] and presented here as equation (3.34) using equation (3.37) for the characteristic length in the Rayleigh number.

$$\overline{Nu}_L = 0.27Ra_L^{1/4} \quad (10^5 \leq Ra_L \leq 10^{10}) \quad (3.34)$$

The Biot number at the plate-water interface was 0.764, which is three orders of magnitude greater than that of the interface with air. This fully justifies the assumption that the heat conduction in the plate is entirely in the tank direction. As such, for conduction calculations through the copper plate, the cross sectional area of conduction used is that of the wetted area of the bottom side of the plate.

In order to find the heat transfer rate between the pool water and the cooling plate one has to consider more than just conduction as there is a warmer water plumes impinging on the lower surface of the plate which greatly increases heat transfer over simple conduction. In fact, since the cooling plate plane is normal to gravity, the buoyant exchange of warm and cool water helps to break up any sort of boundary layer which could create a temperature gradient and resist heat transfer. McAdams [74] provided correlations for the average Nusselt number as a function of Rayleigh number for a horizontal plate which is either heated with fluid on top or cooled with the fluid on the bottom. These are presented here as equations (3.35) and (3.36). Goldstein et al [75] and Lloyd et al [76] suggest a slight modification to McAdams correlations to enhance accuracy in the form of a modified characteristic length which is shown in equation (3.37) where  $A_s$  is surface area of the plate and  $P$  is perimeter of the plate.

$$\overline{Nu}_L = 0.54Ra_L^{1/4} \quad (10^4 \leq Ra_L \leq 10^7) \quad (3.35)$$

$$\overline{Nu}_L = 0.15Ra_L^{1/3} \quad (10^7 \leq Ra_L \leq 10^{11}) \quad (3.36)$$

$$L \equiv \frac{A_s}{P} \quad (3.37)$$

Once the average Nusselt number is found, the convective heat transfer coefficient can be found in the same method as above using the definition of the Nusselt number.

Once the convective heat transfer coefficients are found from the cooling plate tank surface and cooling channels, the overall heat transfer can be found by an analysis using thermal resistances [48]. The overall heat transfer from the coolant channel to the water in the tank can be represented by equation (3.38) Where  $q_p$  is the power removed by the plate,  $T_{\infty c}$  is the average cooling water temperature,  $T_{\infty t}$  is the bulk fluid temperature in the water tank,  $h_c$  is the convective heat transfer coefficient in the cooling channels,  $\delta_p$  is the thickness of the copper that the heat is conducted through,  $A_p$  is the surface area of the copper through which heat transfer is occurring and which is exposed to the water in the tank, and  $A_w$  is the wetted area inside the cooling channels in plate side A.

$$q_p = \frac{T_{\infty c} - T_{\infty t}}{1/h_c A_p + \delta_p/k_c A_p + 1/h_t A_w} \quad (3.38)$$

One valuable metric for the system is the amount of heat being removed by the cooling plate based on the flow rate of the coolant and the temperature change across the inlet and outlet of the cooling plate. In order to find the power transferred to the coolant in the secondary loop, equation (3.39) can be used, where  $\dot{m}$  is the flow rate of water through the plate,  $C_p$  is the heat capacity of water at that temperature and  $\Delta T$  is the difference in temperature across the plate.

$$q = \dot{m}C_p\Delta T \quad (3.39)$$

It should be noted that heat capacity of water is dependent on the temperature sampled, and for the purposes of this study, the heat capacity was found at the average temperature across the cooling plate. The same assumption applies to the density needed to find the mass flow rate from a volumetric flow rate.

### 3.4.2 Heat Transfer from Heater Rods

The heat transfer from the heater rods to the tank fluid is a function of conduction and convection. The Prandtl number and the Rayleigh number will indicate which mode of transfer is dominant. In the case of water in the LINC facility tank, the average Rayleigh number is on the order of  $10^{10}$  for 200W rod power, so heat transfer will occur primarily via convection in the turbulent regime. Churchill and Chu [77] developed a correlation for the Nusselt number for flat, vertical plates which is valid over all Rayleigh numbers, especially in the turbulent regime. This correlation is presented here as equation (3.40) where  $Ra_L$  is the Rayleigh number based on the length of the plate.

$$\overline{Nu}_L = \left\{ 0.825 + \frac{0.387Ra_L^{1/6}}{\left[1 + (0.492/Pr)^{9/16}\right]^{8/27}} \right\}^2 \quad (3.40)$$

In the case of the LINC facility, cylindrical heater rods are used instead of flat plates, and so an adaptation must be made. Fujii and Uehara [78] suggest a method for laminar natural convection heat transfer from the outer surface of vertical cylinders in the form of an adjustment to the heat transfer correlation for a flat, vertical plate. Although the study specifies the correction is for laminar heat transfer, Churchill [49] presents the correction with no limits on the range of use, and it has been applied here with good results. The correction from Fujii and Uehara is shown as equation (3.41) where  $\overline{Nu}$  is the Nusselt



number for vertical cylinders,  $\overline{Nu}_p$  is the Nusselt number for a flat vertical plate,  $x$  is length along the cylinder and  $D$  is the diameter of the cylinder.

$$\overline{Nu} = \overline{Nu}_p + 0.97 \frac{x}{D} \quad (3.41)$$

Once the average Nusselt number is found for the heater rods, the rod surface temperature can be calculated from the rod power and the convection heat transfer coefficient by substituting the definition of  $h$  from equation (3.31) into equation (3.42) and solving for  $T_s$  where  $q$  is power (W),  $h$  is the heat transfer coefficient,  $A$  is the heated surface area,  $T_s$  is the surface temperature and  $T_\infty$  is the bulk fluid temperature. It should be noted, that for the purpose of the model, the temperature of the rod was assumed to be a constant, average value based on Ra.

$$q = hA(T_s - T_\infty) \quad (3.42)$$

Another method of finding the surface temperature of the rod is from the inside out instead of from the outside in. The heater rods used in the LINC facility have a thermocouple at the centerline of the rod, halfway along the heated portion of the rod. This thermocouple temperature is recorded using National Instruments equipment as described in section 4. In order to find the surface temperature from the centerline temperature, some knowledge of the geometry of the heater is required. The heater rod is diagrammed and described in section 4.2.1 A cross-section of the heater rod is illustrated in Figure 3.4 where the red portion represents the heater element, the light grey represents the ceramic filler, Magnesium Oxide (MgO), and the dark grey represents the sheath or clad.

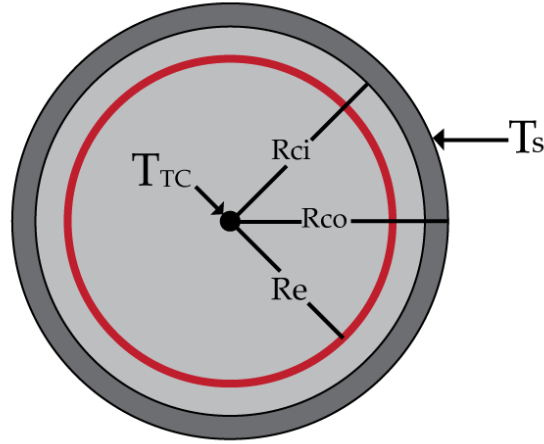


Figure 3.4 Illustration of cross-section of heater rod

The heater element is spiraled 0.1 mm from the inner surface of the clad. The element and thermocouple are packed in MgO. The thermocouple, being in the center of a uniform heating element with no significant form of heat loss in the axial direction, can be considered to be at the same temperature as the heating element. The temperature at the surface of the rod can then be found using equation (3.43) [48] where  $T_s$  is the surface temperature,  $T_{TC}$  is the thermocouple temperature,  $q$  is the rod power,  $L_r$  is the length of the rod over which the power is spread,  $r_{ci}$  is the radius (measured from the center of the rod) of the inside of the cladding,  $r_e$  is the radius of the outer edge of the heating element, and  $r_{co}$  is the radius of the outside of the clad.

$$T_s = T_{TC} - \frac{q}{2\pi L_r} \left[ \frac{\ln\left(\frac{r_{ci}}{r_e}\right)}{k_{MgO}} + \frac{\ln\left(\frac{r_{co}}{r_{ci}}\right)}{k_{inc}} \right] \quad (3.43)$$

This surface temperature is used to calculate the  $Ra$  profile along the heater rod.

### 3.5 Natural Circulation & Boundary Layer Development

With much of natural convection, a good starting point for analysis is with forced convection. The two phenomena are fundamentally similar in many ways. Such is the case for boundary layer development. Early solutions to natural convection boundary layer analyses began with assumptions that the flow was similar in shape and behavior to that of forced convection. Some important early work on the subject was by Eckert and Jackson [9] wherein they developed an expression for the boundary layer thickness and velocity profile for natural convection conditions. These expressions are functions of the Grashof and Prandtl number. In order to find the Grashof number at any vertical coordinate (where  $x$  is chosen to be the distance from the bottom of the rod herein), the functions from section 3.1 were used to create an expression for  $Gr$  that is a function of rod surface temperature, bulk fluid temperature and length. The rod surface temperature can be found using the method outlined in section 0

Eckert and Jackson's equations for the boundary layer thickness and velocity profile are based on first principles and the momentum equation. They are presented here as equations (3.44), (3.45) and (3.46) where  $\delta$  is the boundary layer thickness (in the same units as  $x$ ),  $x$  is the distance over which the flow has progressed,  $Gr$  is the Grashof number evaluated at  $x$ ,  $Pr$  is the Prandtl number evaluated using the bulk fluid temperature, and  $V$  is the velocity parallel to gravity.

$$\delta = 0.565xGr^{-1/10}Pr^{-8/15}(1 + 0.494Pr^{2/3})^{1/10} \quad (3.44)$$

The Grashof and Rayleigh number can be found at any location  $x$  along the heated surface as long as the surface temperature and other material properties are known.

$$V = V_1 \left(\frac{y}{\delta}\right)^{1/7} \left(1 - \frac{y}{\delta}\right)^2 \quad (3.45)$$

$$V_1 = 1.185 \frac{\nu}{x} Gr^{1/2} [1 + 0.494 Pr^{2/3}]^{-1/2} \quad (3.46)$$

As fluid progresses along the heated length of the surface, a few things occur. One is that the temperature of the fluid continues to increase as it spends more time in proximity to the heated surface. This causes the density of the fluid in the boundary layer to drop further as it progresses along the surface, increasing its buoyancy. This added buoyancy lends itself to a higher velocity. Once the velocity increases to a critical amount, it begins to create a region of low enough pressure that it draws in or entrains bulk fluid into the boundary layer. At a certain threshold velocity, the boundary layer will become turbulent as momentum forces overcome viscous forces. The boundary layer increases in size proportionally to the Grashof number as shown in equation (3.44). In the LINC facility, the fluid traveling in the boundary layer around the heated rods will eventually reach the cooling plate, whereupon it cools, then drops down to the bottom of the tank near the outer edge. The velocity of the cool water downward is much lower than that of the warm water upwards due to the disparity of fluid volumes.

### 3.6 Particle Image Velocimetry

PIV systems consist of three essential components: a light source, tracer particles and an imaging system. Often, modern systems consist of Q-switched lasers with high speed cameras capable of up to 10,000 frame per second collection rates, though this figure is likely to be eclipsed with further steady advances. The LINC facility PIV configuration consists of a laser mounted beneath a clear acrylic tank, shining up through the tank between heater rods. There is a high speed camera on a 3-axis mount system directed normal to the laser sheet. In the tank are polystyrene tracer particles which reflect the laser light.

In the LINC facility, image pairs are collected in a known time interval. These images are analyzed by dividing them into interrogation areas and determining a statistical probability

that the particles captured in the first of the image pairs are the same as those in the second image. This “tracking” of particles allows for an average vector to be assigned to that particular interrogation area. The magnitude of the vector assigned to an interrogation area is based on a calibration of distance, and the time interval between image pairs. A representation of the PIV analysis process is shown in Figure 3.5. In the figure, one can see the extent of seeding used in the LINC facility to obtain high resolution vector images.

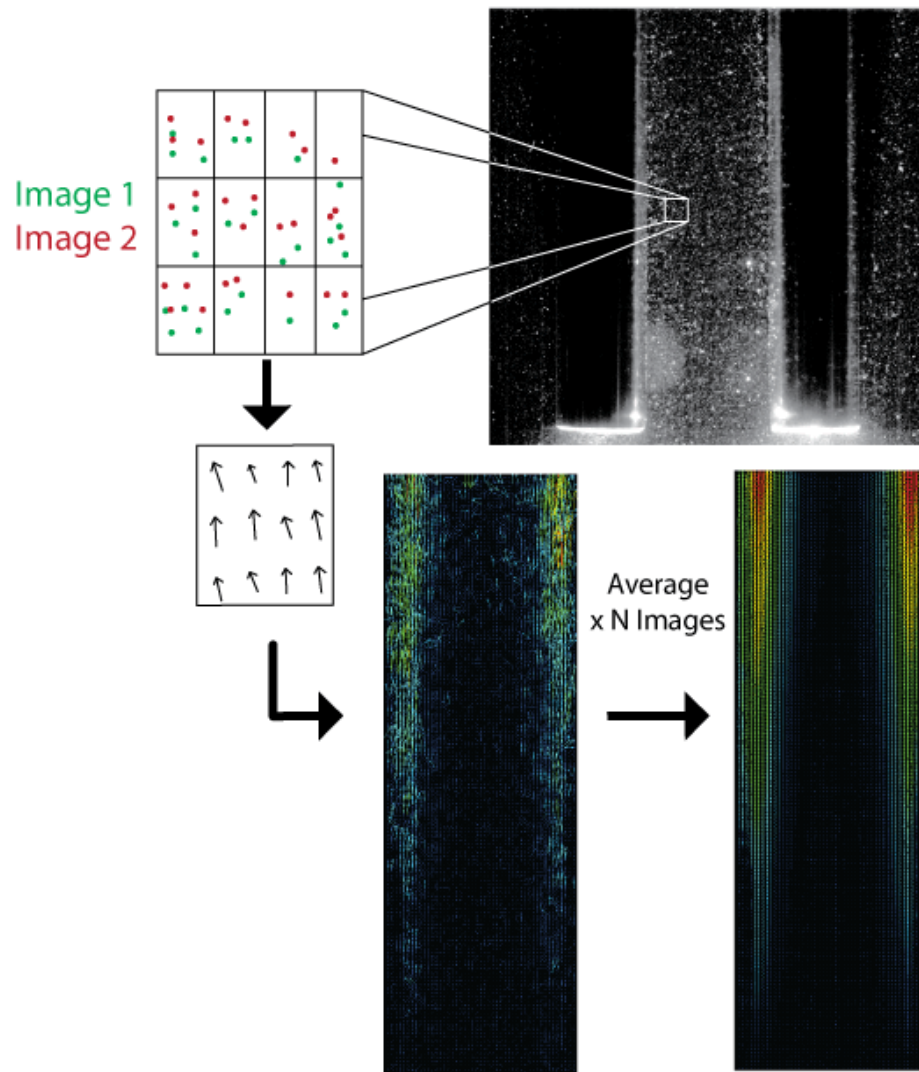


Figure 3.5 Summary of PIV analysis process using images from the LINC facility

In order to obtain a vector for each interrogation area, a cross correlation is performed for the same interrogation area on both images in the pair. This correlation is performed in Fourier space for the computational advantage of performing the calculation. If one estimates the correlation between interrogation area 1 ( $I_1$ ) and interrogation area 2 ( $I_2$ ) on the basis of spatial averages, the cross-correlation estimation for a region is given by equation (3.47) where  $I(X)$  is the intensity distribution of the interrogation area and  $s$  is the shift.

$$R(s') = \int_{W_1} I_1(X)I_2(X + s')dX \quad (3.47)$$

The cross correlation finds the shift in space where the intensity distributions of corresponding interrogation areas line up by finding the maximum of  $R(s')$ . With proper seeding and interrogation area size, the largest correlation coefficient will correspond to actual displacement of the seed particles, which can then be used to calculate the velocity vector in that interrogation area. This process is performed for each interrogation area in each image pair. An example correlation map is shown here as Figure 3.6, where the peak in the center corresponds to the largest correlation coefficient, which is the displacement solution. An acceptance factor for the ratio of the tallest peak to the second tallest can be set for the analysis so that a vector will only be considered valid if the signal of the largest peak is a certain multiple of the next largest peak.

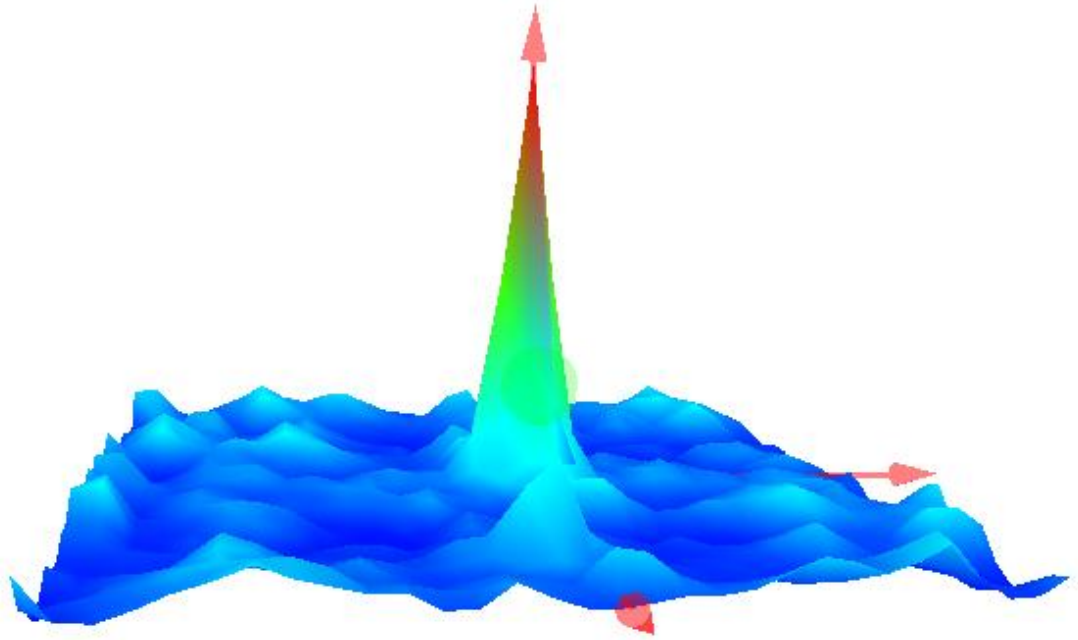


Figure 3.6 Cross correlation map acquired from LINC facility data

One consideration with PIV and interrogation areas is that the cross-correlation of an area only relates to that area and not a neighboring area. This can be aided by specifying a certain overlap of interrogation areas. Another consideration for PIV is the particle density in the interrogation area. It is generally considered optimum to have 5-10 particles in each interrogation area and for the particles to traverse less than 25% of the length of the area [51].

Many refining methods exist for obtaining accurate, high resolution vector fields. Generally, a very reliable method for refining data for steady state flow is simply to take a large number (500-1000) of image pairs and average them using a vector statistic algorithm (provided by Dantec Dynamics in this case). Other methods include moving average validation, outlier removal algorithms, and interpolation methods. For further information on these techniques the reader is referred to the works by Adrian and Raffel [51] [66].

Seeding fluid flow is a very important aspect of PIV technique. The seeds need to be similar in density and momentum to the fluid so as to flow with it. The images taken and analyzed in a PIV system are of these particles, and so in order to capture the fluid dynamics the particles need to behave the same way. In addition to density matching, the particles need to have enough surface area to reflect light to the camera. There is a fine balance for seed particle choice for these reasons as characteristics that make ideal particles are sometimes in opposition to each other. The seed particles used in the LINC facility are 10  $\mu\text{m}$  polystyrene microspheres. Polystyrene has a density of 1.05 g/cc, which is very similar to that of water. There are many analyses on how to implement seeding particles to each experimental application and fluid including accounting for characteristics such as settling time and frequency response. Again, the reader is referred to Adrian's book on the topic for more information [51].



## 4 EXPERIMENTAL FACILITY

The LINC facility is a natural circulation facility with a fast response time and flexibility for various experiments. Currently the facility accommodates two vertical heater rods mounted through a top cooler plate. These rods heat water in the tank, which rises and impinges upon the bottom surface of the cooling plate, cools, then drops to the bottom of the tank only to be heated again. There is a laser mounted beneath the tank pointed upward to create a plane of light between the heater rods. A high speed camera is mounted pointing perpendicular to the rods and normal to the laser light plane to capture images of seed particles illuminated by the laser. Figure 4.1 shows a labeled rendering of the LINC facility. Figure 4.2 shows a closer view of the system and includes a rendering of the laser light configuration.

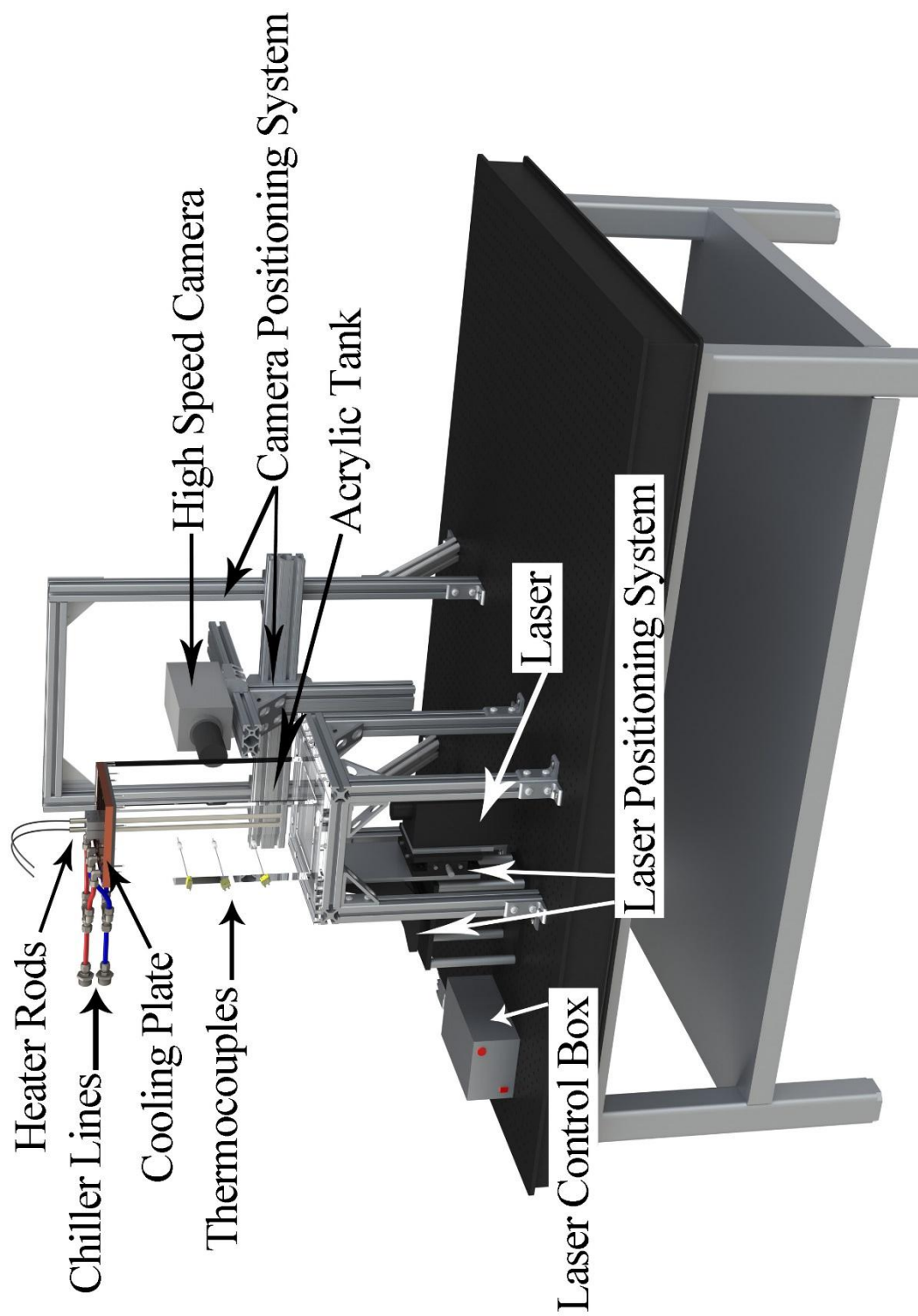


Figure 4.1 Overview of LINC facility

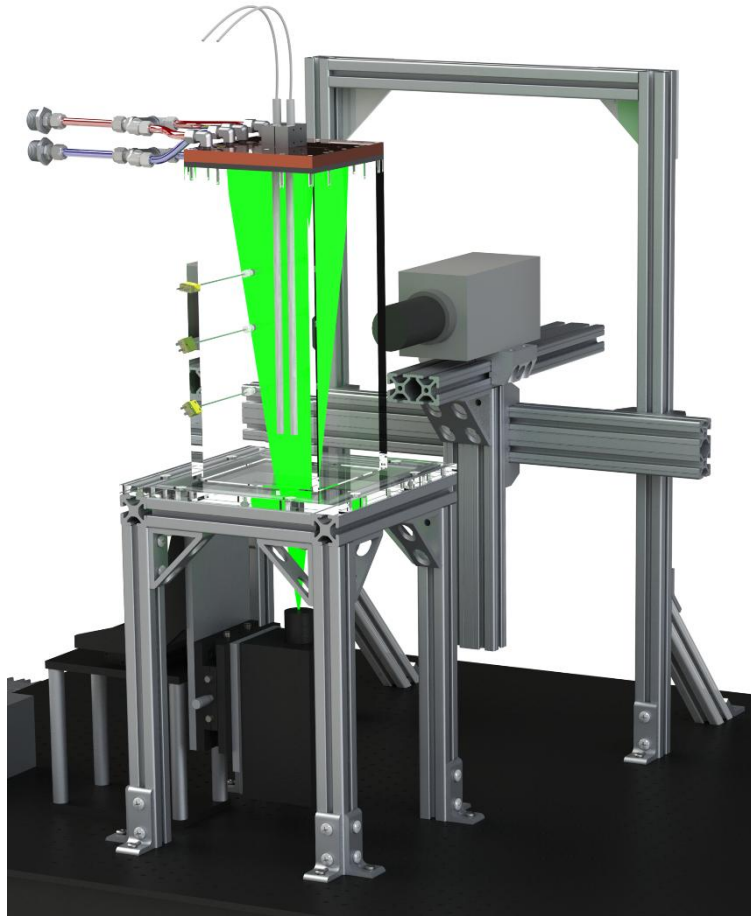


Figure 4.2 Rendering of LINC facility close up

## 4.1 Design Bases

### 4.1.1 Tank design

The design of the facility originated with the heater rod diameter, which was chosen to be 3.18 mm (3/8 in) diameter because this is a common size for fuel pins and also a common size for cartridge heaters. From there, a suitable diameter for the tank was chosen based on the number of rod diameters to ensure the effects of the wall on the flow would be negligible. For this reason, a rectangular tank was designed with an inner diameter of 152

mm (6 in) on a side. The height of the tank was chosen to be 381 mm (15 in) inside from the “floor” of the tank to the cooling plate surface. The pitch of the rods is adjustable, and so the number of diameters between the heater rod and the wall in this design ranges from 6.5 to 1 in one direction and remains constant at 7.8 diameters in the other direction. A sketch of the tank is shown in 1 Figure 4.3.

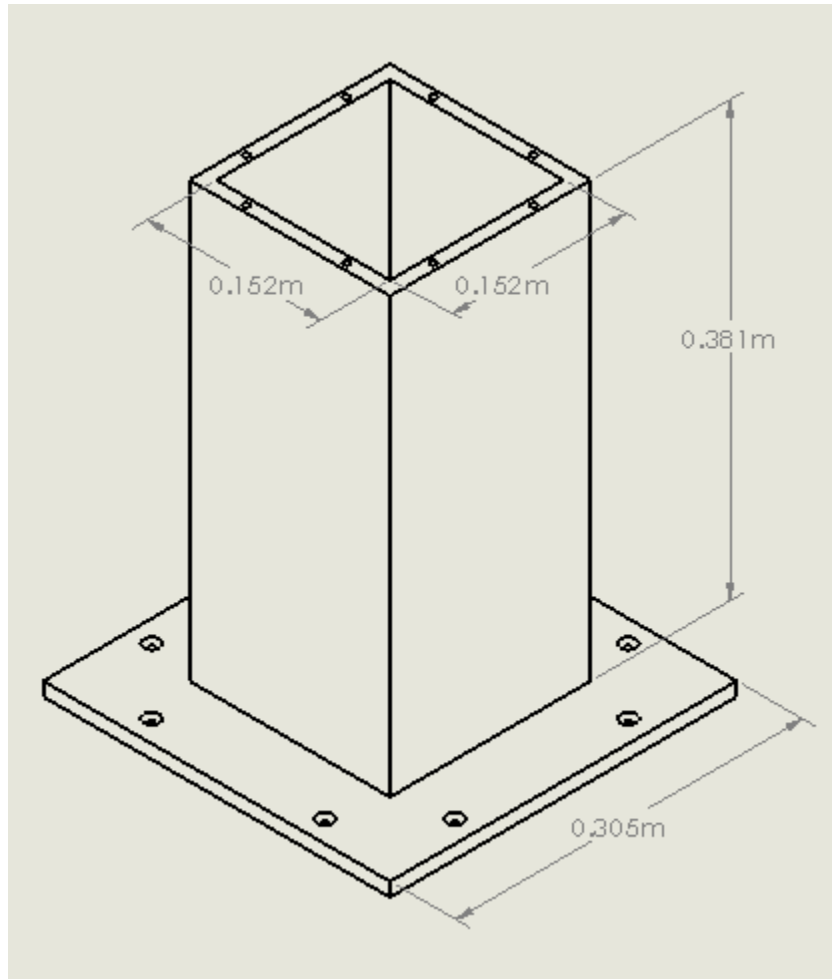


Figure 4.3 Tank sketch with dimensions

The tank was constructed of transparent acrylic which is 11.13 mm thick. This thickness was chosen for strength and robustness and also for the convenience and benefit of having the transparent tank bottom also be the mounting surface to a stand. This thickness allows for the full weight of the water tank to rest on the oversized transparent bottom. This is important because the laser is positioned underneath the tank pointing up to create a light plane between the heater rods for the PIV system. Acrylic was chosen as the tank material both for its strength and for its similar index of refraction to water.

#### *4.1.2 Cooling Plate Design*

The design of the cooling plate has accounted for more design time than any other component of the LINC facility. It was desired to have the flexibility to be able to test various rod pitches, but two issues complicated the design. The first was the desire to avoid complex flow effects from a long channel in contact with the water and the second issue was the cost with machining a custom cooling plate for every pitch desired. The design of the cooling plate solves both of these issues by making the cooling plate in 2 pieces. The top portion (side A) has all of the coolant channels, rod mount hardware, O-ring glands, and tank mount holes while the bottom plate (side B) is simply a thin cap to contain the coolant. A cross-section of the cooling plate assembly is shown in Figure 4.4 to clarify the design of the plate. The portion of the bottom plate in contact with the water in the tank is polished and flat all except for two holes for the heater rods which have a fit tolerance small enough to be virtually flat across the entire plate. While the flat bottom plate only has 2 holes in it, the top portion of the cooling plate has a channel cut into it in the center with 8 mounting positions for each rod, in 6.35mm inch increments. This allows for fine adjustment to various rod pitches, and just replacing the bottom plate for each pitch. In order to ensure good conduction to and from the plate, it was made from Copper 110, which is 99.9% pure. The technical drawings of the cooling plate are included in Appendix A (as Figure 10.3, Figure 10.4, and Figure 10.5) and should be referred to for clarification of the explanations herein. These drawings show the channel for the heater rods, the adjustment

locations for the variable pitch, the dimensions of the cooling channels and the O-ring glands for sealing between the two plates. A 3D rendering of the bottom of side A is shown here as Figure 4.5 and the bottom of side B is shown in Figure 4.6.

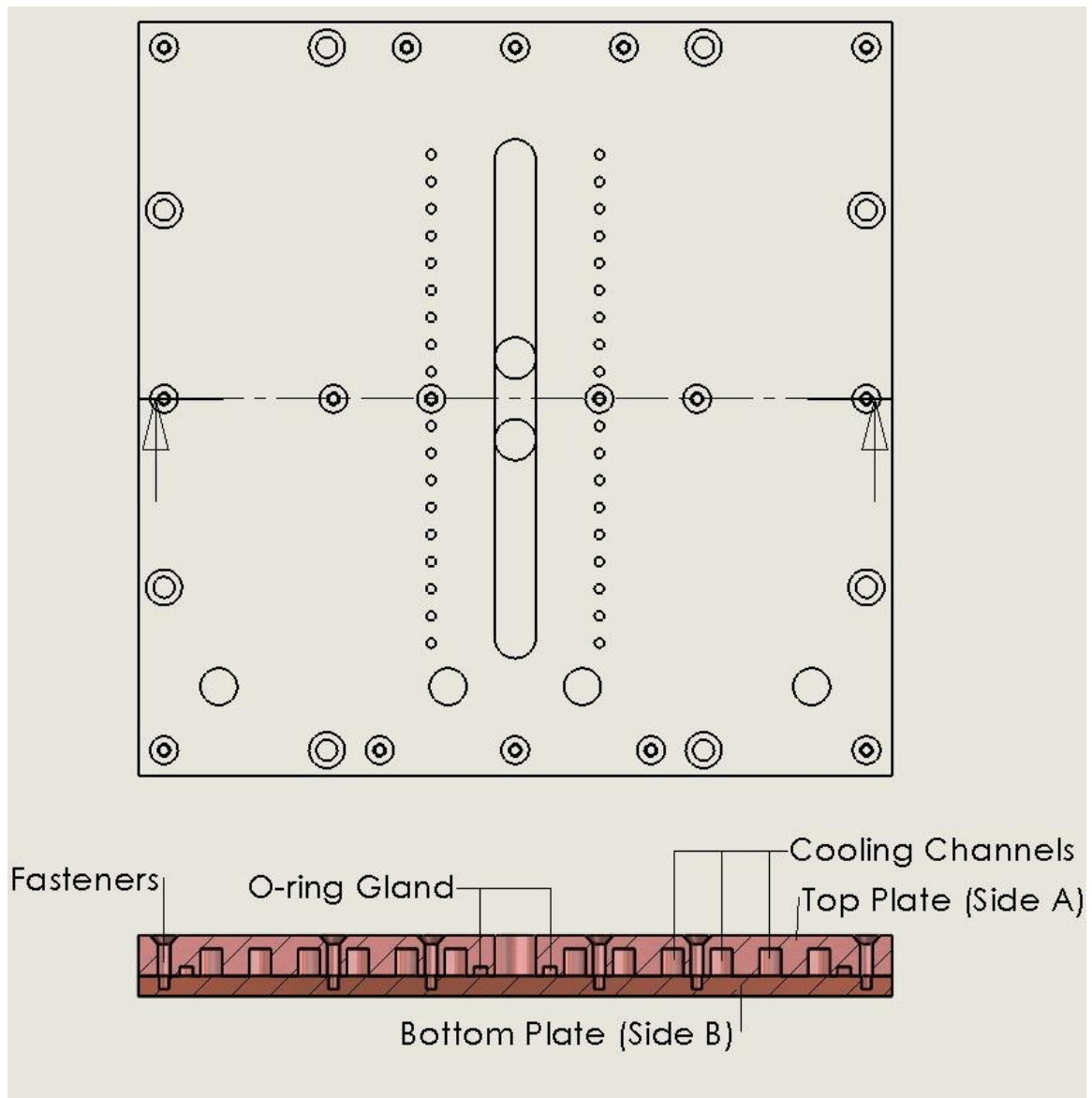


Figure 4.4 Detail of cross section of cooling plate with labels

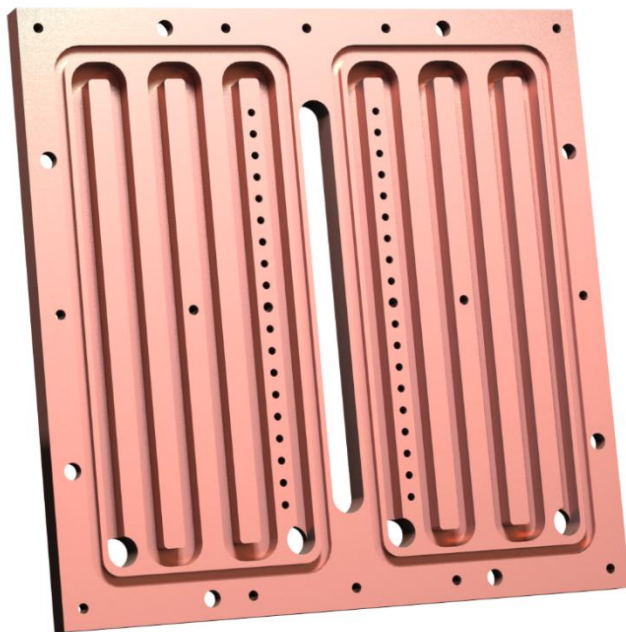


Figure 4.5 Rendering of side A of cooling plate

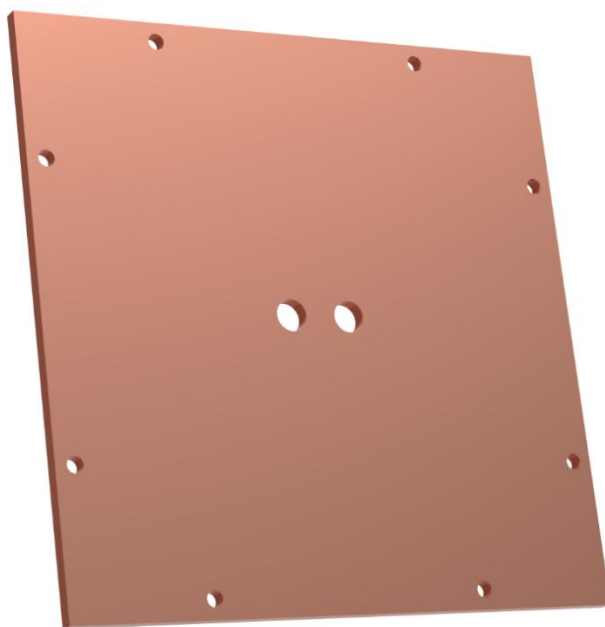


Figure 4.6 Rendering of side B of cooling plate

The top of side A has pipe threaded holes for fittings to be attached to the cooling water lines from the chiller. As can be seen from Figure 4.5, the plate is split symmetrically along the centerline of the rod channel. This means that there are two separate cooling channels which are cooled symmetrically by splitting the flow from the chiller into 2 lines as shown in Figure 4.7. Also shown in Figure 4.7 is how the colder (blue) lines start at the center and the warmer water (red) leaves the plate toward the outside edge.

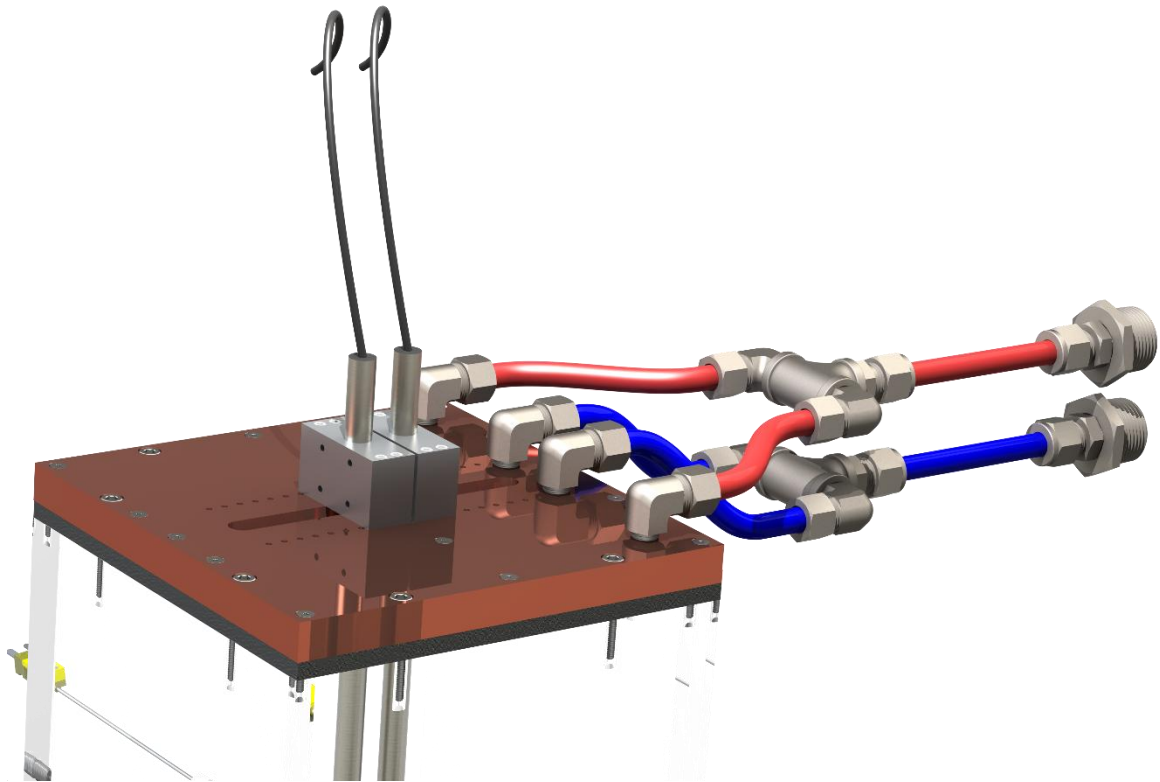


Figure 4.7 Cooling configuration of cooling plate

The cooler plate is attached to the acrylic tank using steel socket head cap screws which sit flush with the top of the plate and screw into brass press-fit expansion inserts in the acrylic tank. These brass inserts were pressed into holes drilled into the acrylic tank.



In between the cooling plate and the acrylic is a silicone foam gasket to seal the water in. This silicone foam allows for all of the air in the tank to be eliminated so the water can have total contact with the cooling plate. The two plates are attached together using small screws which pass through side A and attach to threads cut into side B at several locations (specified in Figure 10.5).

## **4.2 Experimental Equipment and Specifications**

### *4.2.1 Heaters & Cooling*

When choosing heater rods, preference was given to the diameter of fuel pin commonly used in the nuclear industry (9.525 mm). It was desired to have rods long enough to be able to analyze a long section of developed natural convective flow and so a heated length of 0.3048 m (12 in) was chosen. The heater rods used were manufactured by Bucan Electric Heating Devices Inc. An example cross section of the heater rod is provided in Figure 4.8. The diameter of the rods are 9.525 mm. They are 0.4064 m in total length with 0.3048m of it uniformly heated, starting 6.35 mm (0.25 in) from the tip opposite the leads. A Type K thermocouple was installed in the heater halfway along the heated region (0.15875 m from the end opposite the leads) in the center of the Magnesium Oxide (MgO) core ceramic (region 2 in Figure 4.8). The heater rod is sheathed in a thickness of 1 mm of INCOLOY-800 (number 4 in Figure 4.8). The heater element is a spiral NiCr wire (number 1 in Figure 4.8) that is packed into the sheath approximately 0.13 mm from the wall (with MgO between) (region 3 in Figure 4.8). The heater rods have an input voltage range of 0-100V and an operational power range of 0-700W.

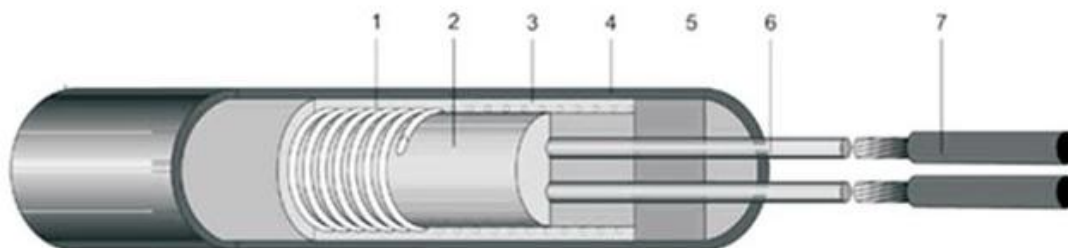


Figure 4.8 Cross section view of heater rod design. Image courtesy of Bucan

The power supplies used to power each rod are BK Precision® brand, model number XLN10014. These have a voltage range of 0-100V and a current range of 0-14.4 A. They have a readback accuracy of 0.05%+25mV which allows for accurate feedback of actual power being used by the rods. These power supplies were chosen for their versatility and precision. Also, since the power supplies monitor actual power usage there was no need to acquire additional equipment to measure current and voltage. The power supplies are programmable and can be controlled by a USB interface but for the purposes of the lab they are manually adjusted using the built-in keypad and LCD.

The heater rods are held in place by custom clamps which are made from aluminum. These clamps mount to the top of the cooler plate in any of several locations depending on the desired pitch. Detailed information on the heater rod clamps can be found in Appendix A in Figure 10.6 and Figure 10.7.

The chiller used is a Cornelius® brand, model number CH951A. It has a 1 horsepower condensing unit, a reserve capacity of 18.9 gallons and an operating water temperature range of 40-100°F. The secondary loop (cooling) flow rate is measured with an acrylic rotameter with a steel float. The rotameter has a 25.4 cm viewing scale and a flow range of 0.76 - 8.33 L/min. The read-out precision of the rotameter is 0.038 L/min with an accuracy of  $\pm 2.0\%$ . With the system configuration in the LINC facility, the circulation rate in the cooling water line is 3.03 L/min. This flow rate is largely governed by the pressure drop across the cooling plate, tubing and fittings.

#### 4.2.2 Instrumentation

In order to perform an energy balance on the facility, the temperature at various locations were measured. These locations are as follows:

- In the tank:
  - One thermocouple mounted in the center of the tank at the height of the center of the heated region of the rods.
  - One thermocouple above and one below the center thermocouple at a distance of 7.62 cm (3 in) from center.
- In the cooling water line:
  - One mounted into a “cross” fitting at both the inlet and outlet lines to the cooling plate.

Temperature data was collected using a National Instruments™ CompactRIO model number CRIO-9022 controller with a cRIO-9113 4-slot chassis. The chassis contains a 16-channel thermocouple input module, model number NI 9213 which read in all thermocouple data. The thermocouple data was processed and displayed using LabView. A LabView program was written which collected temperature data from the 7 thermocouples (3 in the tank, 2 on secondary loop and 2 in heater rods), and created a spreadsheet from the data, recording temperatures at a rate of 1 Hz. The spreadsheet filename is automatically named based on the date and time of the experiment.

#### 4.2.3 PIV System

The PIV system is a package from Dantec Dynamics which includes a laser, high speed camera, timer box and DynamicStudio software. The laser is manufactured by RayPower, model number 5000. The laser is Q-switched, has a wavelength of 532 nm and an output power >5000mW. The laser has an entrance module, model number 9080X8941 which creates the light sheet for illumination of the seed particles. The seed particles used are

Polysciences Polybead® Microspheres with a 10 $\mu$ m mean diameter with a coefficient of variance of 10%.

### 4.3 Procedure and Set-up for Characterization Experiments

#### 4.3.1 Thermal Equilibrium Analysis

A model was developed, using all of the information from section 3, to predict the thermodynamic behavior of the LINC facility from startup to steady-state. This model was written in Python [79]. The model first builds a library of material properties as functions of temperature, length, or whatever is appropriate. This includes heat capacity, density, viscosity and other properties, mostly of water. These functions are then used to create the next level of functions which consist of things like the volumetric thermal expansion coefficient and kinematic viscosity. The next level of functions uses the prior level to build up to relevant parameters such as the Grashof number and Rayleigh number. Once the hierarchy of functions is established, one can simply call a function like the Rayleigh number and pass in a few parameters such as bulk fluid temperature, surface temperature and characteristic length. This facilitates and simplifies the calculations for correlations for the Nusselt number to find heat transfer coefficients and other important parameters for characterizing the thermodynamic behavior of the system. The model numerically solves for the surface temperature of the rods by first evaluating a range of possible temperatures and finding the difference between the “left hand side”,  $h_{lhs}$ , and the “right hand side”,  $h_{rhs}$ , at each temperature. In this case, the left hand side is shown in equation (4.1) and the right hand side is shown in equation (4.2) which come from equations (3.40), (3.41), and (3.42).

$$h_{lhs} = \frac{q''}{T_s - T_{bulk}} \quad (4.1)$$

$$h_{rhs} = \left[ \left( 0.825 + \frac{0.387 Ra_L^{1/6}}{\left[ 1 + (0.492/Pr)^{9/16} \right]^{8/27}} \right)^2 + 0.97 \frac{L}{D} \right] \left( \frac{k}{L} \right) \quad (4.2)$$

The temperature range evaluated begins from the bulk temperature and proceeds in increments of 1°C for 200 degrees. The model finds the minimum of the matrix of the difference between  $h_{lhs}$  and  $h_{rhs}$ , then examines 4000 temperature increments in a range of 2 °C below to 2°C above the initial minimum temperature index. The minimum of this matrix of the difference between  $h_{lhs}$  and  $h_{rhs}$  is then considered to be the surface temperature for that time step. The surface temperature of the rod can be used to find the Grashof and Rayleigh number at any point on the rod and indeed to analyze the profile of  $Ra$  along the rod (see section 4.3.2 for further use and significance of this). In addition to finding the surface temperature, the model uses equations (3.30), (3.36), and (3.38) to calculate the heat removed by the plate. The model updates bulk water temperature and coolant temperatures every time step based on the disparity between how much power the rods are adding and the cooling plate is removing. Ultimately, equilibrium is reached by the bulk fluid rising in temperature enough to increase the driving force to the cooling plate such that  $Q_{in} = Q_{out}$ . The model proceeds until the difference between the heat removed by the plate and the heat added by the heater rods is less than 0.001 W. The model records the history of the system and returns a text file with the heater power, cooling plate removal rate, bulk temperature and Gr and Ra at the top of the rod at each time step. In addition to this data, the model records a profile of Gr and Ra as well as boundary layer thickness in 50 incremental locations along the heater rods.

For the thermal equilibrium analysis, the objective was to determine how well the model created using the information from section 3 adequately represented reality. To begin, the tank was left to equilibrate to room temperature by sitting for an adequate amount of time. All bubbles were removed from the top of the tank by way of a needle inserted through the gasket between the copper plate and the tank. This ensures uniform, symmetrical and

consistent heat transfer from the tank to the cooler plate. For the sake of this experiment, the cooling plate was removed from the chiller loop while it cooled its reservoir. Once the chiller reached its set-point, the cooler plate is added to the chiller coolant loop and started at the same time the rods receive power. The power of the rods was recorded from the power supplies, which was relatively constant over the experimental time. Another parameter that was largely constant is the flow rate of water in the secondary loop from the chiller. The flow rate of this loop is measured with a high-accuracy flow meter as described in section 4.2.1. In order to find the heat removed by the coolant, the temperature of the inlet and outlet coolant lines from the plate are measured in the center a “cross” fitting with a probe-type thermocouple. Using the temperature difference and the water flow rate the energy added to the coolant can be calculated and compared to the model results. The temperature is also measured at the centerline of the heater rods and at 3 locations in the tank specified earlier. All temperature measurements are recorded by LabView every second and written to a data file. All of this information is then used to compare to the thermodynamic model.

#### 4.3.2 *Boundary Layer Thickness Analysis*

An important aspect of flow adjacent to surfaces is the boundary layer characteristics. Knowledge about boundary layer properties can lend to predictions about diffusion, heat transfer, turbulence and other defining characteristics of flow. The LINC facility has the capability to study the boundary layer in a natural circulation environment in great detail. One important property of the boundary layer is its physical thickness. This thickness will increase as the Rayleigh number increases along a heated surface. Of particular interest is when the boundary layer grows large enough that it is no longer isolated and begins to interact with another surface or the boundary layer from another surface.

The model described in section 4.3.1 conveniently creates a function for  $Gr$  which can be evaluated at any point  $x$  along the rod. This is used in Eckert's equation (3.44) to determine the boundary layer thickness at any point  $x$  along the rod. One of the driving design

characteristics of the LINC facility was the boundary layer thickness. It dictated the design of the size of the tank, and consequently the cooling plate and the pitch adjustment positions for the heater rod clamps. When designing the facility, it was desired that there be flexibility in testing overlapping boundary layers between two heated rods, and so a good design basis calculation was needed to estimate the thickness of said boundary layer.

In order to evaluate how accurately the LINC facility design matches the predictions using Eckert's equations for boundary layer thickness, a series of experiments were performed to determine boundary layer thickness. The following is an outline of the procedure used to collect data for the boundary layer analysis.

In the LINC facility, the polystyrene microspheres used to seed the flow have a density that is slightly greater than that of water, so over a long period of settling such as overnight, they may rest on the bottom of the tank. A custom stirring rod was designed from an aluminum rod and some gasket material to stir and coax the seed particles into suspension. The stirring rod fits through one of the heater rod holes so it is necessary to remove any bubbles collected on the top plate as a result of the removal and re-insertion of the rod due to displacement. Since this experiment relies on uniform cooling via direct contact with a cooling plate mounted on top of the tank, all bubbles were removed prior to experimentation. Sometimes when the tank water is cooling down, the water will naturally contract and draw in air from the gap around the rods. This is easily remedied by staying aware of cooling conditions and adding water as necessary. Once all seed particles were in suspension and all air was evacuated from the top of the tank, the heaters and chiller were turned on and the system was allowed to reach steady state. Generally, the system is considered to be at steady state when the bulk fluid temperature does not change more than 1% in 10 minutes. The thermal equilibrium analysis presented here in section 5.1 details how long it takes to get to steady state for several heater set points but generally equilibrium was reached in about 2 hours of startup.

Once steady state conditions were established, the camera was positioned to focus on the center plane between the two heater rods. This was accomplished by turning on the laser and focusing the camera on the seed particles illuminated by the laser sheet between the rods. The camera was calibrated using the known diameter of the heating rods so an image was taken with room lights on and a scale factor was measured to translate pixels to absolute distance. For the case of the LINC system, the flow rates are slow enough that the camera shutter rates are more than adequate to get good image pairs for velocity correlations. For this reason, for acquisition with the LINC system, the laser was simply left on continuously while the camera collected images. If it is desired to capture periodic behavior, a high frame collection rate can be used such as 100-500 Hz. For time-averaged flow patterns, one can set the image pair collection rate to 1-20 Hz, which, when collecting 100-200 images at 1 Hz will give a representation of behavior over the course of several minutes.

For the boundary layer characterization experiments, the camera was placed close enough to the heater rods such that the frame of view encompassed approximately 40 mm from top to bottom. 50 images were taken at the first location, where the bottom of the heater rods were just barely touching the bottom of the view frame. Once the images were collected, the camera was moved up using the camera mount system. The camera was moved the same distance up as was visible in the scaled images collected at the first location in order to attempt to construct a continuous vector field for the entire heated channel. Images were collected at 7 vertical settings (marked to ensure repeatability) for each power setting. A matrix of power settings was examined to start to characterize the system and see how accurate the boundary layer predictions were. Table 4.1 shows the combinations of rod powers chosen for the boundary layer analysis. The number in the test matrix refers to the test case number used to identify it.



Table 4.1 Boundary Layer Experimental Test Matrix

Case #		Right Heater		
		100W	200W	300W
Left Heater	100W	1	2	3
	200W		4	
	300W			5

Once images are recorded they are transferred from the RAM buffer on the camera to network storage system where they can be analyzed. The LINC facility uses equipment and software from Dantec Dynamics. The Dantec software includes an auto-correlation method which determines a vector for each interrogation area based on statistical algorithms. For the experiments presented here, a 16x16 pixel interrogation area was used because the camera was relatively close to the flow field, there were plenty of seed particles, and a high resolution was desired to capture boundary layer information. Each image pair is analyzed to get a vector field. In such vector fields there are inevitably interrogation areas where there are invalid or substituted vectors where there was not enough of a statistical confidence in the correlation. Much of this variability is eliminated by using the software to average all of the vector fields to greatly increase the confidence in the vector field values and eliminate random noise and variations.

#### 4.3.3 Velocity Profile Analysis

Another important metric for analyzing flow patterns is the velocity profile. The model of the system velocity profile near the heated rods consisted mostly of solutions to Eckert's equation (3.45). The velocity equation was evaluated at several locations along the heater rod in order to gain an understanding of the velocity profile progression. The velocity profile and the boundary layer are inherently linked since the boundary layer thickness (as

defined by Eckert and Jackson) is where the velocity profile drops to a threshold number. Quantification of the velocity profile is achieved by calibrating a scale factor in an image as explained earlier.

In order to compare the approximation by Eckert, measurements were taken at the same conditions and locations along the rods as were used in the calculations. Since the shape of the velocity profile was desired and not just the thickness of the boundary layer, 700 images pairs were collected to obtain a cleaner vector field and only 2 sequential, 40mm view fields were investigated for the case of each rod heated to 200W.

## 5 RESULTS AND DISCUSSION

### 5.1 Energy Balance Characterization

The energy balance was evaluated for 3 different symmetrical heat rates from the heater rods: 200W, 300W and 400W (each rod). The principle metrics for comparing the energy balance of the rod with the model were the bulk fluid temperature and the energy removed by the plate. The model of the LINC system reached an asymptotic solution for the bulk temperature and it was desired to know how well the behavior of the actual facility matched the model. Figure 5.1 shows the bulk temperature equilibrium behavior for the system and model for the rods at 200 watts each. Figure 5.2 shows the heat removed by the cooling plate, as measured by the flow rate of the coolant and temperature change from inlet to outlet of the plate. Figure 5.3 and Figure 5.4 show the equilibrium temperature and heat transfer to the plate for a power of 300W to each rod while Figure 5.5 and Figure 5.6 show the same for a power of 400W in each rod. A summary of the three energy balance cases compared with the model are presented in Figure 5.7 and Figure 5.8. One interesting feature of note in the 400W case, is the disturbances in the temperature and power. This was caused by bubbles being released by the heater rods rising and collecting on the bottom of the plate. When the bubbles were removed, the bulk tank temperature fell and the heat removed by the plate shot up. The bubbles were removed three times in this experiment, with the same result all three times.

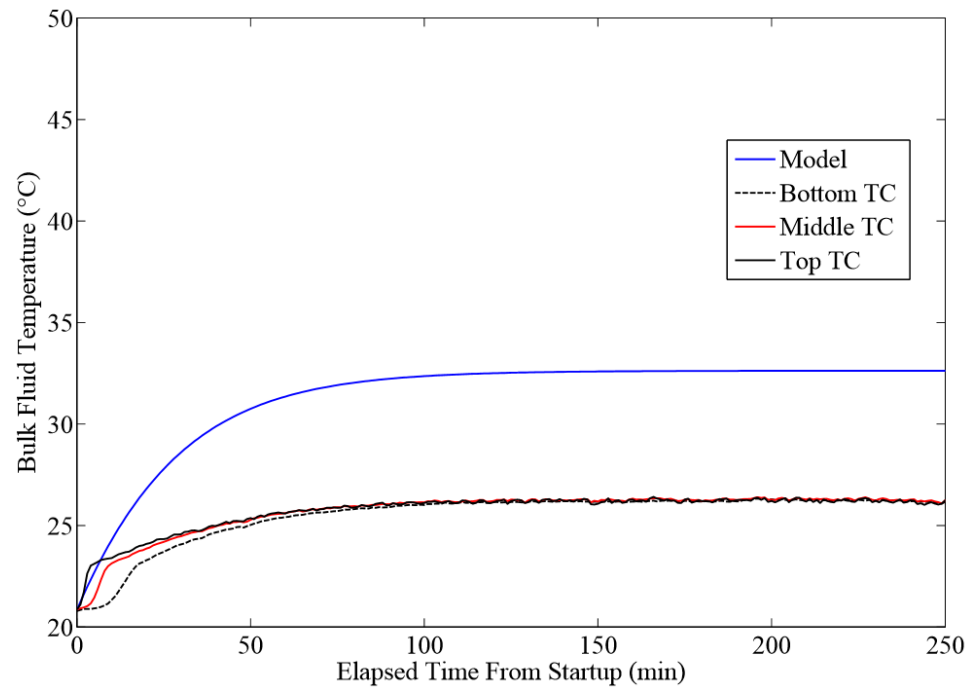


Figure 5.1 Temperature equilibrium plot for 200W rod power

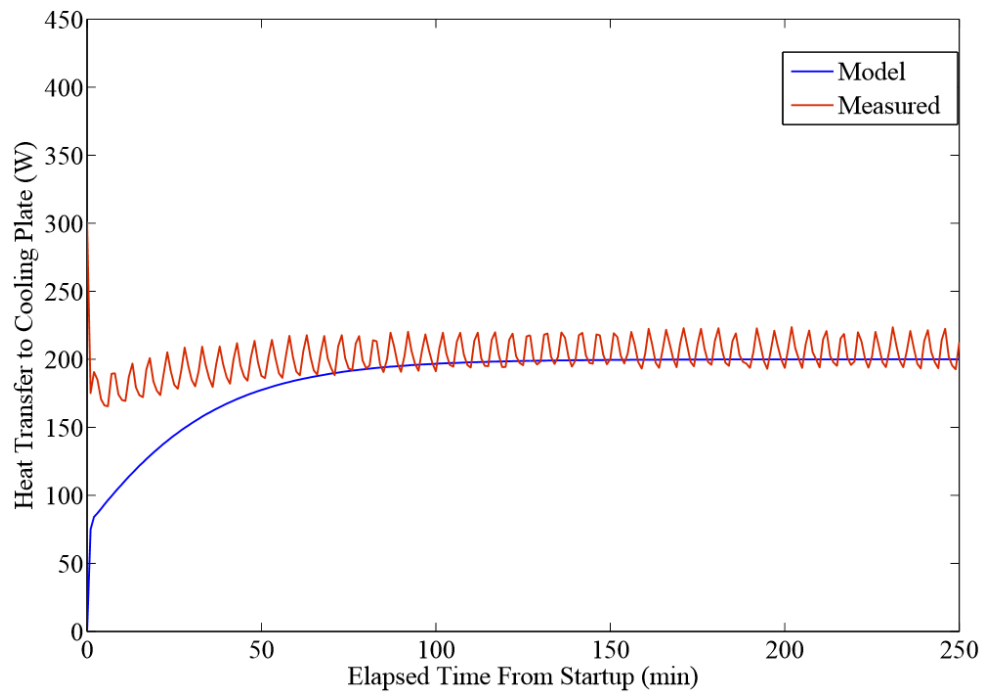


Figure 5.2 Power equilibrium plot for 200W rod power

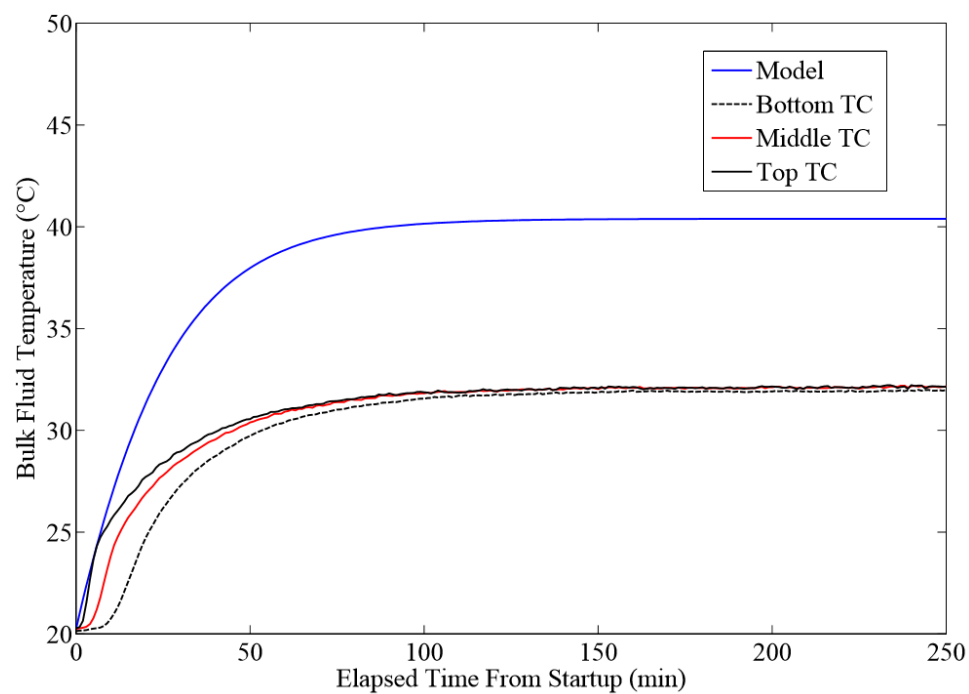


Figure 5.3 Temperature equilibrium plot for 300W rod power

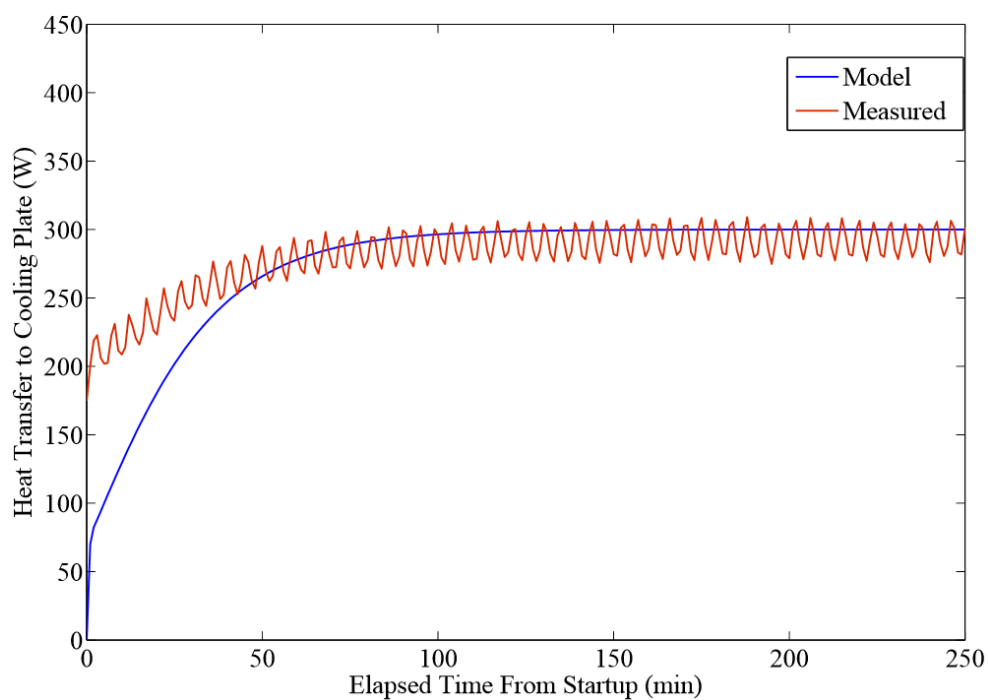


Figure 5.4 Power equilibrium plot for 300W rod power

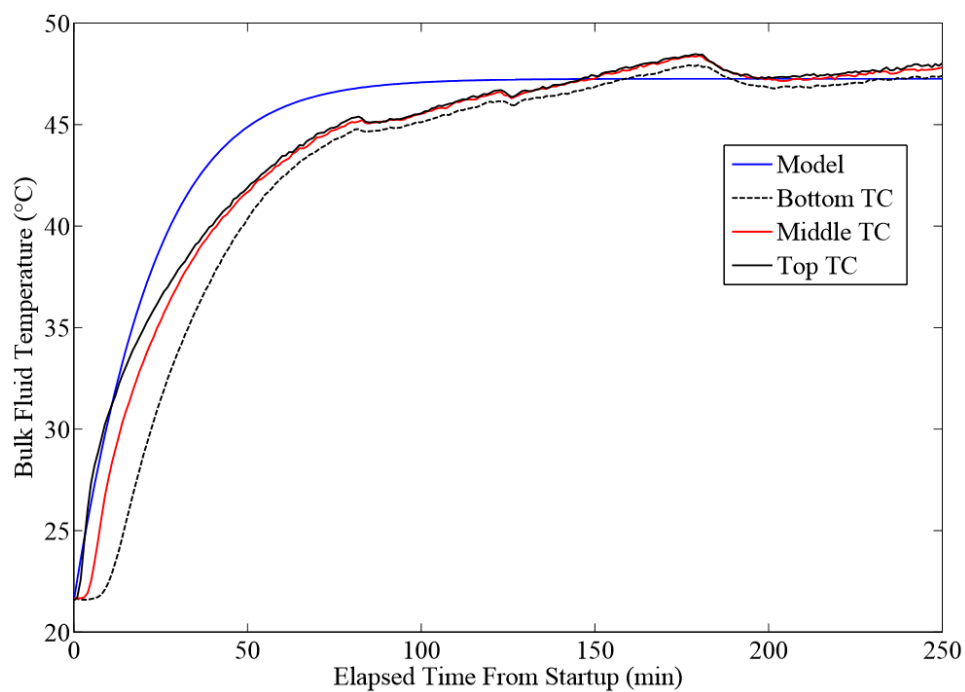


Figure 5.5 Temperature equilibrium plot for 400W rod power

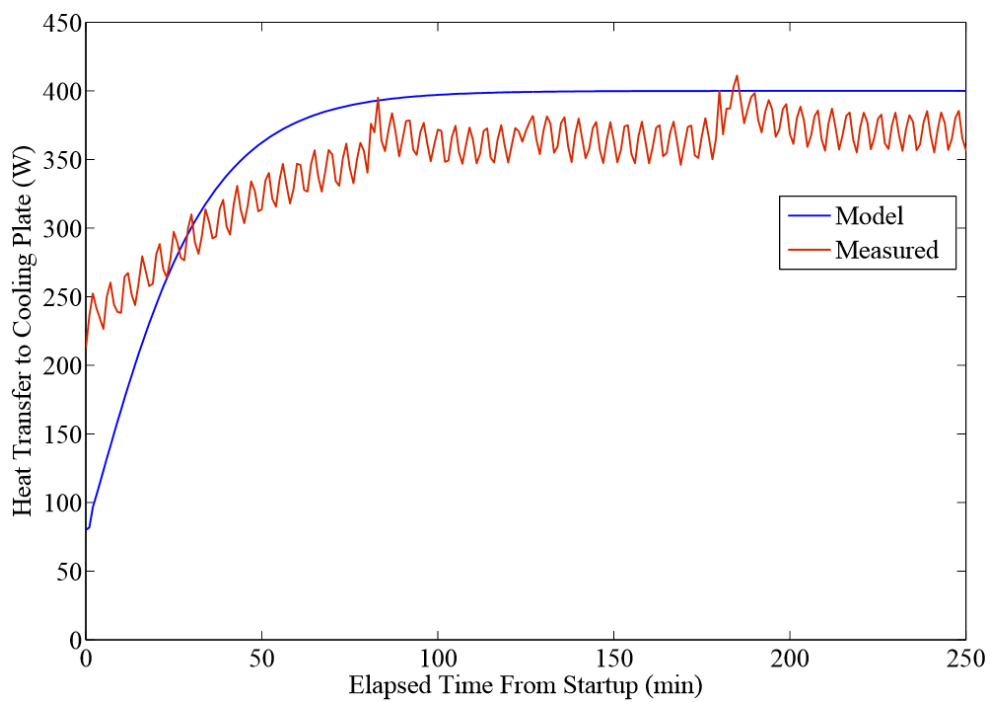


Figure 5.6 Power equilibrium plot for 400W rod power

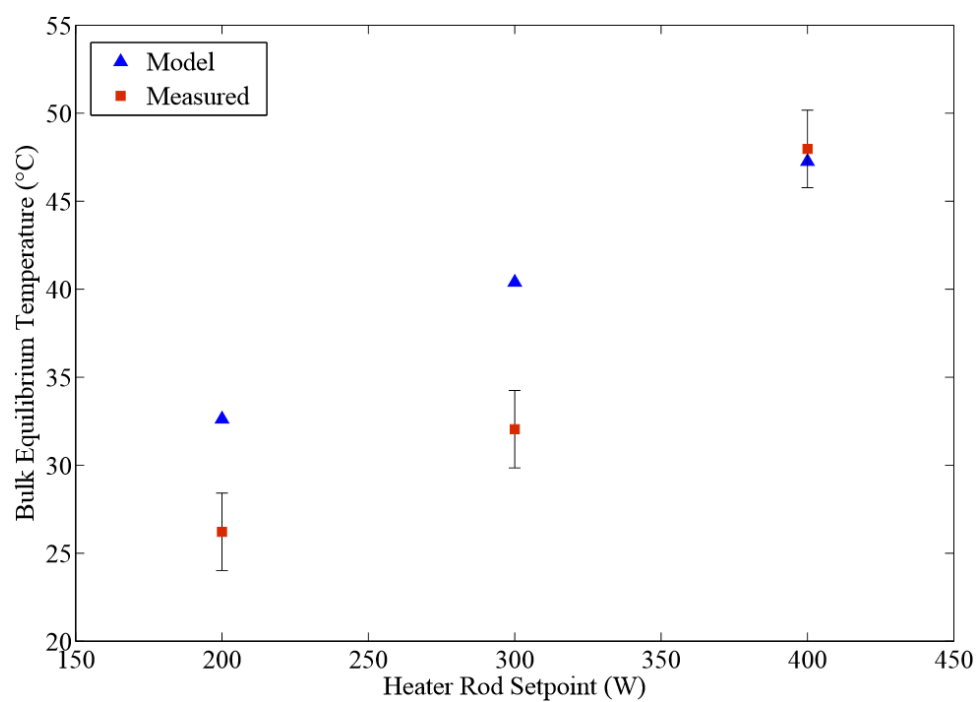


Figure 5.7 Equilibrium temperature comparison summary

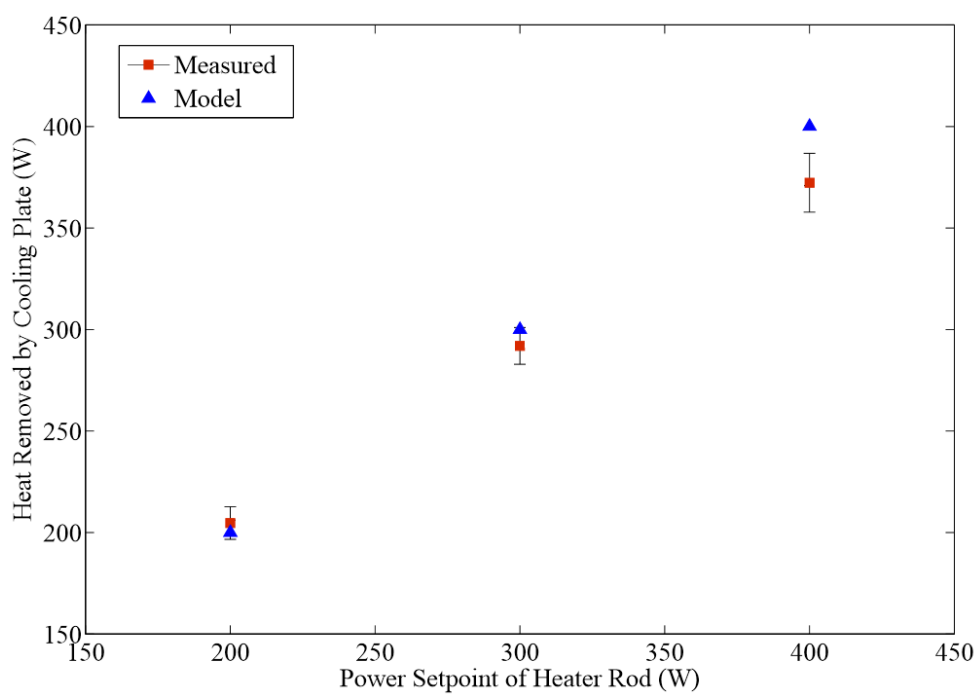


Figure 5.8 Equilibrium power comparison summary

As can be seen from the range of figures from Figure 5.1 through Figure 5.8 that the model seems justified as a first approximation of the facility. It was noticed, however, that the model is not capable of capturing some of the complex heat transfer mechanisms in the actual facility. This makes sense for several reasons listed here:

1. The Nusselt number for the bottom of the cooling plate where it contacts the water is based on the Rayleigh number of the plate only, which is 4 orders of magnitude less than that of the Rayleigh number of the rod where it meets the plate. If the Rayleigh number of the rod were used to find  $Nu$  of the plate (although this is beyond the specified use case for the correlation), the model would *over-predict* the cooling in the plate for most cases. This impingement effect is very apparent at lower cooling rates, where the actual pool temperature is much lower than that predicted by the model and in fact, lower than room temperature by as much as 7 °C. At the higher power of 400 W, the impingement seems a less dominant phenomena than at lower powers, instead it seems the entire plate becomes more significant to heat transfer with the larger temperature differential between the cooling water and the bulk water temperature.
2. The cooling water enters the plate symmetrically on each side of the heater rod channel, with the cold leg entering the center region of the plate and the hot leg leaving at the outer edge of the plate. This means that the buoyant plume mentioned in (1) impinges on the coldest portion of the cooling plate, maximizing the cooling effect of the phenomena.
3. The model makes no effort to account for cooling by natural convection on the *outside* of the tank due to conduction through the acrylic. There are also minor losses such as conduction up through the heater rod into the rod clamps, water evaporating from the cooling plate on top, or conduction from the tank to the frame that are not accounted for by the model. For the case of heat loss from the acrylic



tank to the air, this effect is expected to contribute more significantly to the disparity of the experimental data to the model at higher powers and tank temperatures, and indeed this is the case where one can see in Figure 5.6 the power drawn out by the cooling plate is less than that provided by the heater rods. It makes sense that even though the tank is being heated at lower power levels, the equilibrium temperature is barely above room temperature and so little to no driving force exists to drive heat transfer to the room. As the power level increases, the equilibrium tank temperature also increases and the temperature differential between the bulk fluid and the room becomes noticeable.

## 5.2 Boundary Layer Characterization

The boundary layer analysis was perhaps the most subjective and qualitative of the analyses performed in this study. The boundary layer can be defined as the distance from the surface at which the velocity is a certain fraction of the bulk fluid. Eckert proposes that the boundary layer edge was located where  $V=0.99V_{bulk}$ , but in a channel it is not as clear how the bulk fluid velocity can be defined. Different methods were employed to attempt to develop a consistent and definite method of determining the boundary layer thickness. One difficulty of the determination is the need to distort the image to be able to analyze it. Figure 5.9 shows a full length surface plot of  $V$  in the channel between the heated rods at a power setting of 200W with an aspect ratio that is to scale. The color coding is proportional to  $V$  where blue in this case is low to zero velocity and red represents higher velocities. This aspect ratio is unwieldy and yields little data so further images will be shown with a more appropriate scaling to best view results. Figure 5.10 shows a different aspect ratio, where the velocity behavior is more apparent.

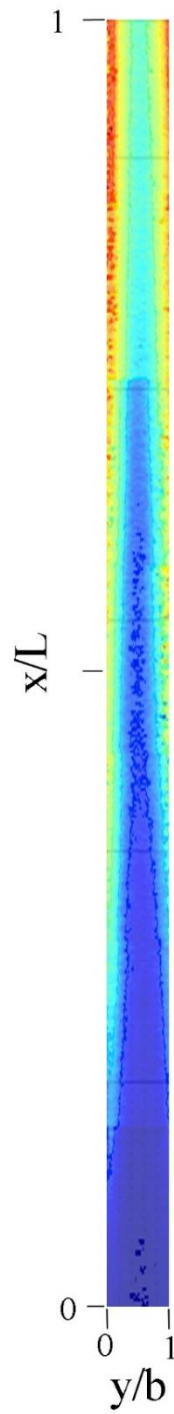


Figure 5.9 Surface/contour plot of  $V$  with accurate aspect ratio test case 4

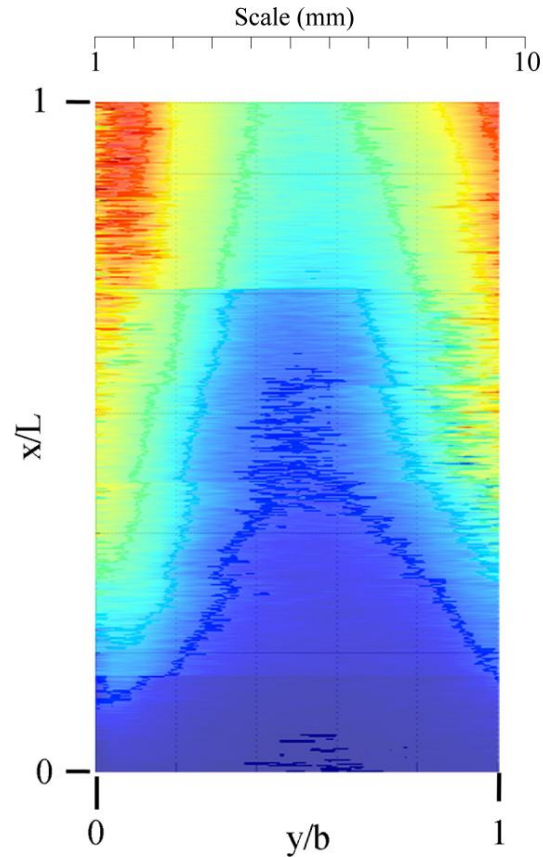


Figure 5.10 Surface/contour plot of  $V$  for full profile test case 4

In Figure 5.10, one can see slight discontinuities where vector fields were stitched together but the full profile is remarkably continuous for being taken in seven segments over the course of about 2 hours. The discontinuities are likely the result of slight camera misalignment during adjustment. The channel between rods being 9.42 mm wide, a difference of even 1 mm in adjustment laterally can alter the alignment by more than 10%.

In order to compare to Eckert, a consistent method of analysis was developed wherein the vector field was evaluated logically using a computer. The velocity in the center of the entrance region was averaged across a 4X3 grid of vectors and each vector in the map was divided by that average entrance velocity. If the value exceeded 50, then a 1 was assigned to the cell, with a 0 being assigned should the value be less than 50. This meant that the

edge of the boundary layer was found when  $0.02V=V_{entrance}$ . This logic was applied to all five rod power combination test cases. This threshold method, plotted against the boundary layer thickness predicted by Eckert is shown for all test cases in Figure 5.11 through Figure 5.15. Figure 5.16 is shown alongside the threshold method to show what a 2D representation of the velocity map looked like.

For all cases, the experimental boundary layers are similar to what Eckert and Jackson predicted in 1950. Case 5 is almost exact in its agreement with Eckert until there is a discontinuity from one camera location to the next.

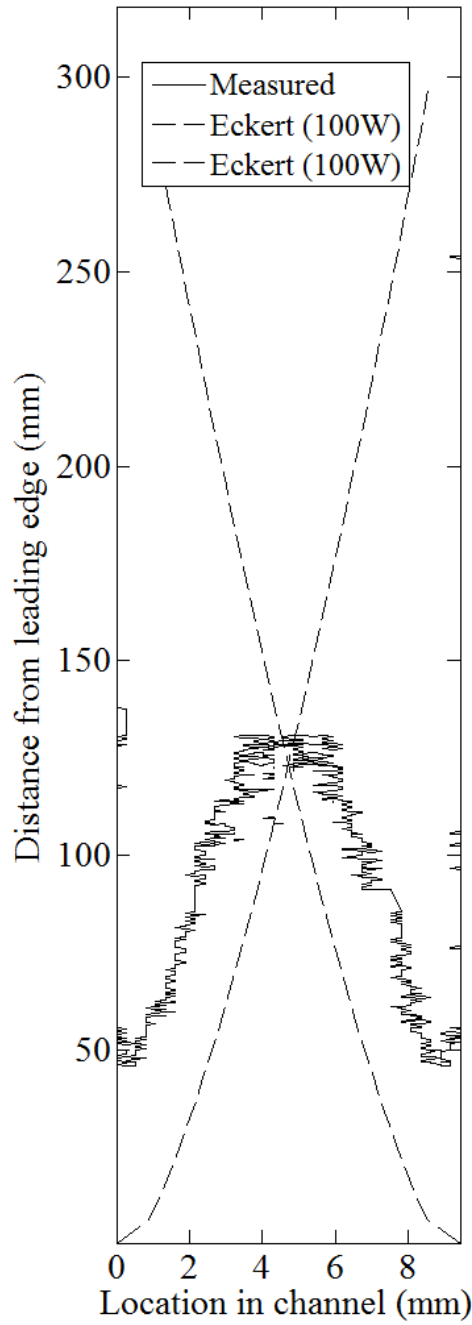


Figure 5.11 Boundary layer comparison  
Case 1

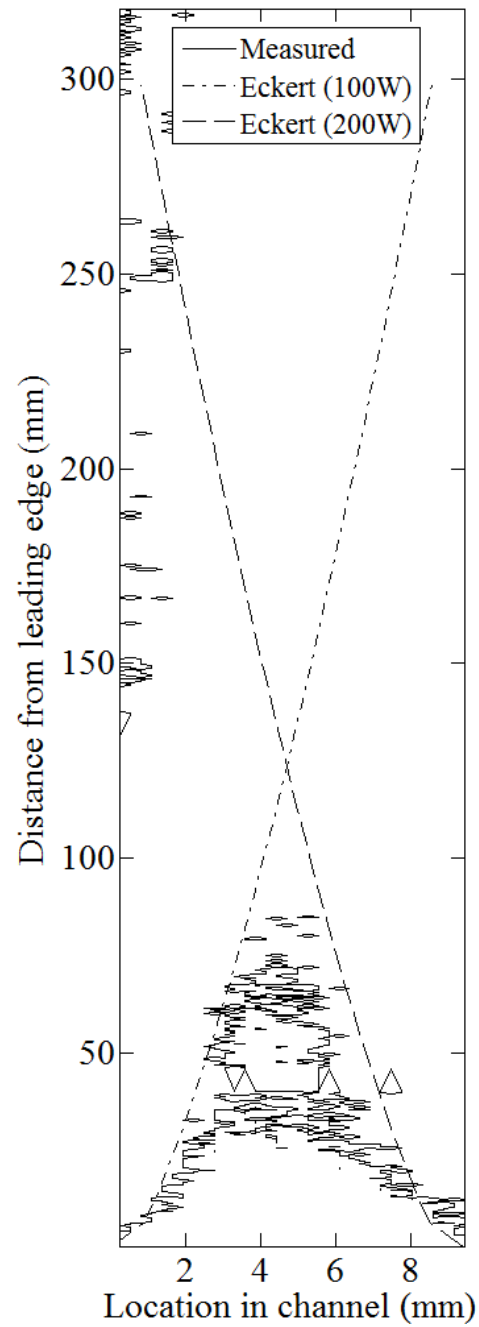


Figure 5.12 Boundary layer comparison  
Case 2

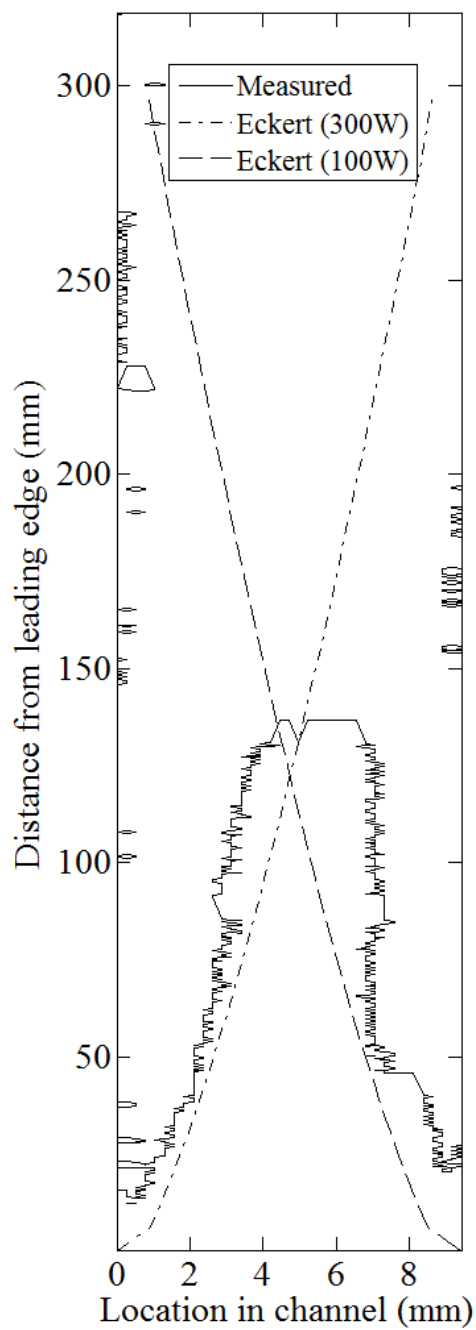


Figure 5.13 Boundary layer comparison  
Case 3

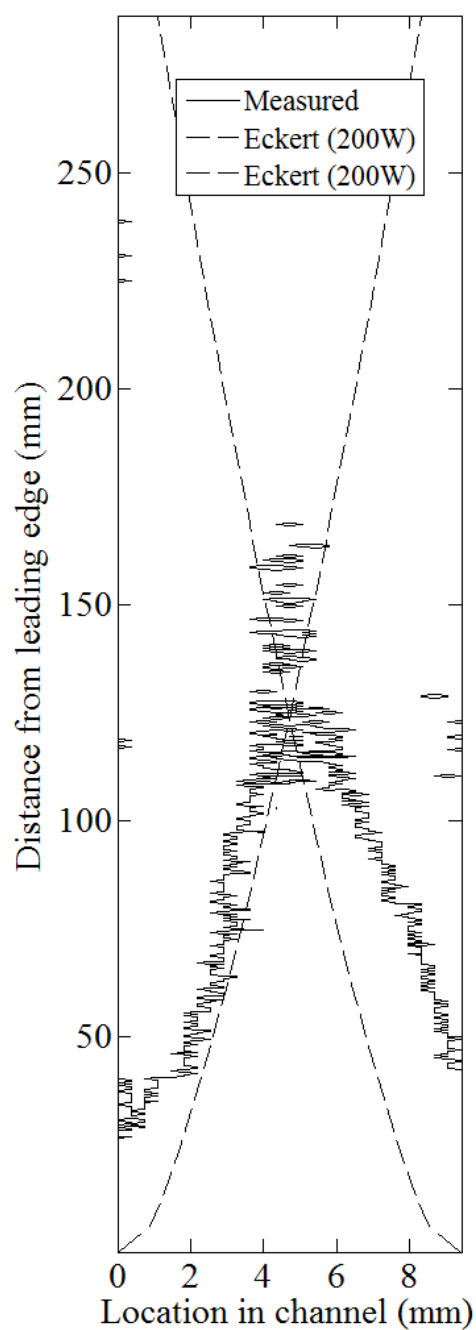


Figure 5.14 Boundary layer comparison  
Case 4

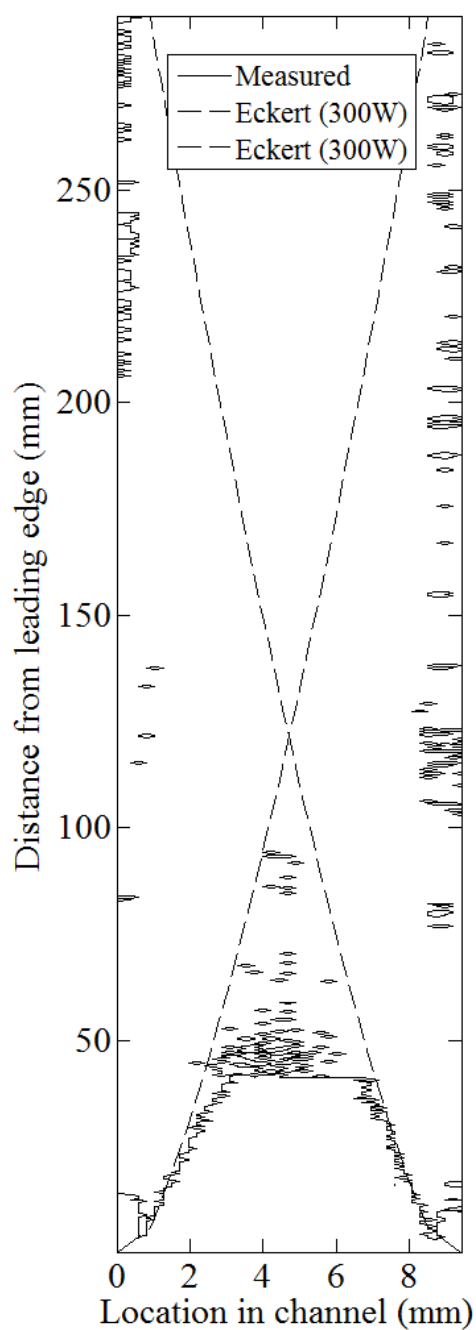


Figure 5.15 Boundary layer comparison  
Case 5

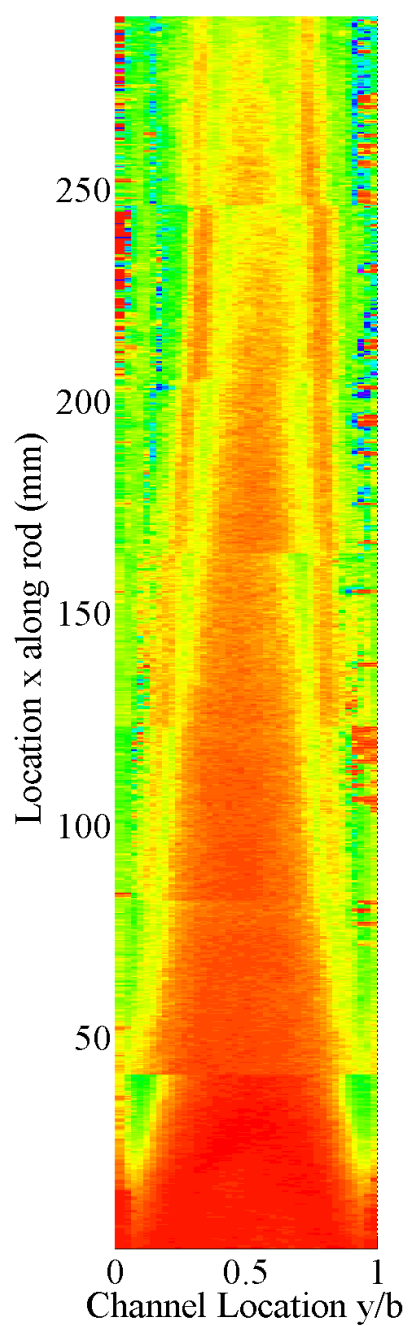


Figure 5.16 Colorized surface plot of  $V$   
for test case 5

Overall, the design basis calculations for the LINC facility with regards to the boundary layer thickness seem to be justified and have provided a reasonable estimate of the boundary layer thickness in the facility. The data seems somewhat rough on some plots, and there seemed to be some asymmetrical heating effects, but overall the facility design appears to be right in line with the behavior it was predicted to have in the boundary layer. There are several possible reasons why the measured boundary layer thickness deviated from the predicted results. The foremost of these is the applicability of Eckert and Jackson's expression to water and a cylinder. The expression is most relevant for fluids with a Prandtl number of 1, and it was a stretch to apply it to water (Pr of about 7). In addition, there is something called the transverse curvature effect that causes flow adjacent to a cylinder to differ from that adjacent to a flat plate. The effect becomes more pronounced as the ratio of  $\delta/D$  nears unity or greater and is exacerbated further at large  $x/D$  where the boundary layer is fully developed. Sparrow and Gregg suggest that the correlations for a flat plate can be used on a vertical cylinder if the condition in equation (5.1) holds.

$$\frac{D}{L} \geq \frac{35}{Gr_L^{1/4}} \quad (5.1)$$

For the case of the LINC facility heater rods, this condition is not met and so the transverse curvature has an appreciable effect on boundary layer thickness and increase in heat transfer. For these reasons, it is actually somewhat surprising that the results align as well as they do. For an investigation of the transverse curvature effect on the boundary layer thickness one would likely need to either increase the pitch or examine the outside of one of the rods (as opposed to inside the channel) to examine a full length profile without overlap from the other heater rod boundary layer.

As mentioned above, the boundary layer thickness data gathered in this study is fairly coarse and the convention used to determine the boundary layer edge ( $0.02V = V_{entrance}$ ) is somewhat arbitrary. If, for example, the definition of  $0.01V = V_{entrance}$  were chosen to



indicate the boundary layer edge, the boundary layer profiles would shift slightly up in the channel but still exhibit the same basic shape. For this reason, a different method of determining boundary layer thickness should be investigated. Due to the more complex nature of the channel between two rods, the new method should be more sophisticated than simply a threshold of velocities. The new method could consist of a multiple of the distance between the velocity maximum and the inflection point of the velocity curve (see the next section for such a curve example) taking the form of equation (5.2) where  $C$  would be a constant in the range of 2.

$$\delta = C(y_{inf} - y_{max}) + y_{max} \quad (5.2)$$

Investigating the validity of this new definition of the boundary layer thickness is beyond the scope of this work but it is of interest to the author and of value to include in future work.

### 5.3 Velocity Profile Characterization

The velocity profile was measured in detail for one heating case of 200W to each rod. The surface temperature associated with this power level at equilibrium was 58°C, however some asymmetry was noticed in the rod temperatures which had actual surface temperatures of 57.6°C and 58.6°C. A surface plot of the velocity  $V$  is shown Figure 5.17. The plot shows some asymmetry in the velocity maximum which is likely related to the temperature asymmetry, though overall the data is very clean and smooth, showing the formation of the boundary layer in the first 100 mm of channel between the heater rods. If one examines the center “valley” region of the surface plot, a nascent channel bulk velocity can be seen, which is real and quantifiable but clearly outside of the boundary layer. This is partly what introduces difficulty in defining a boundary layer thickness in terms of bulk velocity because further along the rod that center region will be indistinguishable from the boundary layer edge.

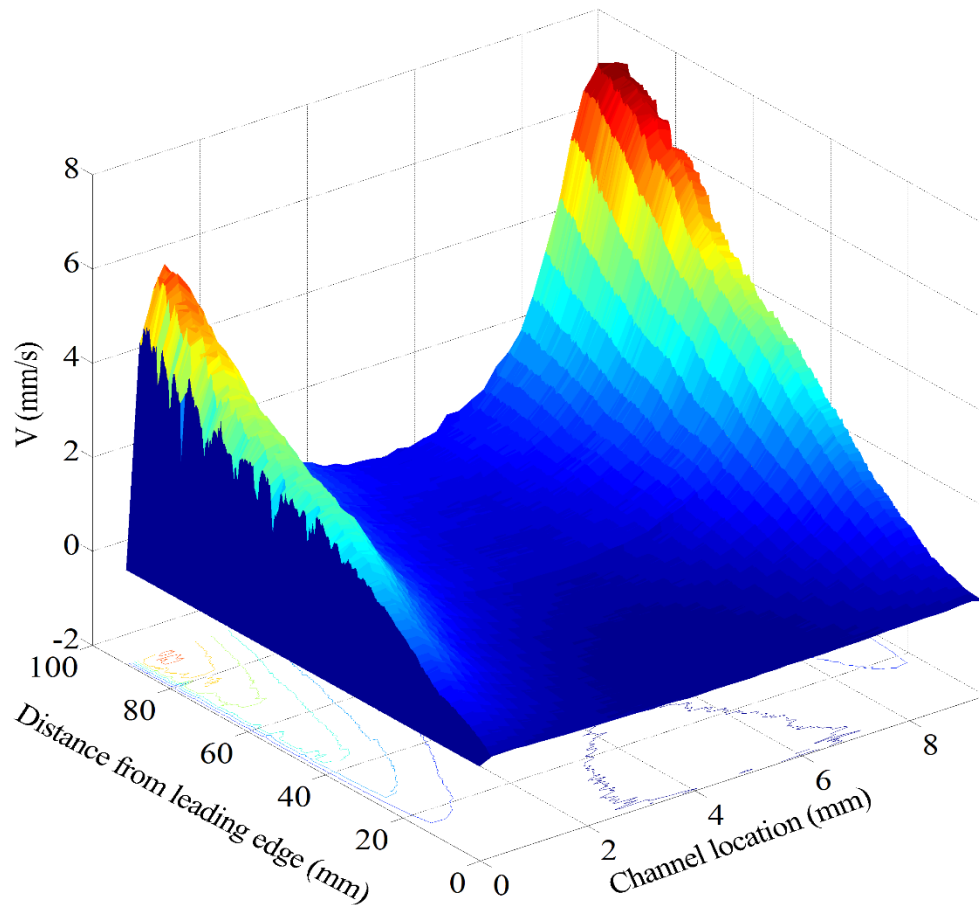


Figure 5.17 Surface plot of velocity profile for 200W power

In order to compare to the design calculations using Eckert's equations, the velocity map shown in Figure 5.17 was sampled at 10 locations from the leading edge of the heater rod: 3.05 mm, 13.22 mm, 23.07 mm, 32.93 mm, 43.08 mm, 53.12 mm, 63.04 mm, 73.20 mm, 83.05 mm, and 90.75 mm. These values were inserted into equation (3.45) along with the surface temperature of the rod and the bulk temperature of the tank to directly compare the same locations and conditions in the model and experiment. Figure 5.18 shows the velocity profile progression for one side of the channel at each of the ten x coordinates.

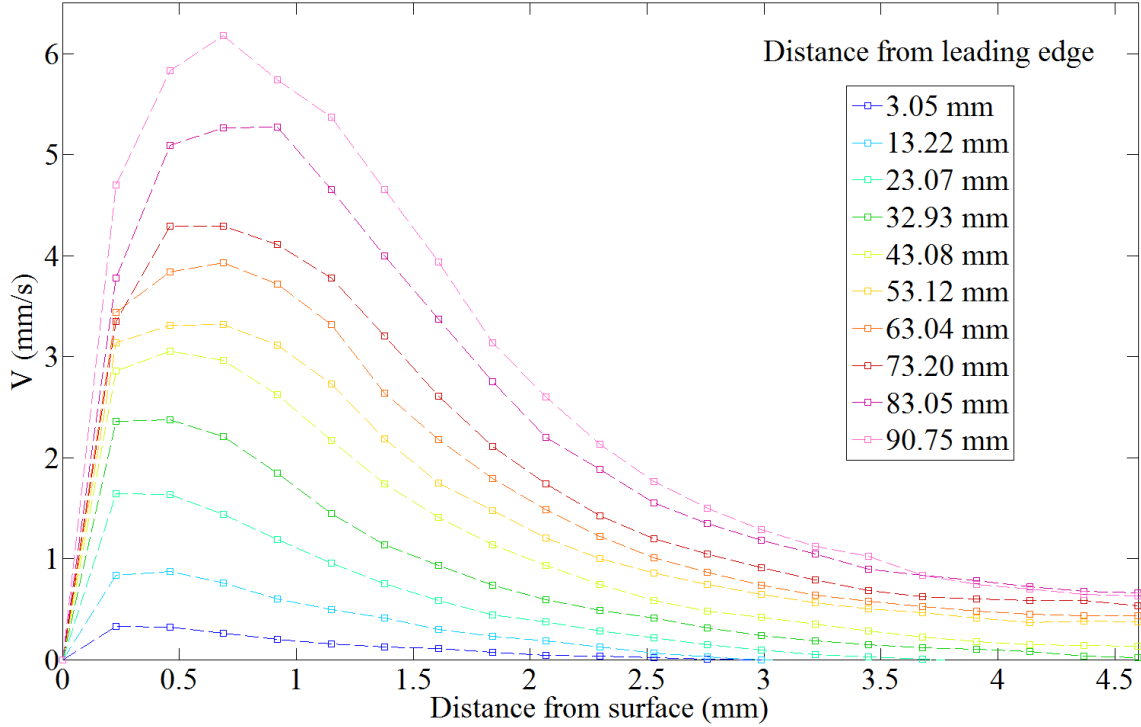


Figure 5.18 Velocity profile development in absolute units at 200W

As can be seen in Figure 5.18, the velocity profile develops through a consistent progression from the entrance region into the full-bodied velocity profile shape shown at 90.75mm. Each profile drops asymptotically to a velocity which can be thought of as the channel bulk velocity. Figure 5.19 shows the same information as Figure 5.18, except it has been normalized by dividing each velocity by the maximum velocity value in the array (found in the profile of the 90.75 mm position). The x axis was normalized by the boundary layer. For the velocity cases, it was assumed that the boundary layer edge was at the center of the channel due to the subjective nature of the actual boundary (see the preceding section for this discussion). The same profiles as predicted by the model are shown in Figure 5.20. These are normalized by the actual boundary layer thickness predicted by equation (3.44) by necessity since the nature of the velocity equation makes it only valid in the range  $0 \leq y \leq \delta$ .

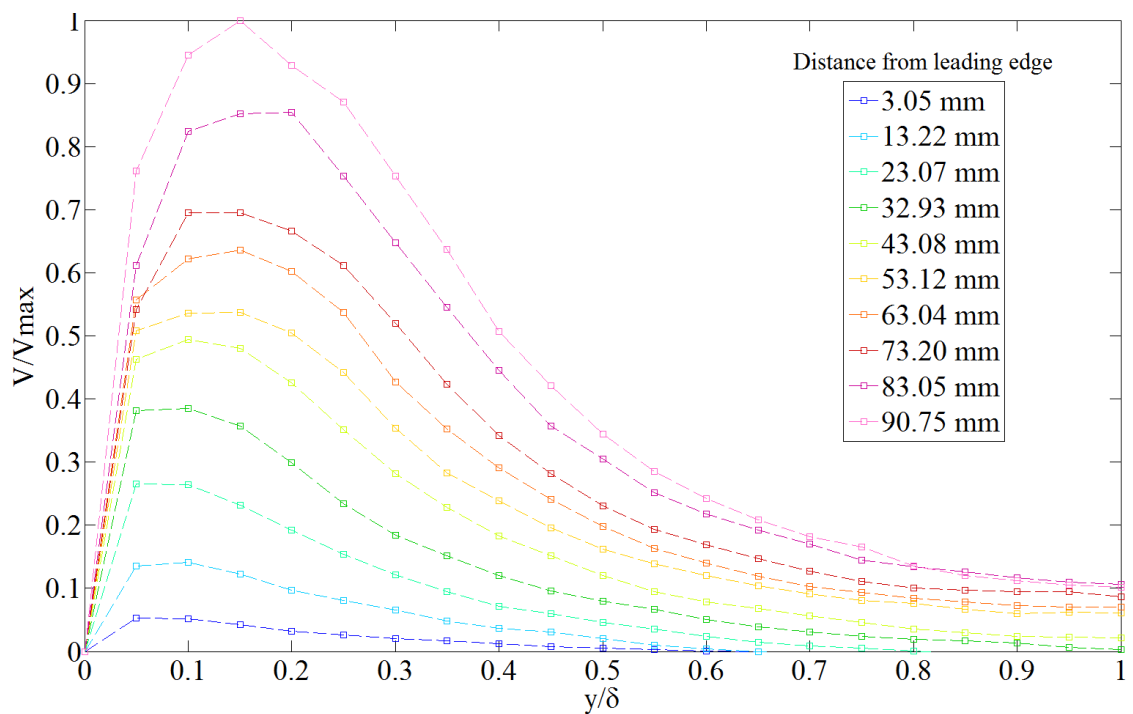


Figure 5.19 Normalized velocity profile development at 200W

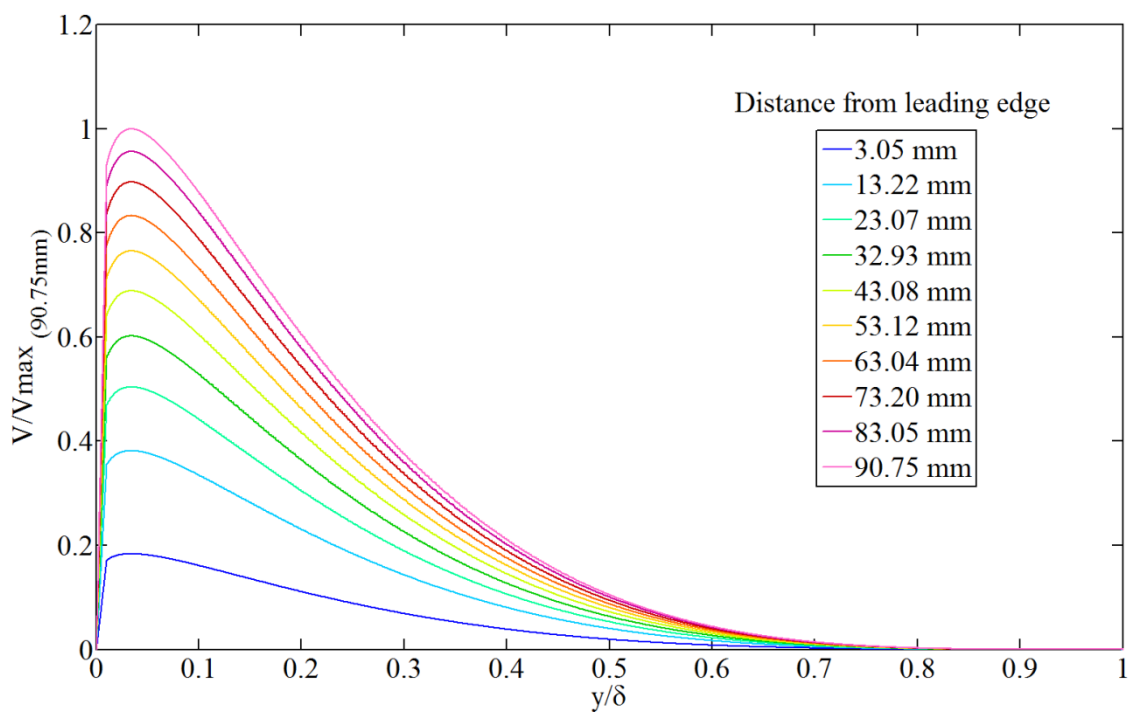


Figure 5.20 Velocity profile from Eckert

Comparing Figure 5.20 with Figure 5.19, it is observed that the two profile progressions share similarities in shape but also exhibit some important differences. One difference between the two is the lack of any channel bulk velocity from the model results. This is expected as the profile by Eckert was evaluated only from 0 to  $\delta$ , and Eckert designed his model with the assumption that the boundary layer edge occurred when  $V=0.99V_{bulk}$ , and  $V_{bulk}$  was assumed to be 0 in the model. In addition to the boundary layer edge behavior, there are differences between the model and experimental results with regard to maximum velocity progression. There seems to be an asymptotic value for the boundary layer maximum velocity, whereas the maximum velocity in the experimental results appears to be simply proportional to the distance from the leading edge. This difference can possibly be attributed to the method in which Eckert's equation was evaluated, which was by assuming the surface temperature of the rod was uniform. In the experimental facility, even though the heater rods have uniform heat flux in isothermal conditions (such as right at startup), this will likely change as a boundary layer develops and flow begins. This is because as the water is heated, and begins to rise, it continues to gain energy from the rod and heat further. The heat transfer from the rod to the water is driven by a temperature differential between the bulk fluid and the rod temperature. So, one would expect the heat flux to shift slightly downward toward the colder water entering the channel and boundary layer, and the temperature of the rod to shift up slightly at higher locations along the channel proportional to the driving force provided by warmer water temperatures in the boundary layer. For these reasons, it is in fact reassuring to see this difference between the results from the model and those of the experimental facility. It should be noted that the heat flux may actually shift up due to increased Ra and higher Nu at locations further along the rod.

Another apparent difference between the model and experimental results is the relative width of the velocity profile. The model profile is noticeably narrower than the experimental one. This is investigated further in Figure 5.21, Figure 5.22, and Figure 5.23 where the normalized velocity profile of the model and experimental values are plotted

together at successive locations measured from the leading edge of the rod. It is observed from these figures that the experimental velocity profile separates slightly from the wall as it progresses and also becomes broader near the maximum whereas the model profile maximum region remains “stuck” to the wall. The experimental results make physical sense for the LINC facility, because as the flow progresses upward along the rod, the boundary layer will get thicker. As the boundary layer thickness increases, the relative position of the maximum velocity with respect to the boundary layer width will remain roughly the same, which will lead to a maximum velocity that is further from the wall as the distance from the end of the rod increases. Also, at higher velocities the physical edge condition of  $V=0$  at the surface will tend to push the maximum  $V$  away from the wall due to friction and shear effects at the surface propagating outward. Yet another explanation for differences in velocity peak widths between Eckert and the experimental values here is the fact that a lower viscosity fluid such as air (what the formulation was based on) would be less subject to wall shear and entrainment effects, which one would imagine would cause a narrower profile than a higher viscosity fluid.

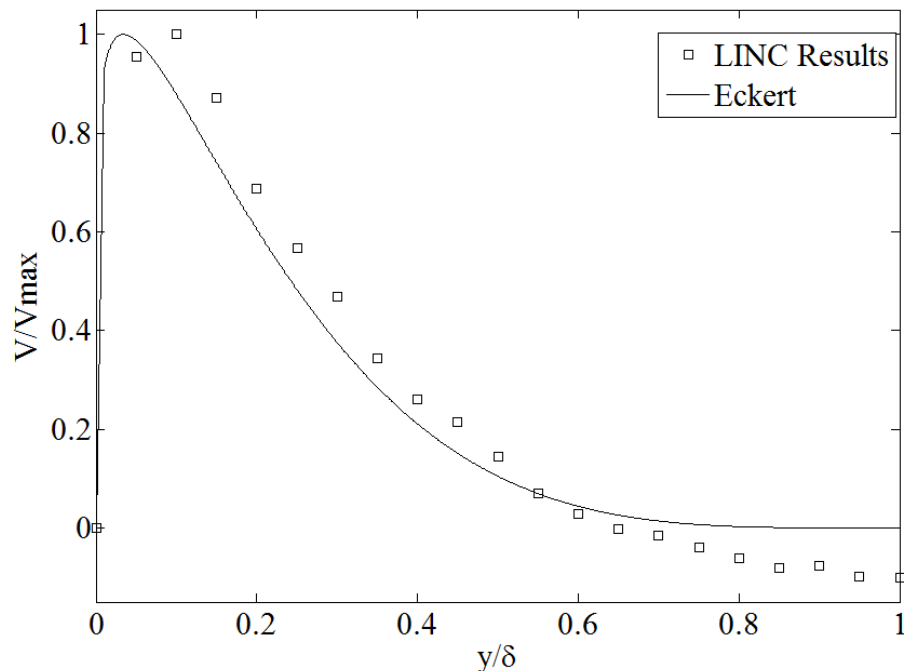


Figure 5.21 Velocity Profile at  $Ra=1.5E6$  (13.22mm from leading edge)

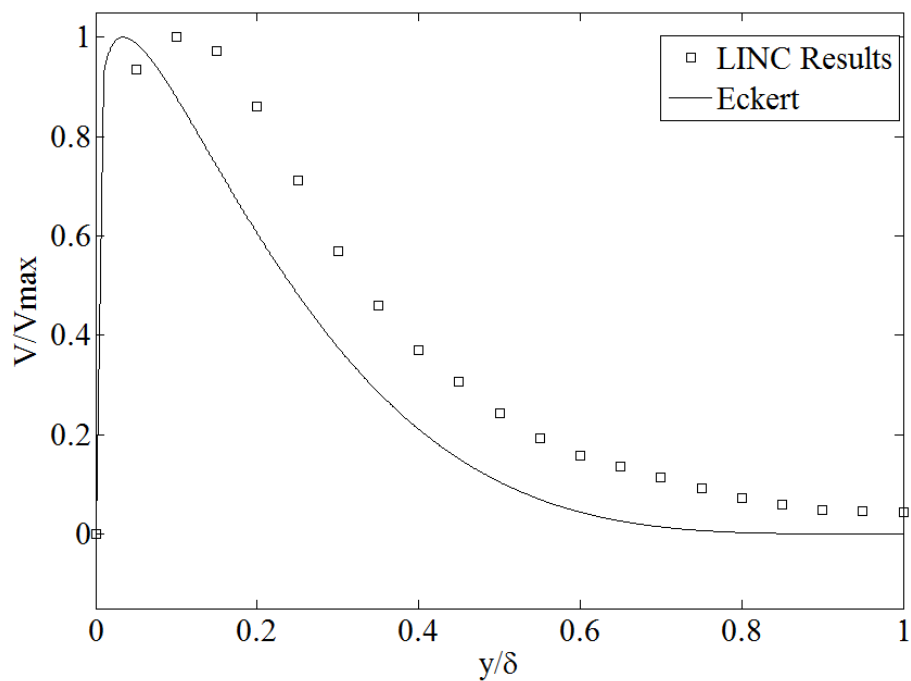


Figure 5.22 Velocity Profile at  $Ra=5.4E7$  (43.1mm from leading edge)

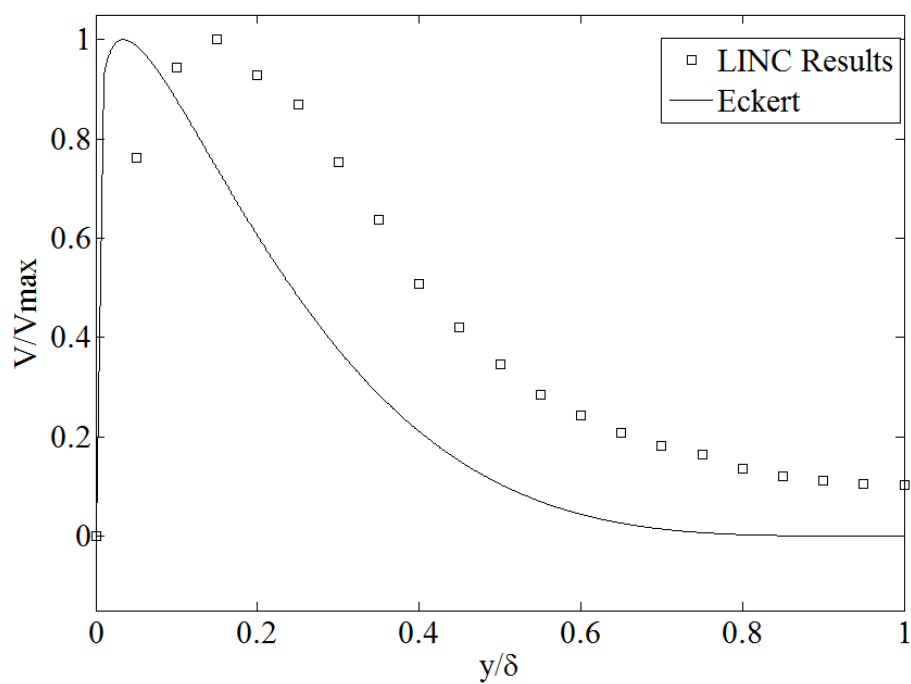


Figure 5.23 Velocity Profile at  $Ra=5E8$  (90.75mm from leading edge)

The absolute magnitude of the velocity profiles were different than those predicted by Eckert by roughly a factor of 7 (Eckert predicting the higher values), though this is understandable for a few reasons. The equations developed by Eckert were intended for use on a flat plate. In addition, the formulas presented by Eckert were assumed to be valid for  $Gr > 10^{10}$  and  $Pr$  close to unity. Both of these conditions place the work done here technically out of the bounds of the formulation as water has a Prandtl number of roughly 7 and the velocity profiles measured here had a range of  $Ra$  from  $10^7$  to  $10^9$ . Finally, the geometry of the LINC facility is fundamentally different from the general geometry configuration used to derive the velocity profile approximation in that it is not open at the top of the free convection region but rather it impinges on a cold surface, the facility uses 2 adjacent heater rods between which the velocity was measured, and again, the heated surface is a cylinder rather than a plate. There is a fundamental difference in the fluids used in many experiments in natural convection such as air and water. For a gas like air, the viscosity increases as temperature increases, but with water, the opposite is true. This could also explain the difference between the velocity profile magnitude given by Eckert and the experimental value since the evaluation by Eckert was carried out for a fluid with  $Pr$  close unity.

#### **5.4 The Nusselt Number and the Transverse Curvature Effect**

A preliminary assessment of the Nusselt number vs. Rayleigh number was also performed using the experimental results from the thermal equilibrium cases. The temperature of the surface was calculated using the measured centerline temperature and the equations from section 0 and the Nusselt number was found using the rod power and the definition of the convective heat transfer coefficient. The results were plotted against the Rayleigh number at the same location along the rod and compared against previous work. This plot and comparison is shown in Figure 5.24 where the results from Fujii [25] were experimental, the results labeled Eckert is from the correlation developed by him and Jackson in 1950 [9] and data labeled Churchill was calculated from the Nusselt correlation used in the



thermodynamic model of the LINC system presented in equation (3.40). Both correlations used the actual experimental temperatures of the bulk fluid and rod surface. The red markers are the Nusselt numbers measured at each heating case, with error bars.

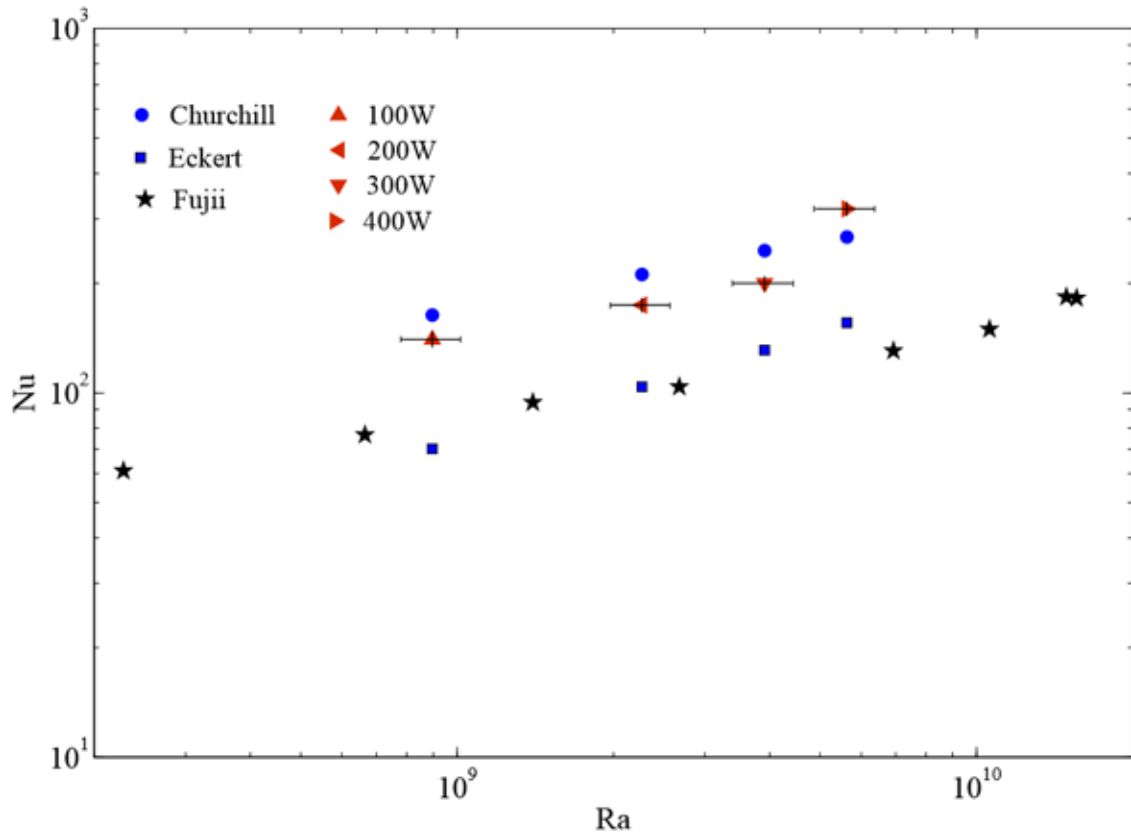


Figure 5.24 Nu vs. Ra for current work compared with prior work

The results presented in Figure 5.24 are interesting for several reasons. First is that the experimental results for Nu are higher than the results obtained by Fujii and those predicted by Eckert. This can likely be explained by differences in geometry used. Eckert and Jackson developed their correlation for a flat plate geometry. While Fujii's experiments were performed on a vertical cylinder in water, the ratio of  $L/D$  for his system was approximately 12.2 whereas the same ratio for the heater rods in the LINC facility is approximately 31.8. There is a transverse curvature effect on the heat transfer from a cylinder wherein the heat transfer is amplified with larger  $L/D$ . For this reason Fujii and

Uehara provided an upward correction for the Nusselt number for a plate when applied to a cylinder (presented as equation (3.41)). Given this, the higher Nusselt number of the LINC facility seems justified compared with prior data and the use of Churchill's flat plate correlation with the correction factor seems to approximate the facility well enough. Another interesting point on the graph is the jump in the trend from the 300W to 400W cases. It would appear that the large transverse curvature effect also contributed to an earlier than expected transition to the turbulent regime. Fujii's results indicated this transition as being in the range of  $Ra$  near  $10^{10.2}$  and here it appears to have occurred closer to  $Ra = 10^{9.4}$ . Again, this is likely the result of the transverse curvature effect and should be investigated further in future work.

## **5.5 Temperature Profiles**

While the system was at steady state for the thermal equilibrium characterization, a temperature profile was measured for each case from the surface to the wall. These profiles are presented here in Figure 5.25, Figure 5.26, and Figure 5.27 where the surface temperature was added based on a calculation from the centerline thermocouple due to the sheathed nature of the tank thermocouples.

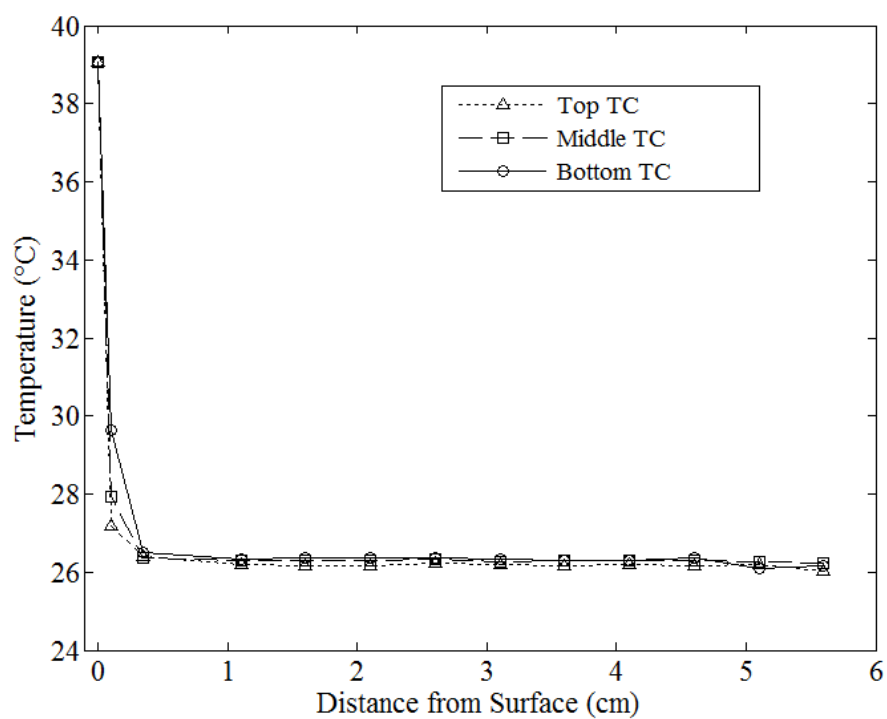


Figure 5.25 Temperature profile for 200W symmetrical heating case

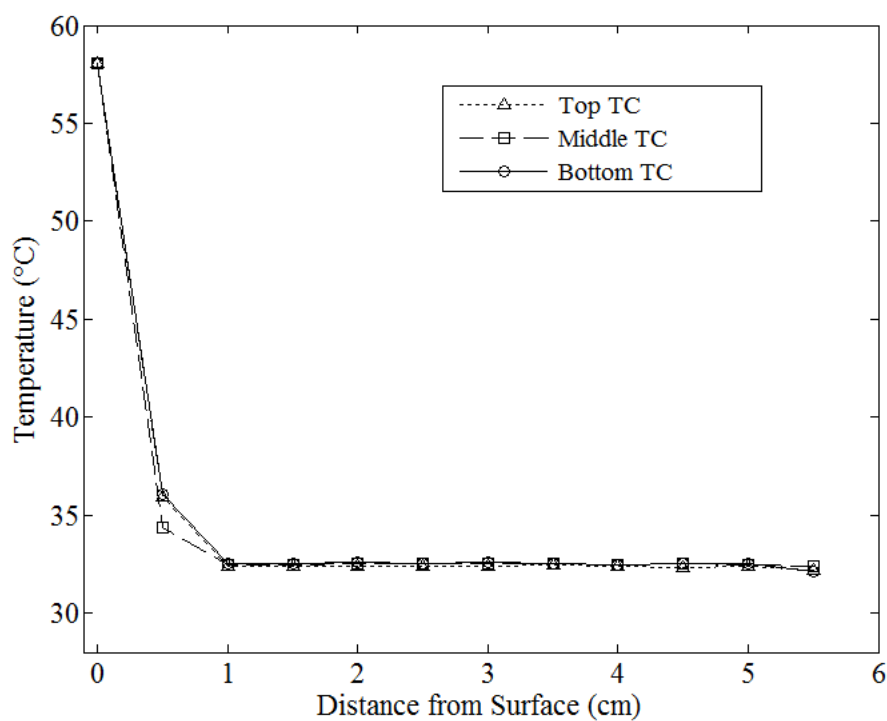


Figure 5.26 Temperature Profile for 300W symmetrical heating case

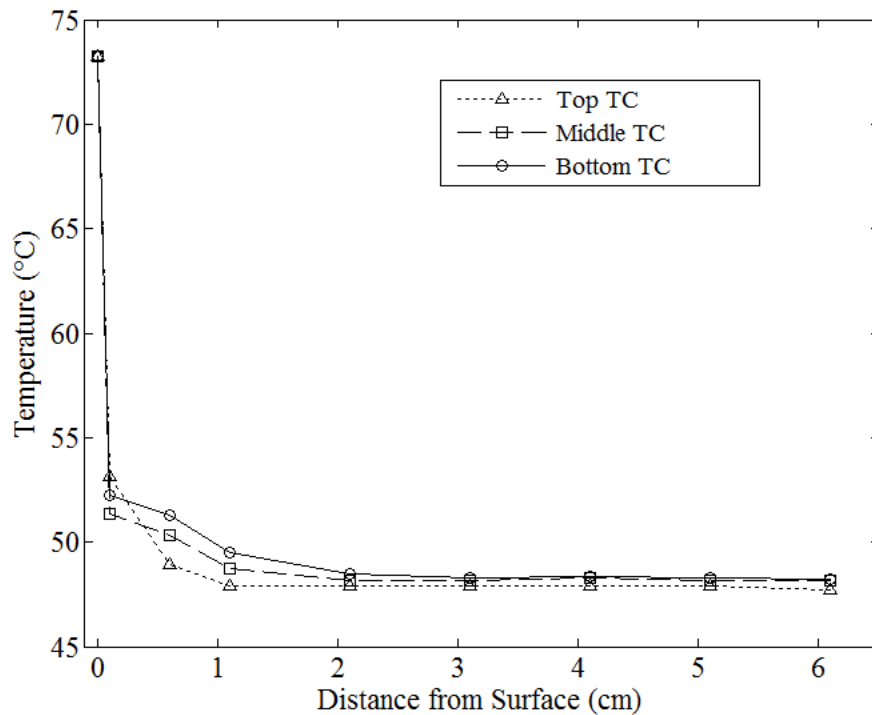


Figure 5.27 Temperature profile for 400W symmetrical heating case

While the spatial resolution of the thermocouple measurements is low, there is still valuable information that can be obtained from these temperature profile plots. First, it is interesting to see just how uniform the temperature in the tank is outside of the boundary layer. For all three heating cases, the temperatures of the thermocouples outside of the boundary layer are within 1°C of each other. This indicates excellent mixing conditions in the bulk fluid and the absence of any wall effects on the boundary layer. As a comparison, when the heater rods and cooling plate are turned off, the water tends to stratify based on temperature, leading to a temperature difference of up to 10°C in the 150 mm between the top and bottom thermocouples. Another feature one might notice on these temperature profile plots is the thermal boundary layer thickness and how much it varies between cases. While it is certainly expected to have a thicker thermal boundary at higher heat rates from the rods, the differences in these plots are primarily from the inability to obtain precise measurements by pushing the thermocouples in by hand. This was mostly due to the fact that neither the thermocouples nor the fitting they are mounted into were perfectly square

with the tank, so over a distance of 6 cm, sometimes the thermocouple tip was somewhat tangential to the heater rod as opposed to normal to the surface. Due to the limitations on acquiring an accurate temperature profile, Figure 5.25, Figure 5.26, and Figure 5.27 should be considered mostly qualitatively for the shape of the curve and how uniform the bulk fluid temperature is. The qualitative shape is in agreement with previous temperature profile measurements [25]. It will be a consideration for the future to implement a more precise temperature profile measurement system.

## 6 CONCLUSION

### 6.1 Observations

The LINC facility has been observed to perform as it was designed to do. The natural circulation loop starts up and reaches steady state quickly, reliably and consistently. The cooling plate design allows for varying of the rod pitch for the minor cost of a flat new bottom plate.

The system behavior compares fairly well with the model developed to describe the thermodynamics of the system. The cooling plate effectiveness was not captured by the model for several reasons, the most significant of which is the inability of the model to capture the cooling effect of the buoyant plume impinging on the center of the cooling plate. This caused the predicted steady state bulk temperature to be higher than the actual value measured experimentally. The case where both rods were powered at 400W, the temperature of the model and experimental results were nearly identical, but looking at the power removed by the plate, this appears to be largely from heat losses to the environment.

The expression provided by Eckert and Jackson for the boundary layer thickness was compared with measured values from the facility. The boundary layer thickness tends to be qualitative in nature unless it is defined in terms of bulk fluid velocity. In this work, the boundary layer thickness was defined as the distance from the surface where  $0.02V = V_{entrance}$  where  $V_{entrance}$  was defined as the average velocity in a region at the center of the entrance region of the channel formed by the heater rods. Using this definition, the boundary layer thickness for series of five heating rates was evaluated and compared to the values predicted by Eckert. The boundary layer thickness in the LINC system was found to be in agreement with the predicted thickness, thus validating the design basis calculations and confirming the usefulness of the LINC facility for collecting important thermal hydraulic data with regard to boundary layer thickness.

The shape of the velocity profile created by the heater rods in the LINC system was found to be in general agreement with the predictions by Eckert with a few exceptions of profile progression behavior and peak width which have been determined to be mostly from oversimplified assumptions used to calculate the predicted velocity profile and the fact that the equations by Eckert were intended to be used for a fluid near  $Pr = 1$ .

The approximation of the Nusselt number by Churchill and Chu used in the model appears to be justified, and the Nusselt number seems to be augmented due to the transverse curvature effect of these rods.

## **6.2 Relevance of Work**

The results of this paper confirm the value of the LINC facility for characterizing natural circulation flow. The behavior of the system is in general agreement with the design basis calculations used to design it. The flexibility and uniqueness of the system will allow for the contribution of much needed experimental data in the field of natural circulation adjacent to heated vertical cylinders and in channels between such cylinders. Of particular value is the application of experimental data from this facility to natural convection analysis and design for the nuclear industry. As mentioned in the introduction, natural convection is a phenomena of great interest for passively safe system design. A deeper understanding of natural convection phenomena, specifically that adjacent tonlong, heated cylinders in water is clearly of great value.

While many similarity analyses and numerical calculations have been carried out over the years on the subject of natural convection along vertical, heated plates and cylinders in open flow and channel flow, there is a disproportionately smaller amount of experimental data for the same subject. The LINC facility will be used to provide much-needed data to the body of science for further refinement of the understanding of natural convection in these configurations.

### 6.3 Experimental Limitations

There are clear limits on the applicability of the model used to design the system. The heat transfer portion of model does not account for heat exchange with the environment, it does not account for the oscillatory nature of the chiller, nor does it find the temperature profile of the heater rods. In addition, the models used by Eckert and Jackson to determine the boundary layer thickness and velocity profiles was not intended for use in such a configuration, specifically with regards to  $Pr$  of the fluid and geometry of the system. As the heat balance model and equations by Eckert and Jackson were used as a tool to design and size the LINC facility, they were not meant to be comprehensive and exact.

As far as physical limitations of the LINC facility, there are a few that limit experimental results. The first is the inability to obtain a full-length, continuous vector field of the channel between the heater rods. This is mostly due to the small seed particles reflecting such a small amount of light that by the time the camera is moved far enough away for a full-field view, the light has attenuated enough to diminish detail in particle images. There is also a resolution consideration for the camera where it wouldn't be able to obtain meaningful data for interrogation areas less than 1 mm if it were at such a wide field of view. Considering that the channel is only 9.43 mm wide, this would make the vector profile resolution very poor. For comparison, the results in section 5.3 have approximately 42 interrogation areas in the  $y$  direction between the heater rods because the camera was placed close enough to capture only 40 mm of the channel in the  $x$  direction. While a camera with a higher resolution would help in this regard, the previous issue of light attenuation would limit the benefit derived from a higher resolution camera.

Another limitation of the LINC facility in its current state is the tendency of the laser sheet between the rods to converge higher up the rod channel, leaving shadows near the rod surface. This results in a lack of data in the shadow region as no particles are being illuminated to correlate. The shadowed region can be as large as 2 mm at the top of the heated region. The issue is being investigated to determine the cause and a solution.



As mentioned in section 5.5, the temperature profiles obtained, while valuable, were still crude. The temperature profile was obtained by inserting a thermocouple into the tank through a fitting. The thermocouple probes have such a small diameter (1.58 mm) that they inevitably get bent, and the fitting that the thermocouple is mounted to is not perfectly normal to the tank wall. This configuration led to large enough margins of error in the temperature profile measurement to be unusable for boundary layer thickness analysis.

#### **6.4 Future Work**

There is much work to be done with the new natural convection facility that has been constructed. To begin, a study can be done to examine more closely the difference between the model of the cooling plate and the actual performance. The model was constructed using correlations that have been used for decades for natural circulation flow on the underside of a flat plate, though no mention could be found concerning adapting said correlation in the presence of buoyant plume impingement. The LINC facility could be used to see if, indeed this plume is having the enhanced cooling effect, as the author suspects.

Further comparisons for velocity profiles are important for characterizing the unique flow properties of the system. Vliet and Liu [80] have presented some data for water adjacent to a vertical plate that seems to be one of the few data sets available for water adjacent to a natural circulation surface, though the data they present is from a range of  $Ra$  beyond that of the normal operating conditions of the LINC facility. Since experimental data about the velocity profile in natural circulation conditions with water is clearly scarce, future work with the LINC facility will surely include publication of velocity profile and flow development behavior for a variety of conditions.

In addition to examining cooling plate behavior and velocity profiles, the LINC facility should be used in the future to examine how vertical, heated cylinders interact in natural convection conditions. Specifically, it would be of great value to determine the effect that

a power offset between the heater cylinders would have on boundary layers, Nusselt number, and flow velocity patterns normal to the cylinder. This is of special interest in the nuclear industry as nuclear fuel rods are cooled via natural convection in spent fuel pools and some reactor designs have incorporated natural convection as the primary coolant driving force. To be able to accurately model behavior in channels where a power offset is present would be of great value to the nuclear industry.

While the values of  $Nu$  vs.  $Ra$  for the LINC facility were compared to previous work, only 4 experimental data points were obtained, and in order to test the hypothesis of augmented  $Nu$  and shortened laminar region due to the transverse curvature effect, more experiments over a wider range of conditions should be performed.

While the subject of velocity profiles and boundary layer profiles were examined in this study, a detailed treatment of temperature profiles in the boundary layer was largely unaddressed. This was primarily due to the lack of a current experimental setup for acquiring such data. A better understanding of temperature profiles in a configuration such as exists in the LINC facility would be of great value to the community and would be an appropriate extension of velocity profile data acquired as well. In order to obtain high resolution temperature gradients near the rods perhaps a Laser-Induced Fluorescence (LIF) system can be implemented in the future for the temperature profile study.

Finally, this study has discussed the difficulty and seemingly arbitrary nature of the boundary layer thickness adjacent to a heated vertical surface under natural circulation conditions. It is of interest to pursue a more refined definition of the boundary layer thickness than simply the location where the velocity is a fraction of the bulk velocity. As mentioned before, a new method, perhaps using the maximum velocity location and the inflection point in the velocity profile can be used to define the boundary layer edge. This evolved definition of the boundary layer can be used to develop a new correlation to predict boundary layer thickness based on  $Ra$  and curvature.

## 7 WORKS CITED

- [1] I. William D. Magwood, "Report to Congress on Small Modular Nuclear Reactors," U.S. Department of Energy, Washington, DC, 2001.
- [2] IAEA, "Status of Small Reactor Designs Without On-Site Refuelling," International Atomic Energy Agency, Vienna, 2007.
- [3] U.S. Department of Energy Office of Nuclear Energy, "SMR Factsheet," February 2010. [Online]. Available:  
[http://nuclear.energy.gov/pdfFiles/factSheets/2011\\_SMR\\_Factsheet.pdf](http://nuclear.energy.gov/pdfFiles/factSheets/2011_SMR_Factsheet.pdf).  
 [Accessed 21 March 2012].
- [4] C. W. Forsberg, "Worldwide Advanced Nuclear Power Reactors with Passive and Inherent Safety: What, Why, How and Who," Oak Ridge National Laboratory, Oak Ridge, 1991.
- [5] L. Lorenz, "Ueber das Leitungsvermögen der Metalle für Wärme und Electricität," *Annalen der Physik*, vol. 249, no. 8, pp. 582-606, 1881.
- [6] V. H. H. Lorenz, "Die Wärmeübertragung voneiner ebene, senkrechten Platte an Öl bei natürlicher Konvektion," *Zeitchr. f. techn. Physik*, vol. 15, pp. 362-366, 1934.
- [7] A. P. Colburn and O. A. Hougen, "Studies in Heat Transmission," *Journal of Industrial and Engineering Chemistry*, vol. 22, p. 522, 1930.
- [8] W. Elenbaas, "Heat Dissipation of Parallel Plates by Free Convection," *Physica*, vol. 9, no. 1, pp. 1-28, 1942.
- [9] E. R. G. Eckert and T. W. Jackson, "Analysis of Turbulent Free-Convection Boundary Layer on Flat Plate," NACA, Cleveland, 1950.
- [10] T. v. Kármán, "On Laminar and Turbulent Friction," NACA, Washington, 1946.

- [11] S. Ostrach, "Laminar Natural-Convection Flow and Heat Transfer of Fluids Without Heat Sources in Channels with Constant Wall Temperatures," NACA, Washington, 1952.
- [12] S. Ostrach, " An analysis of laminar free-convection flow and heat transfer about a flat plate parallel to the direction of the generating body force," National Advisory Committee for Aeronautics, Cranfield, 1952.
- [13] E. M. Sparrow and J. L. Gregg, "Laminar-Free-Convection Heat Transfer from the Outer Surface of a Vertical Circular Cylinder," *Transactions of the American Society of Mechanical Engineers*, vol. 78, pp. 1823-1829, 1956.
- [14] E. M. Sparrow and J. L. Gregg, "Laminar Free Convection From a Vertical Plate with Uniform Surface Heat Flux," *Transactions of the American Society of Mechanical Engineers*, vol. 78, pp. 435-440, 1956.
- [15] K. Millsaps and K. Pollhausen, "The Laminar Free-Convective Heat Transfer From the Outer Surface of a vertical Circular Cylinder," *Journal of Aeronautical Sciences*, vol. 25, pp. 357-360, 1958.
- [16] J. R. Bodoia and J. F. Osterle, "The Developmet of Free Convection Between Heater Vertical Plates," *Journal of Heat Transfer*, vol. 84, no. 1, pp. 40-44, 1962.
- [17] H. R. Nagendra, M. A. Tirunaryanan and A. Ramachan, "Laminar Free Convection from Vertical Cylinders with Uniform Heat Flux," *Journal of Heat Transfer*, vol. 92, no. 1, pp. 191-195, 1970.
- [18] T. Fujii and H. Uehara, "Laminar Natural-Convective Heat Transfer from the Outer Surface of a Vertical Cylinder," *International Journal of Heat and Mass Transfer*, vol. 13, pp. 607-615, 1970.
- [19] W. Aung, L. Fletcher and V. Sernas, "Developing Laminar Free Convection Between Vertical Flat Plates with Asymmetric Heating," *International Journal of Heat and Mass Transfer*, vol. 15, no. 11, pp. 2293-2308, 1972.

- [20] T. Cebeci, "Laminar-Free-Convective-Heat Transfer from the Outer Surface of a Vertical Slender Circular Cylinder," *Heat Transfer: Proceedings of Fifth International Conference*, vol. 3, pp. 15-19, 1974.
- [21] J. P. Narain, "Free and Forced Convective Heat Transfer from Slender Cylinders," *Letters in Heat and Mass Transfer*, vol. 3, pp. 21-30, 1976.
- [22] H. R. Nagendra, M. A. Tirunarayanan and A. Ramachandran, "Free convection heat transfer from vertical cylinders and wires," *Chemical Engineering Science*, vol. 24, pp. 1491-1495, 1969.
- [23] R. Cheesewright, "Turbulent Natural Convection from a Vertical Plane Surface," *Journal of Heat Transfer*, vol. 90, no. 1, pp. 1-8, 1968.
- [24] Kato, "On the Turbulent Heat Transfer by Free Convection from a Vertical Plate," *International Journal of Heat and Mass Transfer*, vol. 11, pp. 1117-1125, 1968.
- [25] T. Fujii, M. Takeuchi, K. Suzaki and H. Uehara, "Experiments on Natural-Convection Heat Transfer From the Outer Surface of a Vertical Cylinder to Liquids," *International Journal of Heat and Mass Transfer*, vol. 13, pp. 753-787, 1970.
- [26] W. J. Minkowycz and E. M. Sparrow, "Local Nonsimilar Solutions for Natural Convection on a Vertical Cylinder," *Journal of Heat Transfer*, vol. 96, no. 2, pp. 178-183, 1974.
- [27] H. B. Mason and R. A. Seban, "Numerical Prediction for Turbulent Free Convection from Vertical Surfaces," *International Journal of Heat and Mass Transfer*, vol. 17, no. 11, pp. 1329-1336, 1974.
- [28] S. W. Churchill, "Correlating equations for laminar and turbulent free convection from a horizontal cylinder," *International Journal of Heat and Mass Transfer*, pp. 1049-1053, 1975.

- [29] R. Cheesewright and K. S. Doan, "Space-Time Correlation Measurements in a Turbulent Natural Convection Boundary Layer," *International Journal of Heat and Mass Transfer*, vol. 21, pp. 911-921, 1978.
- [30] W. K. George Jr. and S. P. Capp, "A Theory for Natural Convection Turbulent Boundary Layers Next to Heated Vertical Surfaces," *International Journal of Heat and Mass Transfer*, vol. 22, no. 6, pp. 813-826, 1979.
- [31] E. Griffiths and A. H. Davis, "The Transmission of Heat by Radiation and Convection, D.S.I.R. Special Report 9," British Food Investigation Board, London, 1922.
- [32] S. V. Patankar and D. B. Spalding, *Heat and Mass Transfer in Boundary Layers*, 2nd Ed., London: Intertext Books, 1970.
- [33] T. S. Chen and C. F. Yuh, "Natural Convection Along a Vertical Cylinder," *International Journal of Heat and Mass Transfer*, vol. 23, no. 4, pp. 451-461, 1980.
- [34] W. M. To and J. A. C. Humphrey, "Numerical simulation of buoyant, turbulent flow - 1. Free convection along a heated, vertical, flat plate," *International Journal of Heat and Mass Transfer*, vol. 29, no. 4, pp. 573-592, 1986.
- [35] K. Velusamy and V. K. Garg, "Transient natural convection over a heat generating vertical cylinder," *International Journal of Heat and Mass Transfer*, vol. 35, no. 5, pp. 1293-1306, 1992.
- [36] M. R. Gavara, P. Dutta and K. N. Seetharamu, "Mixed convection adjacent to non-isothermal vertical surfaces," *International Journal of Heat and Mass Transfer*, vol. 55, no. 17-18, pp. 4580-4587, 2012.
- [37] P. Ganesan and H. P. Rani, "Transient natural convection along vertical cylinder with Heat and Mass transfer," *Heat and Mass Transfer*, vol. 33, pp. 449-455, 1998.

- [38] T. Yilmaz and S. M. Fraser, "Turbulent natural convection in a vertical parallel-plate channel with asymmetric heating," *International Journal of Heat and Mass Transfer*, vol. 50, pp. 2612-2623, 2007.
- [39] T. Tsuji and Y. Nagano, "Velocity and Temperature Measurements in a Natural Convection Boundary Layer Along a Vertical Flat Plate," *Experimental Thermal and Fluid Science*, vol. 2, pp. 208-215, 1989.
- [40] J. H. Merkin, "Natural-convection boundary-layer flow on a vertical surface with Newtonian heating," *International Journal of Heat and Fluid Flow*, vol. 15, no. 5, pp. 392-398, 1994.
- [41] M. Z. Abedin, T. Tsuji and J. Lee, "Turbulence characteristics and vortical structures in combined-convection boundary layers along a heated vertical flat plate," *International Journal of Heat and Mass Transfer*, vol. 55, pp. 3995-4002, 2012.
- [42] S. C. Saha, R. J. Brown and Y. T. Gu, "Prandtl number scaling of the unsteady natural convection boundary layer adjacent to a vertical flat plate for  $Pr > 1$  subject to ramp surface heat flux," *International Journal of Heat and Mass Transfer*, vol. 55, no. 23-24, pp. 7046-7055, 2012.
- [43] M. Miyamoto, Y. Katoh, J. Kurima and H. Sasaki, "Turbulent Free Convection Heat Transfer from Vertical Parallel Plates," *Heat Transfer*, vol. 4, no. 8, pp. 1953-1598, 1986.
- [44] D. Naylor, J. M. Floryan and J. D. Tarasuk, "A Numerical Study of Developing Free Convection Between Isothermal Vertical Plates," *Transactions of the ASME*, vol. 113, pp. 620-626, 1991.
- [45] A. G. Fedorov and R. Viskanta, "Turbulent natural convection heat transfer in an asymmetrically heated, vertical parallel-plate channel," *International Journal of Heat and Mass Transfer*, vol. 40, no. 16, pp. 3849-3860, 1997.

- [46] E. Darie, S. Kimara and A. Okajima, "Natural Convection Heat Transfer in an Asymmetrically Heated vertical Channel Controlled by Through Flows," *JSME International Journal*, vol. 41, no. 1, pp. 227-232, 1998.
- [47] M. A. Habib, S. A. M. Said, S. A. Ahmed and A. Asghar, "Velocity characteristics of turbulent natural convection in symmetrically and asymmetrically heated vertical channels," *Experimental Thermal and Fluid Science*, vol. 26, pp. 77-87, 2002.
- [48] Incropera, DeWitt, Bergman and Lavine, *Fundamentals of Heat and Mass Transfer*, 6th ed., John Wiley & Sons Inc., 2007.
- [49] Churchill, "Free Convection Around Immersed Bodies," in *Heat Exchanger Design Handbook*, New York, Begell House, 2002, pp. 2.5.7-23.
- [50] B. Gebhart, Y. Jaluria, R. L. Mahajan and B. Sammakia, *Buoyancy-Induced Flows and Transport*, New York: Hemisphere Publishing Corporation, 1988.
- [51] R. J. Adrian and J. Westerweel, *Particle Image Velocimetry*, New York: Cambridge University Press, 2011.
- [52] L. Prandtl, "Über Flüssigkeitsbewegung bei sehr kleiner Reibung," Heidelberg, Leipzig, 1904.
- [53] R. J. Adrian, "Scattering particle characteristics and their effect on pulsed laser measurements of fluid flow: speckle velocimetry vs. particle image velocimetry," *Applied Optics*, vol. 23, pp. 1690-1691, 1984.
- [54] C. J. D. Pickering and N. Halliwell, "LSP and PIV: photographic film noise," *Applied Optics*, vol. 23, pp. 2961-2969, 1984.
- [55] R. J. Adrian, "Bibliography of particle image velocimetry using imaging methods:1917-1995 TAM Report 817," University of Illinois, Chicago, 1996.
- [56] M. M. Sutton, W. H. R. W. J. Wolters and S. R. Macneil, "Determination of displacements using an improved digital correlation method," *Optical Engineering*, vol. 1, pp. 113-139, 1983.



- [57] T. Morck, P. E. Andersen and C. H. Westergaard, "Processing speed of photorefractive optical correlators in PIV-processing," in *Laser techniques and applications in fluid mechanics*, New York, Springer, 1993, pp. 227-242.
- [58] A. Vogt, F. Reichel and J. Kompenhans, "A compact and simple all optical evaluation method for PIV recordings," in *Developments in Laser Techniques and applications to fluid mechanics*, New York, Springer, 1996, pp. 423-437.
- [59] C. E. Willert and M. Gharib, "Digital particle image velocimetry," *Experiments in Fluids*, vol. 10, pp. 181-193, 1991.
- [60] J. Westerweel, "Analysis of PIV interrogation with low pixel resolution," in *Optical diagnostics in fluid and thermal flow*, Bellingham, SPIE, 1993, pp. 624-635.
- [61] L. M. Lourenco, S. P. Gogigeni and R. T. Lasalle, "On-line particle image velocimeter: an integrated approach," *Applied Optics*, vol. 33, pp. 2465-2470, 1994.
- [62] B. Chen, F. Mikami and N. Nishikawa, "Experimental studies on transient features of natural convection in particles suspensions," *International Journal of Heat and Mass Transfer*, vol. 48, pp. 2933-2942, 2005.
- [63] F. Corvaro, M. Paroncini and M. Sotte, "PIV and numerical analysis of natural convection in tilted enclosures filled with air and with opposite active walls," *International Journal of Heat and Mass Transfer*, vol. 55, pp. 6349-6362, 2012.
- [64] S. Grafrønningen, A. Jensen and B. A. P. Reif, "PIV investigation of buoyant plume from natural convection heat transfer," *International Journal of Heat and Mass Transfer*, pp. 4975-4987, 2011.
- [65] S. Grafrønningen and A. Jensen, "Natural convection heat transfer from two horizontal cylinders at high Rayleigh numbers," *International Journal of Heat and Mass Transfer*, vol. 55, no. 21-22, pp. 5552-5564, 2012.

- [66] M. Raffel, C. E. Willert, S. T. Wereley and J. Kompenhans, Particle Image Velocimetry: A Practical Guide 2nd Ed., Berlin Heidelberg: Springer-Verlag, 2007.
- [67] J. V. Sengers and J. R. Watson, "Improved International Formulations for the Viscosity and Thermal Conductivity of Water Substance," *Journal of Physical and Chemical Reference Data*, vol. 15, no. 4, pp. 1291-1315, 1986.
- [68] L. Haar, J. S. Gallagher and G. S. Kell, NBS/NRC Steam Tables: Thermodynamic and Transport Properties and Computer Programs for Vapor and Liquid States of Water in SI Units, vol. 40, Washington: Hemisphere Publishing Corporation, 1984, pp. 1001-1004.
- [69] W. Wagner and A. Pruss, "The IAPWS Formulation 1995 for the Thermodynamic Properties of Ordinary Water Substance for General and Scientific Use," *Journal of Physical and Chemical Reference Data*, vol. 31, no. 2, pp. 387-536, 2002.
- [70] Special Metals Corporation, "Special Metals," September 2004. [Online]. Available:  
<http://www.specialmetals.com/documents/Incoloy%20alloys%20800H%20800HT.pdf>. [Accessed 20 May 2103].
- [71] G. A. Slack, "Thermal Conductivity of MgO, Al<sub>2</sub>O<sub>3</sub>, MgAl<sub>2</sub>O<sub>4</sub>, and Fe<sub>3</sub>O<sub>4</sub> Crystals from 3 to 300K," *Physical Review*, vol. 126, no. 2, pp. 427-441, 1962.
- [72] V. Gnielinski, "New equations for heat and mass transfer in turbulent pipe and channel flow," *International Chemical Engineering*, vol. 16, no. 2, pp. 359-368, 1976.
- [73] E. Fried, "Thermal Conduction Contribution to Heat Transfer at Contacts," in *Thermal Conductivity*, vol. 2, London, Academic Press, 1969.
- [74] W. H. McAdams, "Chapter 7," in *Heat Transmission 3rd Ed.*, New York, McGraw-Hill, 1954.

- [75] R. J. Goldstein, E. M. Sparrow and D. C. Jones, "Natural convection mass transfer adjacent to horizontal plates," *International Journal of Heat and Mass Transfer*, vol. 16, no. 5, pp. 1025-1035, 1973.
- [76] J. R. Lloyd and W. R. Moran, "Natural Convection Adjacent to Horizontal Surface of Various Planforms, ASME paper 74-WA/HT-66," ASME , 1974.
- [77] H. H. S. C. Stuart W. Churchill, "Correlating Equations for Laminar and Turbulet Free Convection from a Vertical Plate," *International Journal of Heat and Mass Transfer*, vol. 18, no. 11, pp. 1323-1329, 1975.
- [78] H. U. Tetso Fujii, "Laminar Natural-Convective Heat Transfer From the Outer Surface of a Vertical Cylinder," *International Journal of Heat and Mass Transfer*, vol. 13, pp. 607-615, 1970.
- [79] Python Software Foundation.
- [80] G. C. Vliet and C. K. Liu, "An Experimental Study of Turbulent Natural Convection Boundary Layers," *Journal of Heat Transfer*, vol. 91, pp. 517-531, 1969.
- [81] K. Millsaps and K. Pollhausen, "Heat Transfer to Hagen-Poiseuille Flows," in *Proceedings of the conference on differential equations*, 1956.
- [82] Grant, Selected Papers on particle image velocimetry, Bellingham, WA: SPIE Optical Engineering Press, 1994.

## 8 NOMENCLATURE

$A, B, C, D, E, F, G$	Correlation Coefficients
$A_c$	Cross Sectional Area of Channel
$A_p$	Area of Conduction Region of Plate
$A_s$	Surface Area of Plate
$A_w$	Wetted Surface Area Inside Coolant Channels in Plate
$\beta$	Volumetric Thermal Expansion Coefficient
$Bi$	Biot Number
$C_p$	Heat Capacity
$D$	Diameter
$D_h$	Hydraulic Diameter
$\delta$	Boundary Layer Thickness
$\delta_p$	Thickness of Conduction Region of Plate
$\Delta T$	Temperature Difference
$f$	Friction Factor
$g$	Acceleration due to gravity
$Gr$	Grashof Number
$Gr_L$	Grashof Number Based on Characteristic Length $L$
$h$	Heat Transfer Coefficient
$h_c$	Convective Heat Transfer Coefficient in Cooling Channel
$h_t$	Heat Transfer Coefficient From Tank to Plate
$I(X)$	Intensity Distribution
$I_1$	Interrogation Area 1
$I_2$	Interrogation Area 2
$k$	Thermal Conductivity
$k_f$	Thermal Conductivity of Fluid

$k_{inc}$	Thermal Conductivity of Inconel-800
$k_{MgO}$	Thermal Conductivity of Magnesium Oxide
$k_c$	Thermal Conductivity of Copper
$L$	Length
lhs	Left Hand Side of an Equation
$L_r$	Heated Length of Rod
$\dot{m}$	Mass Flow Rate
$\mu$	Viscosity
$N$	Number of Samples
$Nu$	Nusselt Number
$Nu_D$	Nusselt Number Based on $Re_D$
$Nu_L$	Nusselt Number Based on $Re_L$
$\overline{Nu_L}$	Mean Nusselt Number
$\overline{Nu_p}$	Mean Nusselt Number for a Plate
$\eta$	Similarity Parameter
$\nu$	Kinematic Viscosity
$Pr$	Prandtl Number
$q$	Power
$\dot{q}$	Volumetric power generation
$q''$	Power Per Unit Area
$Q_{in}$	Total Power Added to the System by Heater Rods
$Q_{out}$	Total Power Removed from System by Cooling Plate
$q_p$	Power Removed by Plate
$q_x''$	Power from Plate B to Plate A per area
$R^2$	Coefficient of Determination
$Ra$	Rayleigh Number
$Ra_L$	Rayleigh Number Based on Length

$r_{ci}$	Radial Position of the Inside of the Heater Rod Cladding
$r_{co}$	Radial Position of the Inside of the Heater Rod Cladding
$r_e$	Radial Position of the Outer Edge of the Heater Element
$Re_D$	Reynolds Number based on Diameter
$Re_L$	Reynolds Number based on L
rhs	Right Hand Side of an Equation
$R''_{t,c}$	Thermal Resistance
$\rho$	Density
$s'$	Shift in Space for Cross Correlation Function
$S_{\bar{x}}$	Mean Error of a Set of Samples
$S_x$	Error of a Single Sample
T	Temperature
$T_A$	Temperature of Plate Side A at Interface
$T_B$	Temperature of Plate Side B at Interface
$T_c$	Critical Temperature of Water
$T_s$	Surface Temperature of Heater Rod
$T_{TC}$	Temperature Reading From Rod Centerline
	Thermocouple
$T_{\infty c}$	Average Cooling Water Temperature
$T_{\infty t}, T_{\infty}, T_{bulk}$	Bulk Fluid Temperature in Tank
$U_h$	Overall Uncertainty for Sequential Perturbation Method
u	Velocity perpendicular to gravity
$V, V_1$	Velocity Parallel to Gravity
$V_{bulk}$	Bulk Velocity Parallel to Gravity
$V_{entrance}$	Entrance Velocity of Channel Parallel to Gravity
w	Velocity in the z direction
$W_1$	Location in Cross Correlation Distribution

x	Coordinate Indicating Position along Length of Heater Rod From Bottom
y	Coordinate Indicating Position in Channel Measured From Inner Rod Surface
$\infty$	Subscript indicating bulk properties
*	Superscript indicating non-dimensionalized parameter

#### ACRONYMS

IAEA	International Atomic Energy Association
LINC	Laser-Imaged Natural Circulation Facility
MgO	Magnesium Oxide Ceramic
Nd:Yag	Neodymium-doped Yttrium Aluminum Garnet
SMR	Small Modular Reactor
SN Ratio	Signal to Noise Ratio
PIV	Particle Image Velocimetry

## 9 APPENDIX A: UNCERTAINTY ANALYSIS

The uncertainty associated with the temperature measurements was found by using the standard deviation of the means method shown in (9.1) where  $S_{\bar{x}}$  is the mean error,  $S_x$  is the error of a single measurement and  $N$  is the number of samples.

$$S_{\bar{x}} = \frac{S_x}{\sqrt{N}} \quad (9.1)$$

For K-type thermocouples the error is 2.2°C or 0.75%, whichever is greater. In the case of the equilibrium condition, the error was taken to be 2.2°C for each sampling and the equilibrium temperature was taken for a least 100 minutes at a rate of 1 Hz, for a total of 6000 temperature measurements. This equates to a sampling error in the equilibrium temperature measurement of 0.028°C. The error bars on the thermal equilibrium temperature summary plot were shown as 2.2°C. The error from the CompactRio measurement system was considered to be negligible comparatively.

For the power measurement from the cooling plate, the sequential perturbation method can be used. This is shown generically in equation (9.2) where  $U_h$  is the overall uncertainty,  $x$  is representative of each parameter in an equation and  $\Delta x_i$  is the error in that parameter.

$$U_h = \sqrt{\sum_{i=1}^N (R(x_1, x_2, x_3, \dots, x_i + \Delta x_i, x_{N+1}, \dots, x_n) - R(x_1, x_2, x_3, \dots, x_n))^2} \quad (9.2)$$

For the case of the heat removed by the cooling plate, equation (3.39) is the expression of interest ( $R(x)$  in equation (9.2)). The errors of each component are listed in Table 9.1.



Table 9.1 Tabulated Error for Cooling Calculation Components

Component	Error
Flow Meter	+/- 2%
Thermocouples	0.028°C
Density Correlation	0.2%
Heat Capacity Correlation	1%

Using equation (9.2), the uncertainties for the three thermal equilibrium cases were evaluated and are tabulated in Table 9.8.

Table 9.2 Equilibrium Plate Power Removal Uncertainty

Power Test Case	Uncertainty
200W	+/- 9.44 W
300W	+/- 13.14W
400W	+/- 16.8W

For the Nu vs. Ra plot presented, the error bars were calculated using the sequential perturbation method as well. This began with an analysis of the error in the surface temperature calculation.

Table 9.3 Tabulated component error for surface temperature calculation

Component	Error
Element Radius	0.2mm
Inner Clad Radius	0.5mm
Outer Clad Radius	0.2mm
Thermal Conductivity MgO	1%
Bulk T Measurement	0.05°C
Thermal Conductivity Inc-800	1%
Rod Power	2W

Using these values, the uncertainty for the temperature calculation was found to be near enough to 0.22°C for all cases that it was taken as a constant in further calculations.

The Rayleigh error was calculated using the same method with the errors tabulated in Table 9.4.

Table 9.4 Tabulated component error for Ra calculation

Component	Error
Thermocouple Axial Location	6mm
Bulk Temperature	0.05°C
Surface Temperature	0.25°C

Using these values the error in Ra was calculated and tabulated in Table 9.5.

Table 9.5 Uncertainty in Ra for 4 thermal equilibrium cases

Power Test Case	Uncertainty
100W	1.17E+08
200W	2.96E+08
300W	5.10E+08
400W	7.35E+08

The error in Nu was also calculated using sequential perturbation method where the errors of each component are listed in Table 9.6

Table 9.6 Tabulated error for Nu calculation

Component	Error
Rod Diameter	0.4mm
Thermocouple Axial Location	6mm
Bulk Temperature	0.05°C
Surface Temperature	0.25°C

The result of the Nusselt number error calculation is tabulated in Table 9.7.

Table 9.7 Uncertainty in Nu for 4 thermal equilibrium cases

Power Test Case	Uncertainty
100W	7.014
200W	8.042
300W	9.062
400W	14.491

The uncertainty in the PIV data for the velocity profile analysis was obtained for each velocity discussed in the results in terms of the standard deviation of V. It is presented here in Table 9.8.

Table 9.8 Standard deviation of V used in velocity profile analysis (mm/s)

y location in channel (mm)	Distance x From Heater Rod End (mm)									
	3.06	13.22	23.07	32.92	43.08	53.19	63.04	73.20	83.05	90.75
0.23	0.06	0.28	0.50	0.61	0.70	0.93	0.96	1.01	1.07	1.37
0.46	0.12	0.14	0.52	0.64	0.73	0.90	0.94	1.13	1.16	1.58
0.69	0.19	0.14	0.50	0.65	0.72	0.94	1.05	1.10	1.24	1.69
0.92	0.22	0.29	0.53	0.68	0.78	1.00	1.14	1.17	1.36	1.79
1.15	0.25	0.34	0.50	0.62	0.60	1.03	1.27	1.52	1.79	2.20
1.38	0.21	0.36	0.47	0.63	0.62	0.97	1.23	1.51	1.86	1.96
1.61	0.19	0.37	0.49	0.57	0.65	0.89	1.13	1.24	1.51	1.91
1.84	0.19	0.35	0.46	0.53	0.61	0.80	0.97	1.19	1.30	1.62
2.07	0.18	0.32	0.42	0.50	0.57	0.79	0.91	0.97	1.21	1.48
2.30	0.17	0.30	0.38	0.47	0.55	0.73	0.78	0.89	1.02	1.18
2.53	0.18	0.26	0.35	0.43	0.51	0.66	0.72	0.81	0.92	0.97
2.76	0.18	0.24	0.31	0.40	0.47	0.62	0.68	0.75	0.80	0.93
2.99	0.17	0.23	0.28	0.34	0.44	0.53	0.63	0.68	0.75	0.86
3.22	0.16	0.21	0.25	0.33	0.42	0.49	0.60	0.64	0.72	0.82
3.45	0.18	0.20	0.26	0.31	0.40	0.46	0.55	0.61	0.66	0.77
3.68	0.17	0.20	0.25	0.29	0.38	0.42	0.49	0.56	0.61	0.70
3.91	0.17	0.19	0.24	0.27	0.36	0.42	0.49	0.51	0.60	0.68
4.14	0.18	0.20	0.23	0.27	0.36	0.41	0.47	0.49	0.59	0.67
4.37	0.18	0.20	0.24	0.26	0.37	0.41	0.44	0.52	0.57	0.68
4.60	0.19	0.22	0.25	0.28	0.37	0.40	0.45	0.52	0.54	0.64

In the positioning system, there was an error of 2mm for vertical adjustment, which in the cases presented here correlates to +/- 54 pixels of total uncertainty in the vertical direction. The camera was never moved from right to left nor forward and back so no error was introduced in those adjustments. The scaling factor has an uncertainty of 5 pixels, and since the heater rods were used for the reference scale for the scaling factor, there is also uncertainty in the nominal diameter of the rods. This error is taken to be 0.5 mm, or 13.6px.

## 10 APPENDIX B: EXPERIMENTAL FACILITY DRAWINGS

The figures in this section are intended to provide a better understanding of the LINC facility as fabricated.

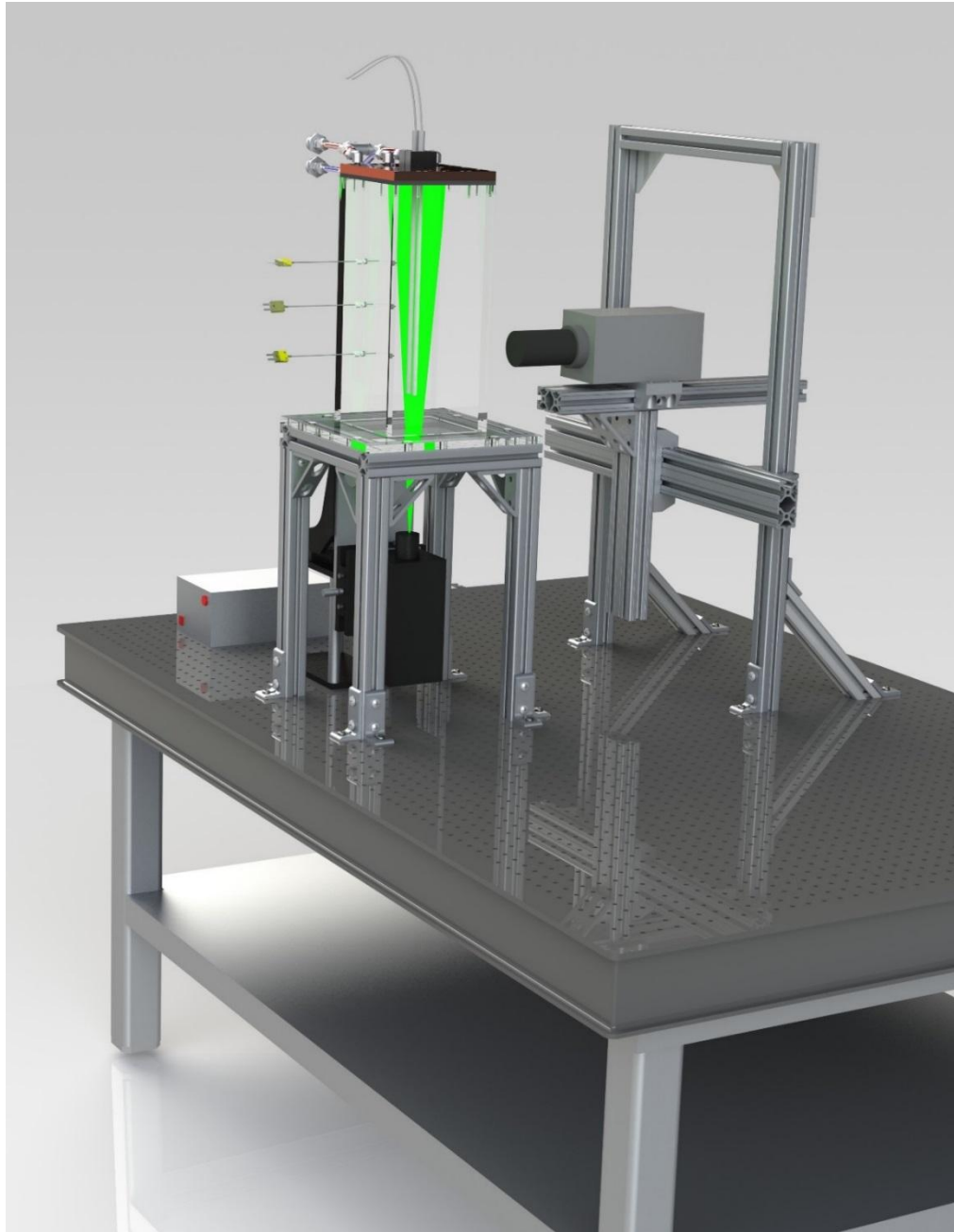


Figure 10.1 Rendering of LINC facility

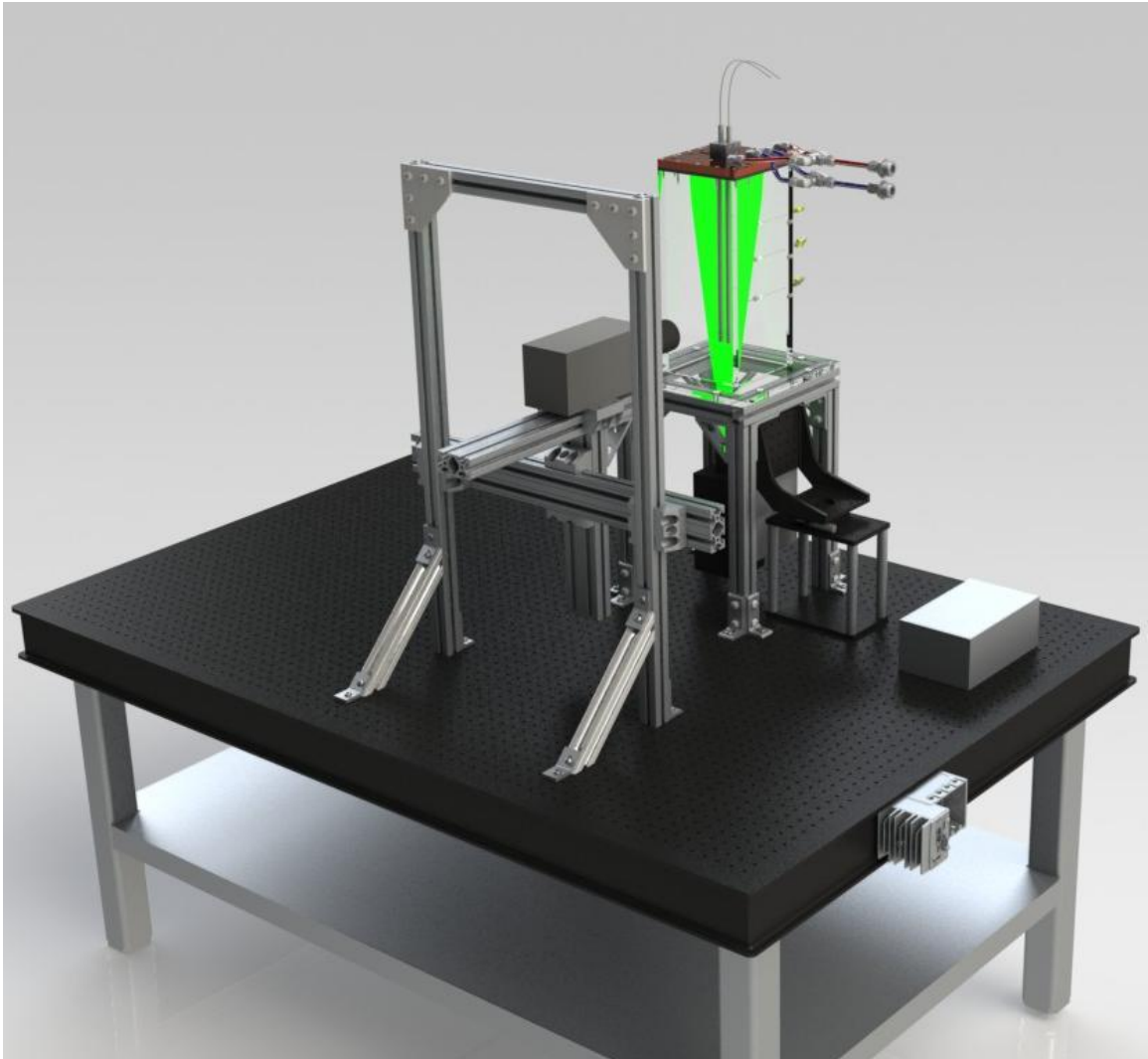


Figure 10.2 Rear view rendering of LINC facility

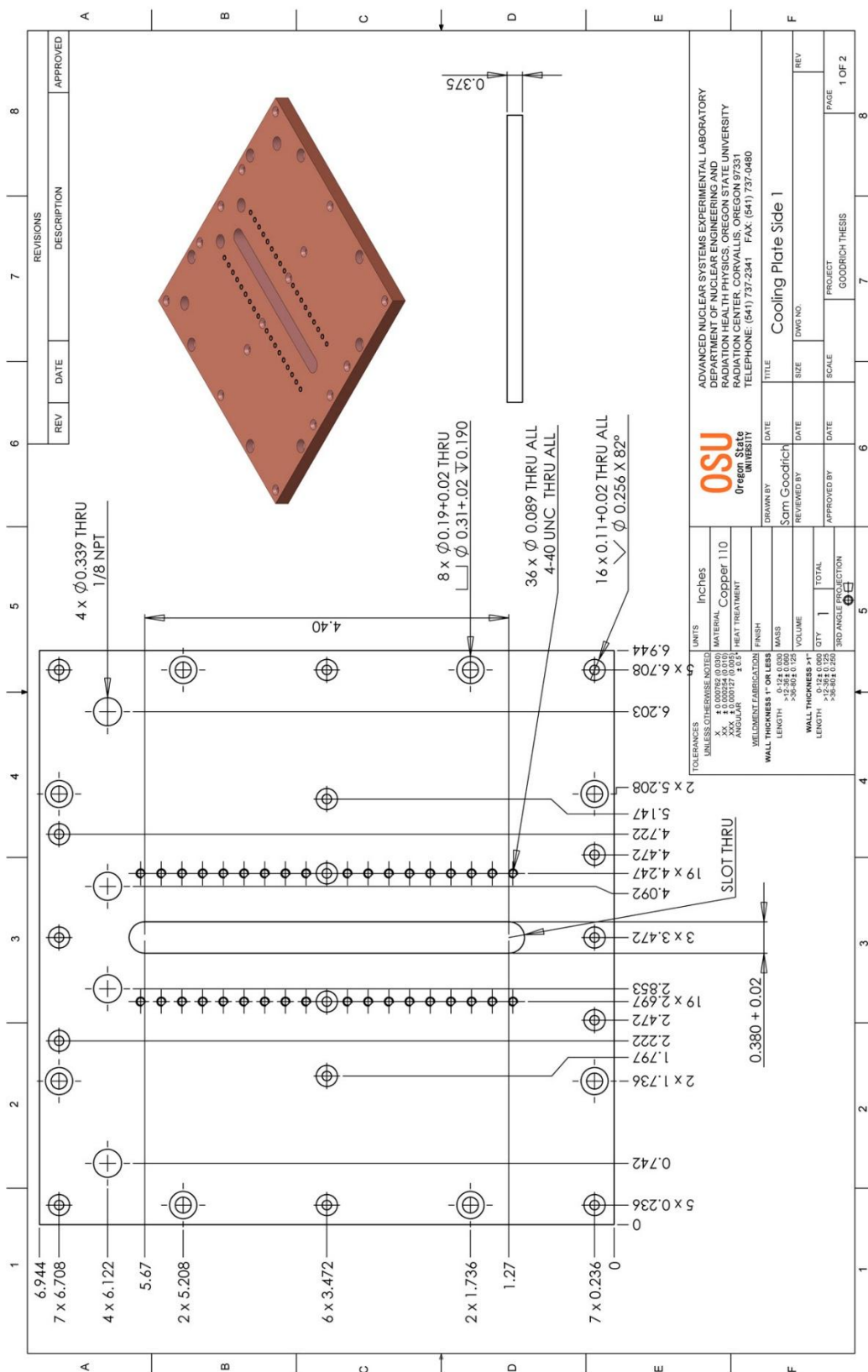


Figure 10.3 Cooling Plate Side A Top View Detail

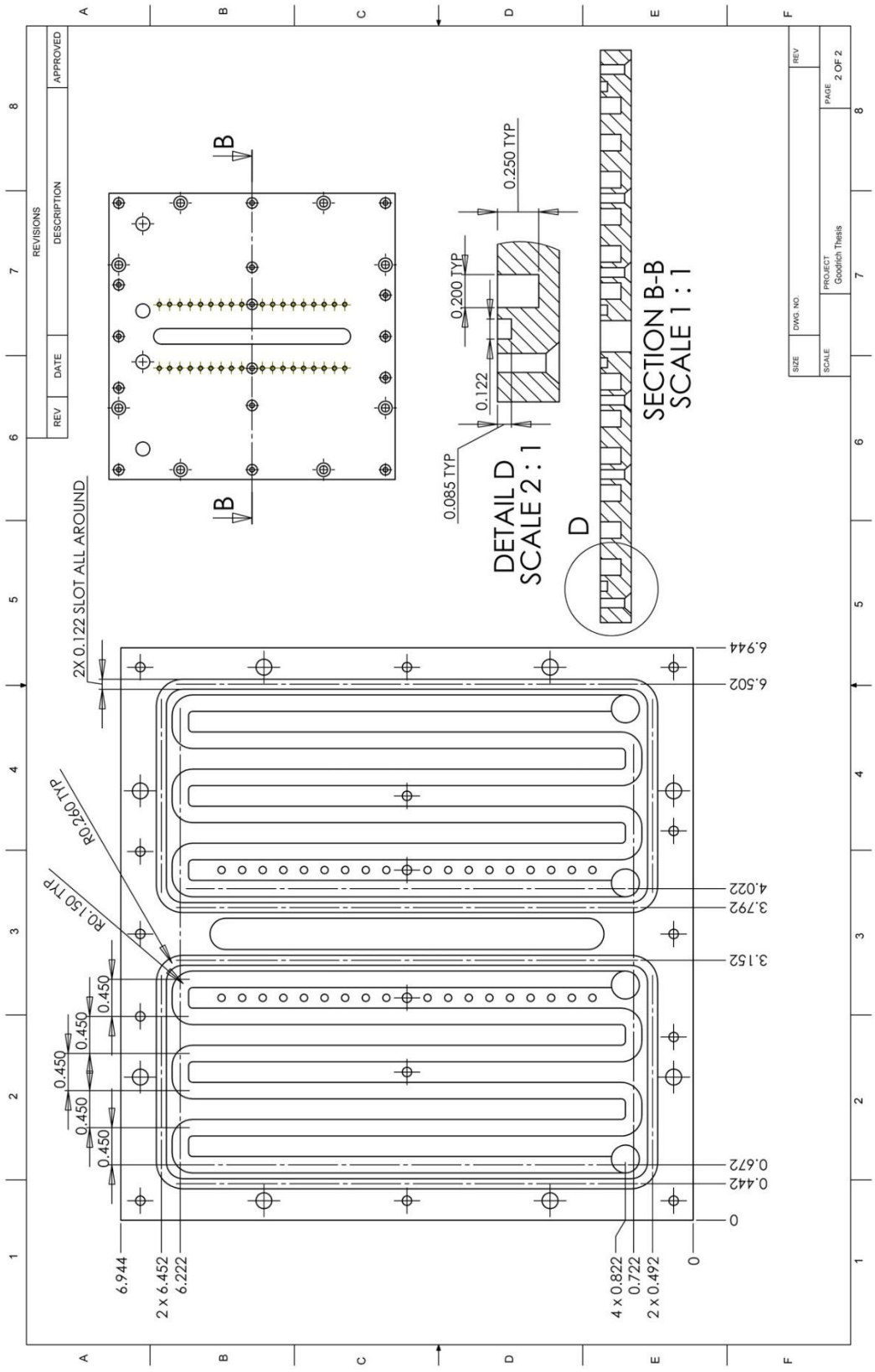


Figure 10.4 Cooling Plate Side A Bottom View Detail



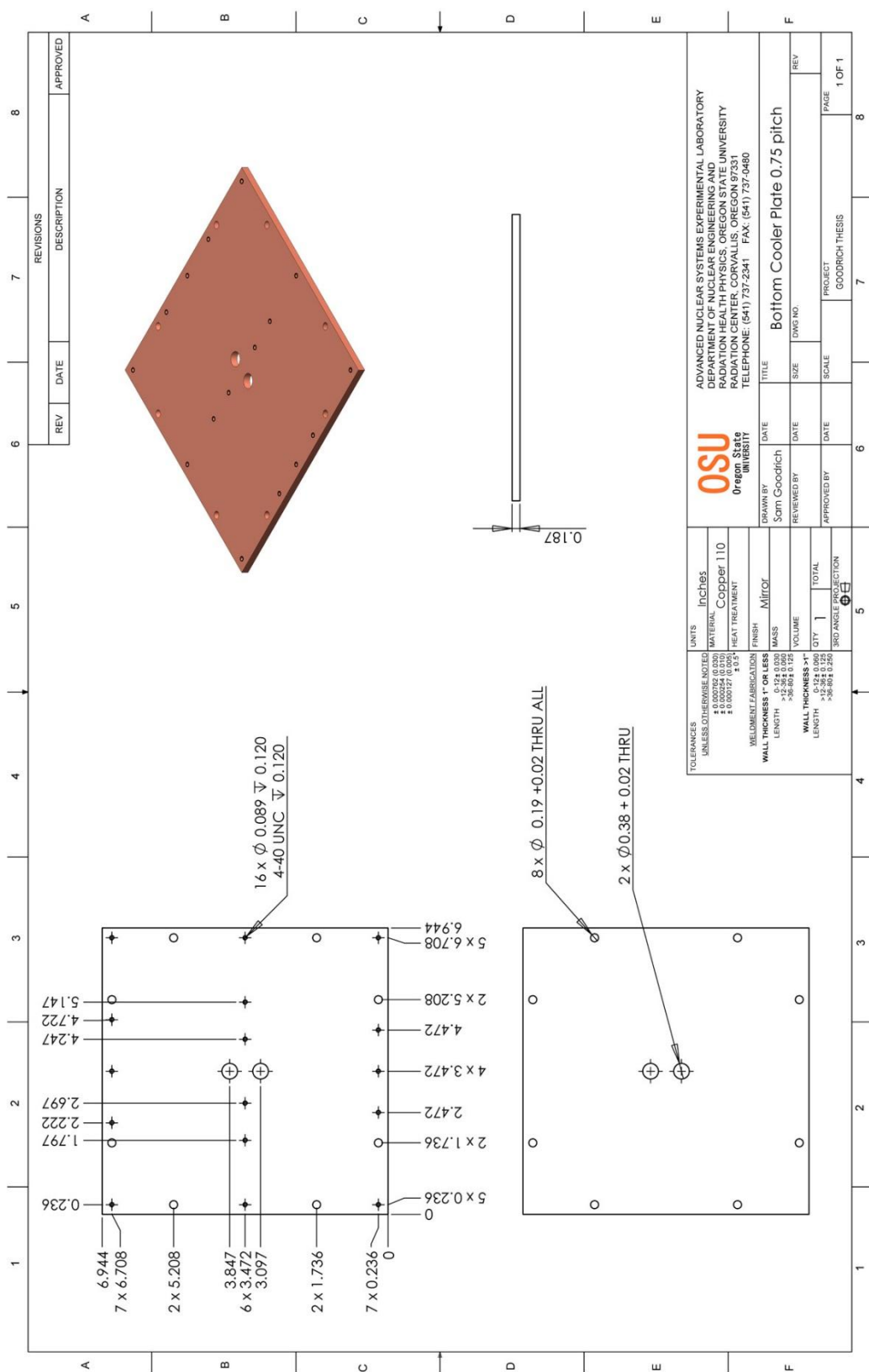


Figure 10.5 Cooling Plate Side B Top View Detail

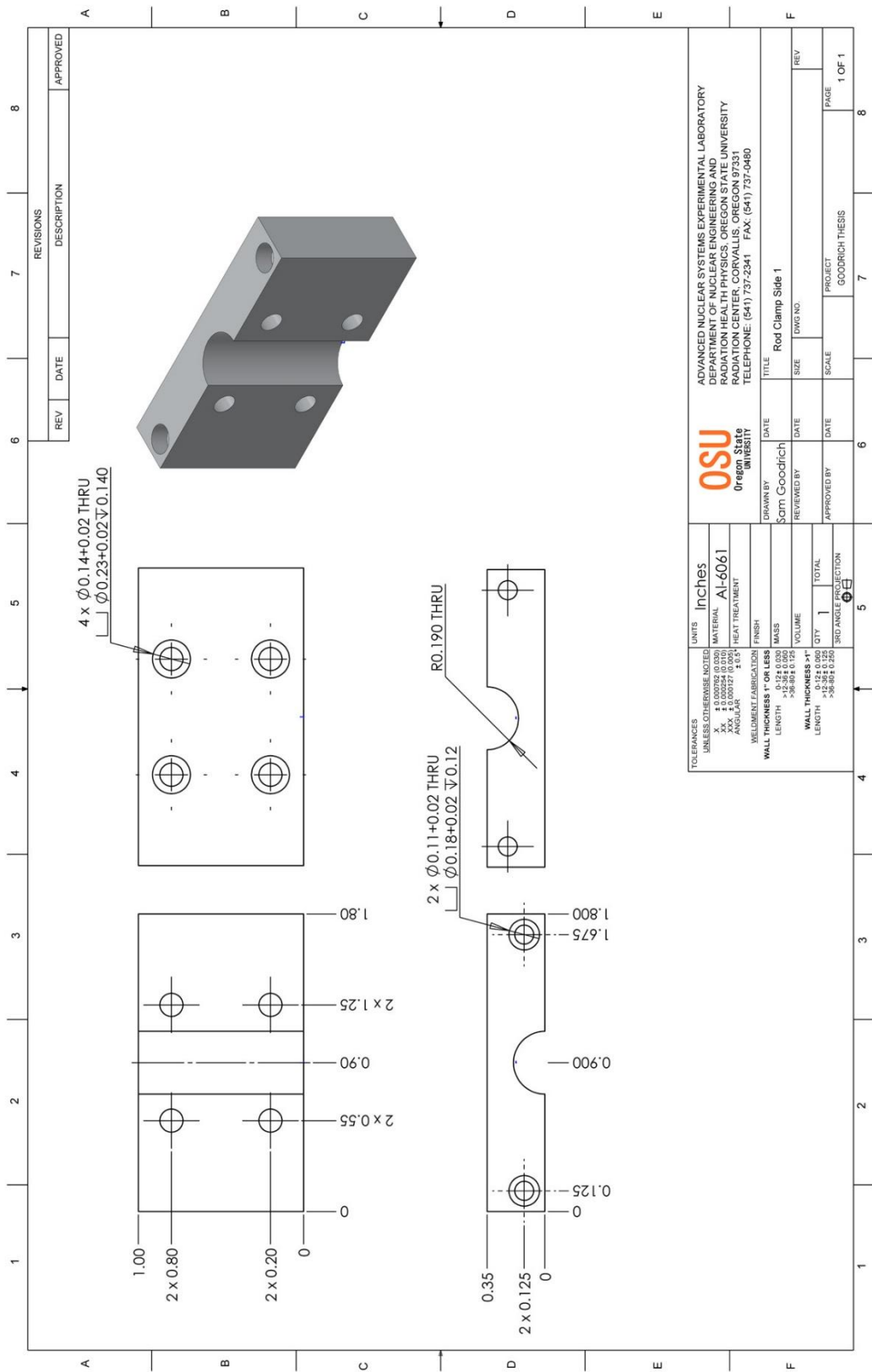
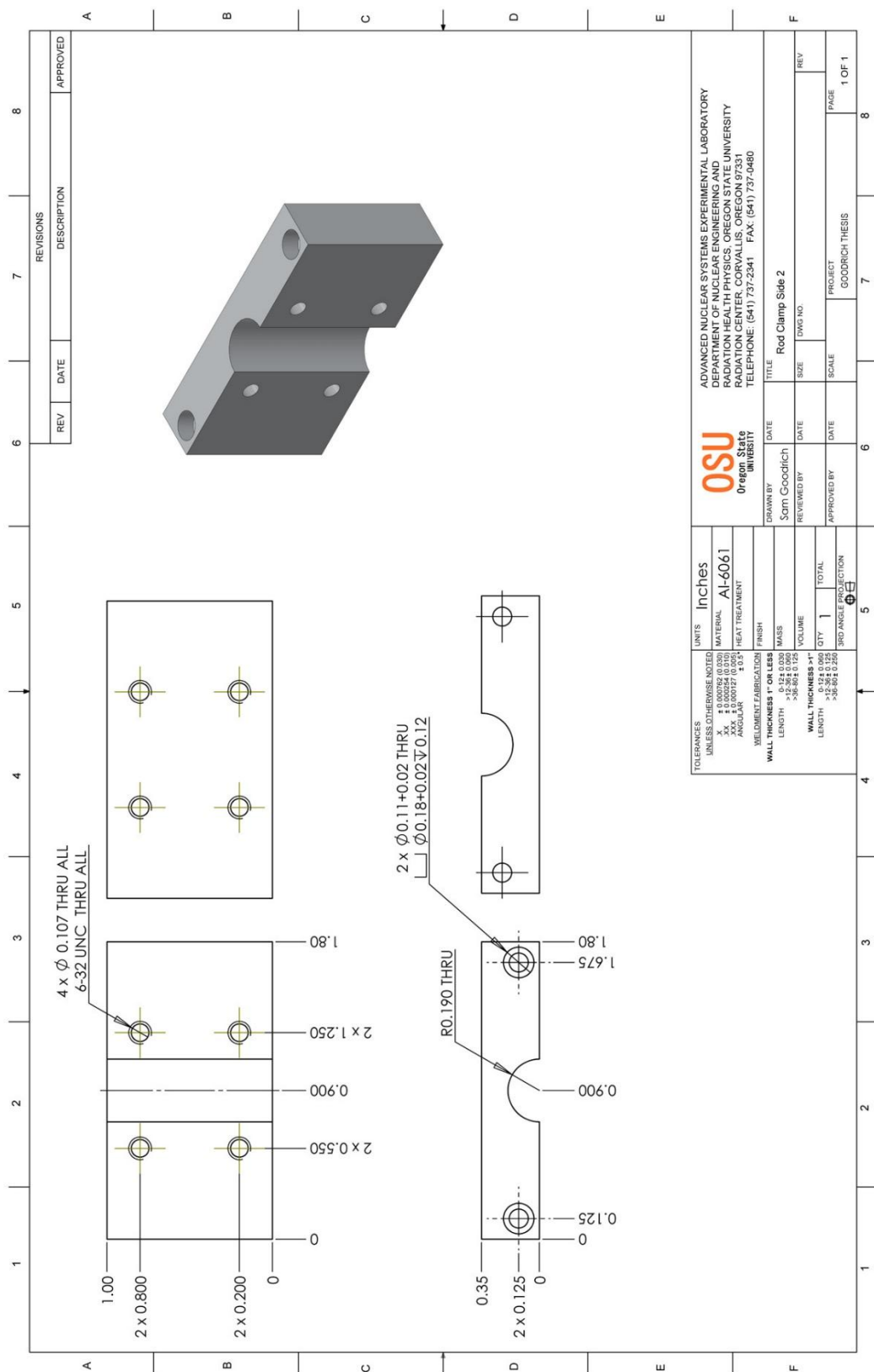


Figure 10.6 Heater Rod Clamp Side 1 Detail



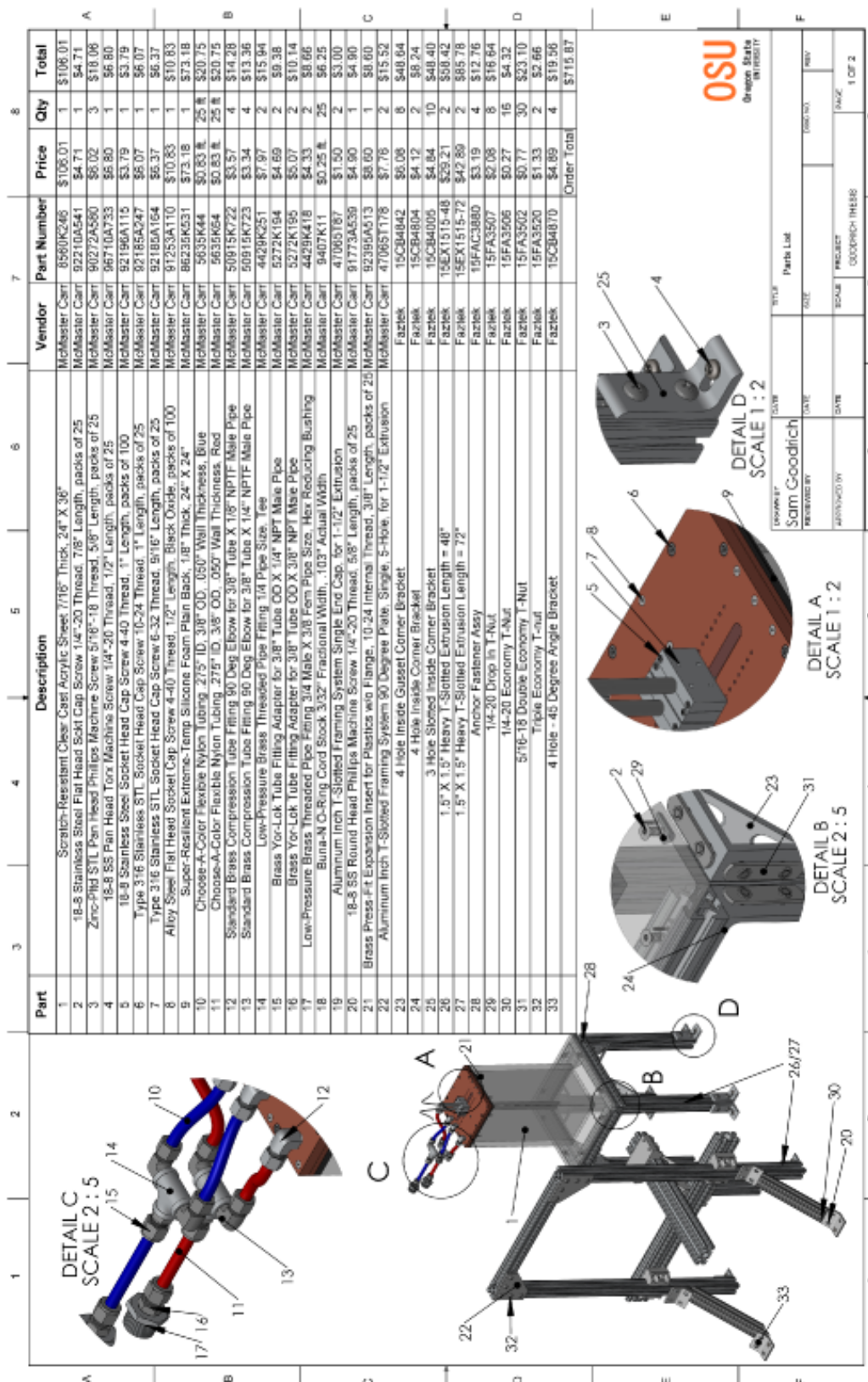


Figure 10.8 Parts List